Digital Dashboards for Smart City Governance: a Case Project to Develop an Urban Safety Indicator Model

POLITECNICO DI TORINO

SCUOLA INTERPOLITECNICA DI DOTTORATO

Doctoral Program in Biomedical Engineering

Final Dissertation

Improving nonlinear search with Self-Organizing Maps - Application to Magnetic Resonance Relaxometry

Laura Gaetano

Tutor
prof. F.M. Montevecchi
prof. R. G. Henry

Co-ordinator of the Research Doctorate Course
prof. F.M. Montevecchi

February, 2012

This page intentionally left blank.

To M. and E.

Preface

My years as a PhD student were characterized just by curiosity and hunger for knowledge. During the school, I chose to dedicate my time to the projects I was really interested in to discover what I like most. Luckily, my supervisor permitted all this. In these years, I dealt with a miscellaneous of topics, ranging from artificial intelligence to cell cultures, stopping by clinical engineering, optimization algorithms, system dynamics, and so on. My research 'adventure' ends up with this thesis and with its topic: bio-imaging. After all my wander around, I have found my way, I have found what I really like to do, I have found what really arouses me.

This thesis is a summing up of all the 'wander around', describing in details what has aroused me in the last years, and presenting a brief collection of other works that I enjoyed doing during my PhD school.

Index

Abstract

Quantification of myelin in vivo is crucial for the understanding of neurological diseases, like multiple sclerosis (MS). Multi-Component Driven Equilibrium Single Pulse Observation T1 and T2 (mcDESPOT) is a rapid and precise method for determination of the longitudinal and transverse relaxation times in a voxel wise fashion. Briefly, mcDESPOT couples sets of SPGR (spoiled gradient-recalled echo) and bSSFP (fully balance steady-state free precession) data acquired over a range of flip angles (α) with constant interpulse spacing (TR) to derive 6 parameters (free-water T1 and T2, myelin-associated water T1 and T2, relative myelin-associated water volume fraction, and the myelin-associated water proton residence time) based on water exchange models. However, this procedure is computationally expensive and extremely difficult due to the need to find the best fit to the 24 MRI signals volumes in a search of nonlinear 6 dimensional space of model parameters.

In this context, the aim of this work is to improve mcDESPOT efficiency and accuracy using tissue information contained in the sets of signals (SPGR and bSSFP) acquired. The basic hypothesis is that similar acquired signals are referred to tissue portions with close features, which translate in similar parameters. This similarity could be used to drive the nonlinear mcDESPOT fitting, leading the optimization algorithm (that is based on a stochastic region contraction approach) to look for a solution (i.e. the 6 parameters vector) also in regions defined by previously computed solutions of others voxels with similar signals.

For this reason, we clustered the sets of SPGR and bSSFP using the neural network called Self Organizing Map (SOM), which uses a competitive learning technique to

train itself in an unsupervised manner. The similarity information obtained from the SOM was then used to accordingly suggest solutions to the optimization algorithm. A first validation phase with *in silico* data was performed to evaluate the performances of the SOM and of the modified method, SOM+mcDESPOT. The latter was further validated using real magnetic resonance images. The last step consisted of applying the SOM+mcDESPOT to a group of healthy subjects ($n = 10$) and a group of MS patients ($n = 55$) to look for differences in myelin-associated water fractions values between the two groups.

The validation phases with *in silico* data verified the initial hypothesis: in more the 74% of the times, the correct solution of a certain voxel is in the space dictated by the cluster which that voxel is mapped to. Adding the information of similar solutions extracted from that cluster helps to improve the signals fitting and the accuracy in the determination of the 7 parameters. This result is still present even if the data are corrupted by a high level of noise (SNR=50). Using real images allowed to confirm the power of SOM+mcDESPOT underlined through the *in silico* data. The application of SOM+mcDESPOT to the controls and to the MS patients allowed firstly obtaining more feasible results than the traditional mcDESPOT. Moreover, a statistically significant difference of the myelin-associated water fraction values in the normal appearing white matter was found between the two groups: the MS patients, in fact, show lower fraction values compared to the normal subjects, indicating an abnormal presence of myelin in the normal appearing white matter of MS patients.

In conclusion, we proposed the novel method SOM+mcDESPOT that is able to extract and exploit the information contained in the MRI signals to drive appropriately the optimization algorithm implemented in mcDESPOT. In so doing, the overall accuracy of the method in both the signals fitting and in the determination of the 7 parameters improves. Thus, the outstanding potentiality of SOM+mcDESPOT could assume a crucial role in improving the indirect quantification of myelin in both healthy subjects and patients.

1. Introduction

In this chapter, all basic principles necessary to understand the problem faced in this thesis and its importance are introduced. For this reason, a brief description of brain anatomy, its normal composition and a particular disease (i.e. the Multiple Sclerosis) that affects it allows setting the practical importance of this work. One of the most promising tools available nowadays to deal with the problem is then presented, since its modified counterpart is the subject of this thesis.

1.1. Basic principles of brain anatomy

The human nervous system monitors, processes and responds to information coming from inside and outside the body [1]. It is formed by two main parts, that are anatomically separate but strictly interconnected and integrated in terms of functionalities: the central nervous system, CNS, and the peripheral nervous system, PNS (Figure 1). The former essentially consists of the brain and the spinal cord, while the latter is formed by nerves extending to and from the brain and the spinal cord.

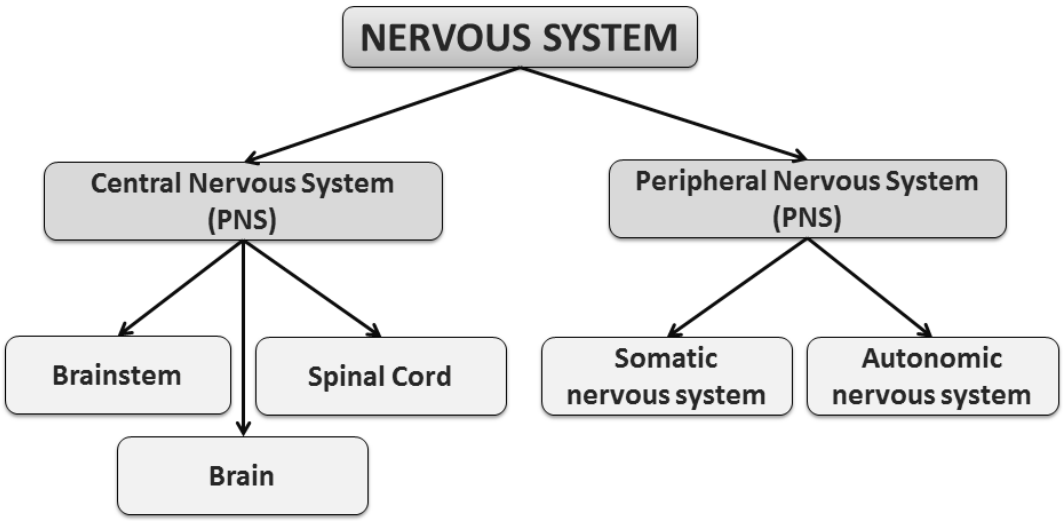

Figure 1. Overview of the anatomical organization of the nervous system.

The brain is protected by the bony structures of the vertebral canal and skull, and an additional mechanical buffering protection is afforded by the surrounding meninges and ventricular system. Their functions are to protect the CNS and blood vessels, enclose the venous sinuses, retain the cerebrospinal fluid, and form partitions within the skull. At birth the brain weighs less than 400 g, but by the beginning of the second year of life it has more than doubled in weight to 900 g [2]. The adult brain weighs between 1.250 and 1.450 g, and demonstrates a gender differential, since brains of males generally weigh more than those of females [2]. This increase in weight is due more to the proliferation of glia cells than to the mitotic activity of neurons.

Viewing an adult brain from an external point of view, three regions are clearly visible: the cerebrum, cerebellum, and part of the brainstem (Figure 2 a).

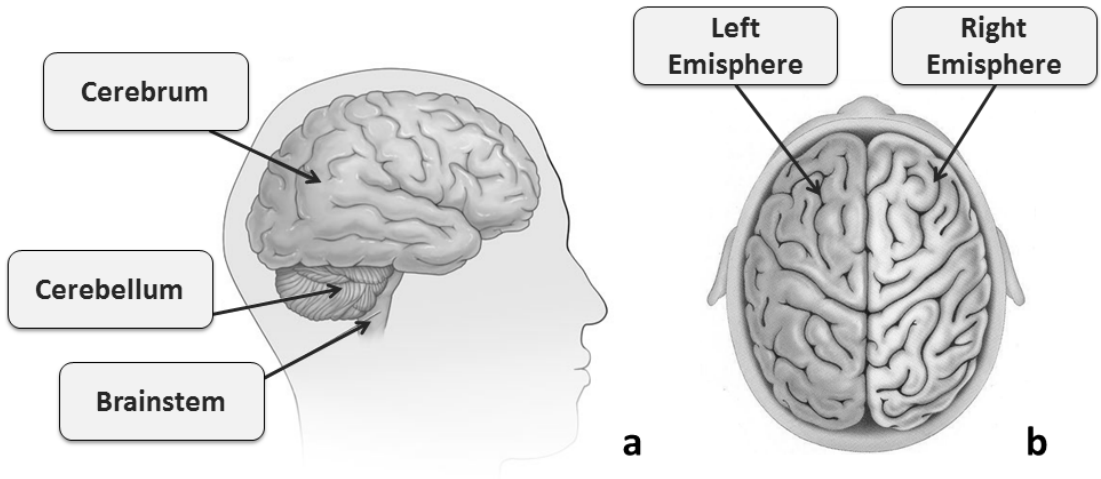

Figure 2. An external view of the brain: from one side (a) and from the top (b).

The cerebrum is a hollow structure divided into two hemispheres by the midline longitudinal cerebral fissure (Figure 2 b). Each hemisphere is subdivided into five lobes: the frontal (involved with decision-making, problem solving, and planning),

parietal (involved in the reception and processing of sensory information from the body), temporal (involved with memory, emotion, hearing, and language), and occipital lobes (involved with vision), and the insula (involved in emotions and regulations of the body's homeostasis). Additionally, the external part of the limbic system can be considered as sixth lobe, the limbic lobe (it regulates autonomic and endocrine functions, particularly in response to emotional stimuli). The hemispheres are connected through the corpus callosum (Figure 3), the largest connective structure in the brain, consisting of over 190 million axons that transfer information between the two cerebral hemispheres [3]. Below the corpus callosum are the front ends of two cavities within the cerebral hemispheres, the lateral ventricles (Figure 3).

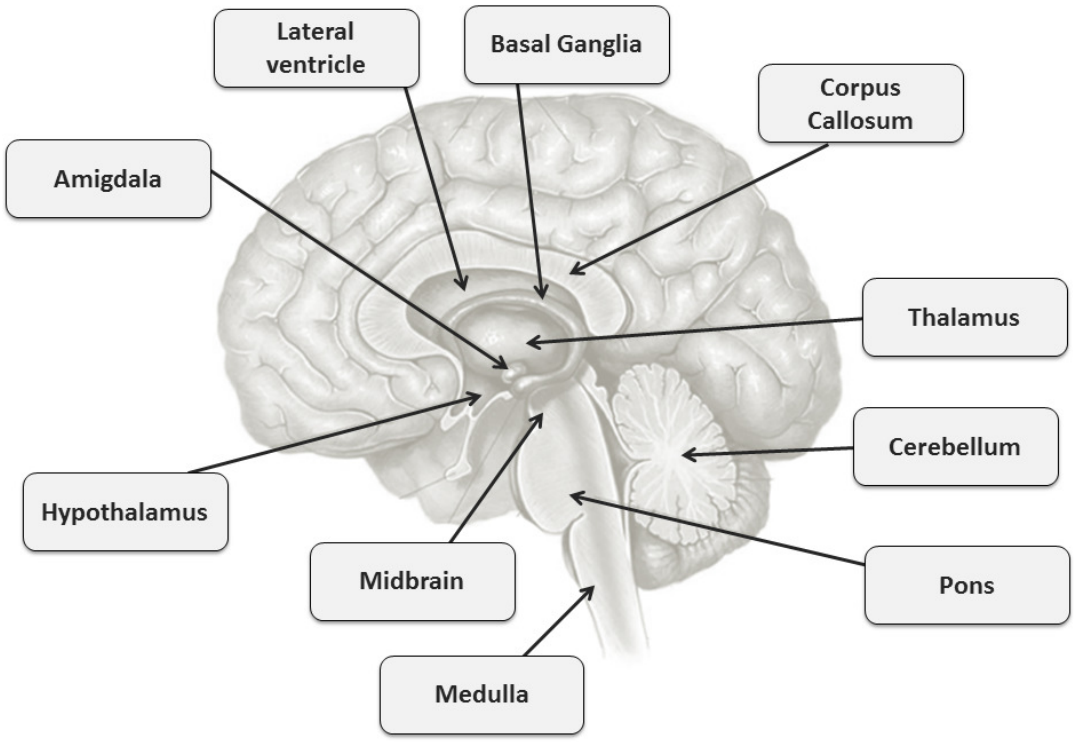

Figure 3. Major parts of the brain.

They, named based on their position as right and left lateral ventricles, are separated from each another by two closely adjoined non-nervous membranes (septum

pellucidum); they are filled with cerebrospinal fluid and, in the same time, and they are the site of the choroid plexus, a structure that produces this fluid. The cerebral hemisphere surface is composed of a highly folded collection of grey matter, known as the cerebral cortex (Figure 2 b and Figure 4). That typical convolution forms ridges (gyri or gyrus, as singular), valleys (sulci or sulcus, as singular) or fissures (sulci particularly deep), allowing, in so doing, to reach a total surface area of several hundred square centimetres [1]. The convoluted surface comprises a continuous layered or laminated sheet of neurons and supporting cells about 2 mm thick called the cerebral cortex and it lies over and around most of the structures of the brain. Deep to the cortex is placed the substance of the cerebrum, i.e. the white matter (Figure 4).

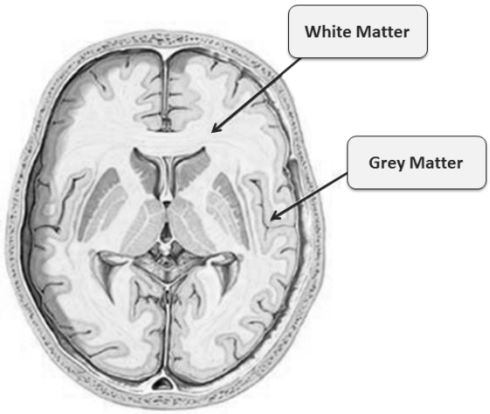

Figure 4. White and grey matter.

It consists of myelinated neurons of varied sizes and their supporting glia. Buried in the white matter, the basal ganglia are large collections of cell bodies (Figure 3) that, when damaged, produce movement disorders. Other major sub-cortical structures, such as the thalamus and the hypothalamus, are situated below the corpus callosum (Figure 3). The thalamus relays sensory inputs to the cortex. The hypothalamus controls the release of major hormones and it is involved in processes such as

temperature regulation, control of food and water intake, sexual behaviour and reproduction, control of daily cycles in physiological state and behaviour, and mediation of emotional responses.

The other structure visible from an external point of view is the cerebellum, located in the posterior part of the brain, just below the occipital lobes of the cerebrum (Figure 3). It essentially controls the timing and pattern of muscle activation during movement, regulates muscle tone in postural control, and provides an important role in maintaining the equilibrium. Similar to the cerebrum, the cerebellum has an outer rim of grey matter, the cortex, an inner core of nerve fibers, the medullary white matter, and the deep cerebellar nuclei, located within the white matter.

Finally, the brainstem, the oldest part of the CNS, is structurally continuous with the spinal cord and it is composed of the mesencephalon, pons, cerebellum, and medulla oblongata (Figure 3). It is an extremely important structure, since all nerve connections of the motor and sensory systems from the main part of the brain to the rest of the body pass through it.

All the structures described above have different morphological aspects depending on the plane of section. Generally, three anatomical planes are considered:

1. the sagittal section is a vertical plane through the brain, parallel to the median plane. The latter slices the brain vertically along the midline into two symmetrical halves (Figure 5 d);
2. the horizontal (or axial) section is a plane across the brain that would be horizontal if the patient were standing up (Figure 5 c);
3. the coronal (or frontal) section is a plane that slices the brain vertically (Figure 5 b).

Moreover, based on their positions (Figure 5 a), structures can be termed as:

1. anterior (or rostral): if they are towards the front of the brain;
2. posterior (or caudal): if they are towards the back;
3. superior: if they are towards the top of the brain;

4. inferior: if they are towards bottom.

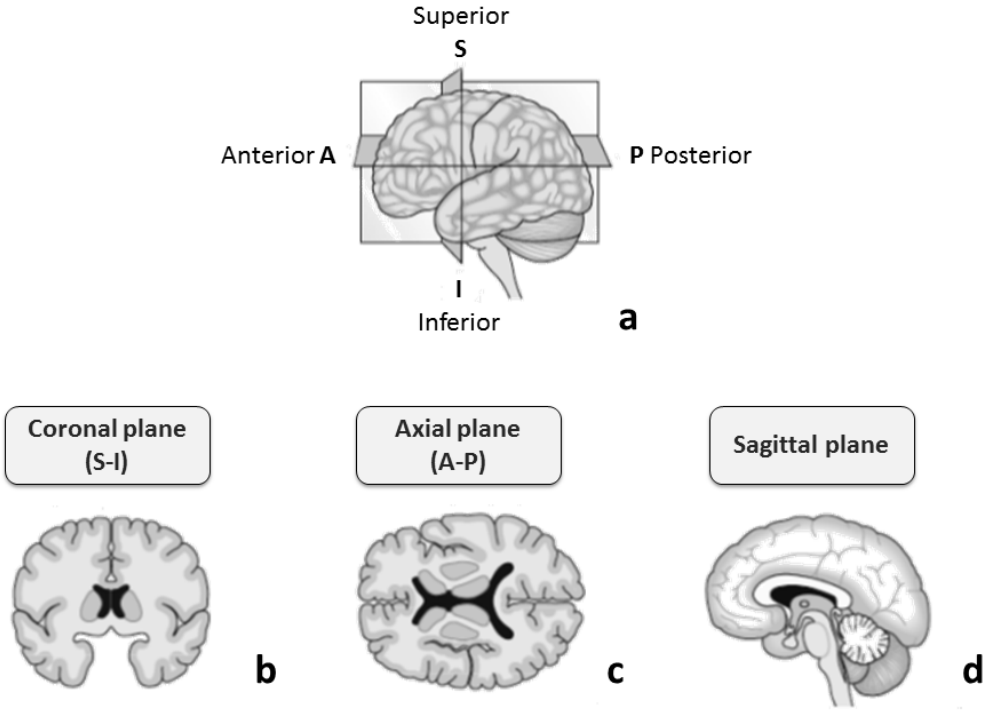

Figure 5. Anatomical planes of section. Depending on the plane of section (a), coronal or frontal (b), horizontal or axial (c), and sagittal (d) view can be obtained.

1.2. Myelin sheath: structure, function, formation and damage

The CNS is mainly composed of two cell types: neurons and glia [1, 4].

Each neuron consists of a cell body (containing the nucleus) with a number of thin processes radiating outward from it: usually one long axon conducts signals away from the cell body toward distant targets; and several shorter branching dendrites extend from the cell body, providing an enlarged surface area to receive signals from

the axons of other nerve cells (Figure 6 a). The typical axon divides at its far end into many branches, passing on its message to many target cells simultaneously through synapses.

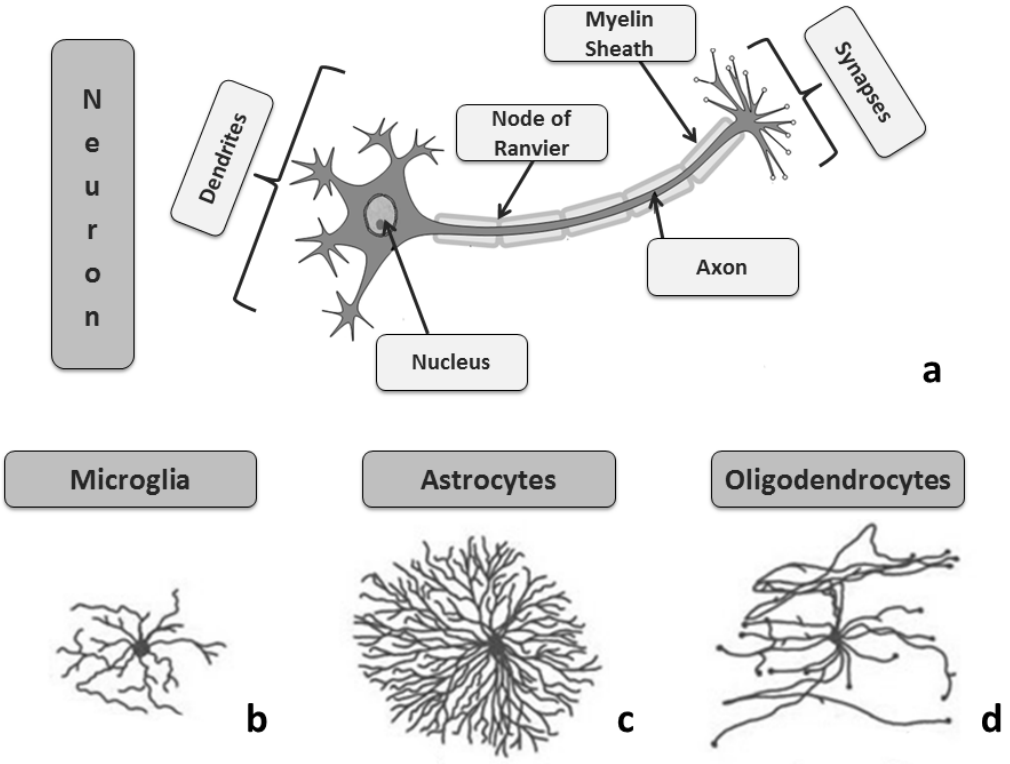

Figure 6. Neuron and glia cells.

The other type of CNS cells, glial cells, constitutes the largest majority of cells in the nervous system. Although glial cells also have complex processes extending from their cell bodies, they are generally smaller than neurons, and they lack axons and dendrites (Figure 6 b, c and d). This implies that glia cells do not participate directly in synaptic interactions and electrical signalling, but they support neurons to define synaptic contacts and to maintain the signalling abilities. Moreover, they modulate the rate of nerve signal propagation, modulate synaptic action by controlling the uptake of neurotransmitters, provide a scaffold for some aspects of neural

development, and help in (or preventing, in some instances) recovery from neural injury. Glia cells of the central nervous system generally fall into three categories: microglial cells, astrocytes, and oligodendrocytes. The former is referred to small cells derived from hematopoietic stem cells and with properties similar to tissue macrophages (Figure 6 b). They, in fact, are primarily scavenger cells that remove cellular debris from sites of injury or normal cell turnover. Astrocytes have a starlike appearance (hence the prefix 'astro') due to their elaborate local processes (Figure 6 c). The major function of astrocytes is to maintain, in a variety of ways, an appropriate chemical environment for neuronal signalling. Finally, oligodendrocytes surround and insulate some neurons axons with a laminated, lipid-rich wrapping called myelin (Figure 6 d).

The reasons why some axons are myelinated and others are not are still debated. In general, it seems that a minimum calibre is required (~1 μm) before an axon can be myelinated, but how axons of a minimum calibre are selected for myelination is still not understood [5]. Moreover, the myelinated axons are not equally distributed in the CNS. White matter, in fact, is essentially composed of myelin sheath, which comprises about 50% of the total dry weight and is responsible for its colour and for the gross chemical differences between white and grey matter [1].

The process of creating a myelin sheath around axons is called myelination and it occurs when the processes of mature oligodendrocytes contact axons [6] (Figure 7 a, b and c).

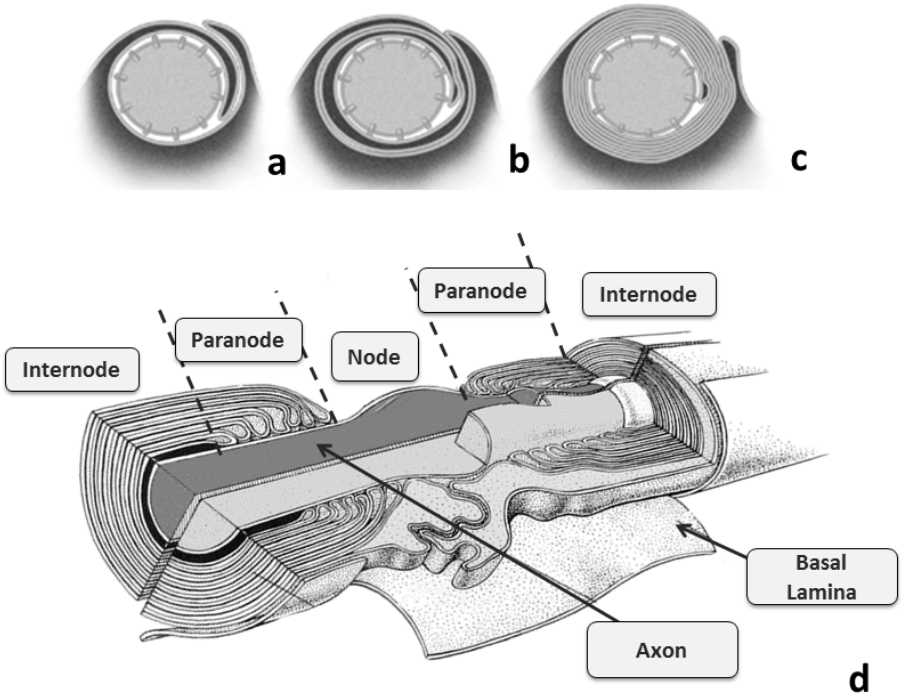

Figure 7. The process of myelination (a, b, c) and the resulting sheath (d).

This process depends mainly on cell surface and extracellular matrix molecules which promote interactions between myelin and axons [7]. More in detail, myelin synthesis is triggered when the elongated oligodendrocyte processes make contact with nearby axons and form a cup at the point of contact, extending lengthwise to form a trough whose two lips advance around the circumference of the axon until they meet. One then passes beneath and rotates many times around the axon to form the multiple membrane layers or lamellae. The developing myelin sheath extends lengthwise in both directions along the axon to form an internodal segment (Figure 7 d). But at the advancing edge, each layer of the spiral retains a bead of cytoplasm where the two inner leaflets of the surface membrane remain separate. In three dimensions, this bead comprises a ring of cytoplasm around the axon and is termed the lateral loop. Transverse bands, regularly arranged sites of close membrane apposition space 10-15 nm apart, later develop between the end of each lateral loop

and the underlying axon. There are as many lateral loops at the leading edge of the advancing sheath as there are lamellae, and these become stacked in a regular way with a periodicity of 12 nm. The complement of lateral loops at one end of each developing internode almost abuts onto its adjacent counterpart, and together these form the paranodal region next to nonmyelinated regions, called nodes of Ranvier (Figure 7 d). During compaction, the cytoplasmatic content of all except the inner- and outermost lamellae of the developing spiral sheath is gradually extruded, and the two inner leaflets of the surface membrane lipid bilayer thus become opposed. They then fuse to form the major dense line visible in ultrastructure cross-sections (Figure 8).

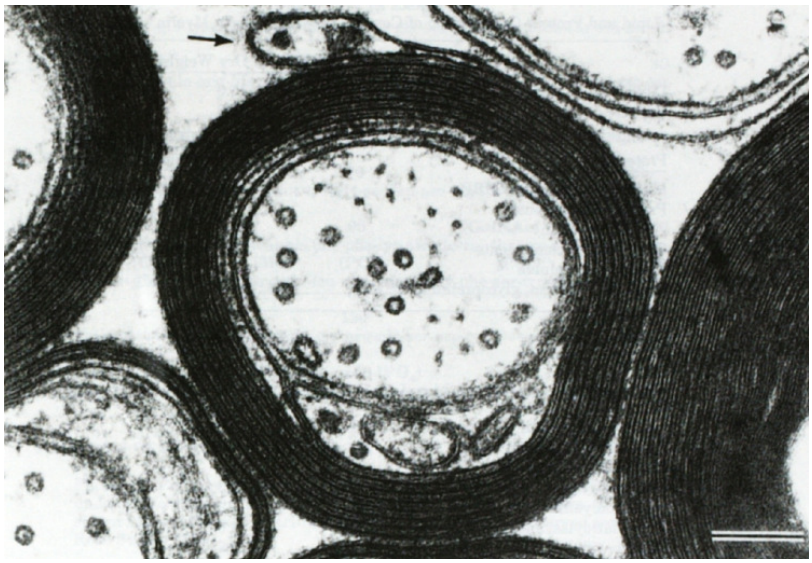

Figure 8. Electron micrograph of mature myelin sheath (from [8]).

Inner and outer tongues of cytoplasm remain where the corresponding central and outermost lamellae have not compacted. Compact myelin thereby consists of a condensed lipid-rich membrane wrapped spirally many times around axons to form a segmented sheath. Thus, the resulting content of myelin is composed of water (40%), lipid (70-85% of the dry mass), and proteins (15-30% of the dry mass) [9].

The myelin structure described above, in particular its thickness, its low water content, and its richness in lipids favour rapid nerve conduction velocity. The myelin sheath, in fact, is responsible for a type of conduction which is considerably faster than continuous propagation of the nerve impulse [1]. In unmyelinated axons, impulse conduction is propagated by local circuits of ion current that flow into the active region of the axonal membrane, through the axon, and out through adjacent sections of the membrane. These local circuits depolarize the adjacent piece of membrane in a continuous sequential fashion. In myelinated axons, instead, the excitable axonal membrane is exposed to the extracellular space only at the nodes of Ranvier, where sodium channels are located. When the membrane at the node is excited, the local circuit generated cannot flow through the high-resistance sheath and therefore flows out through and depolarizes the membrane at the next node. The low capacitance of the sheath means that little energy is required to depolarize the remaining membrane between the nodes, which results in an increased speed of local circuit spreading. Since active excitation of the axonal membrane jumps from node to node, this type of conduction is called ‘saltatory conduction’ (Latin ‘saltare’, ‘to jump’).

After understanding the structure and the function of myelin, its importance is clearly outstanding. If the myelin sheath surrounding the nerve axon is, in fact, damaged or destroyed, transmission of nerve impulses is slowed or blocked leading to serious diseases (such as multiple sclerosis and leukoencephalitis). Different patterns of myelin abnormal formation (i.e., dysmyelination) or damage (i.e., demyelination) have been observed [10]. In active primary demyelination, for instance, the focal removal of myelin sheaths is accompanied by an infiltration of macrophages that quickly accumulate myelin debris and become transformed in fat-filled macrophages. In partial demyelination, instead, the dimensions of myelin sheaths are irregularly reduced; internodes of normal length may be too thin for the diameter of the axon they enclose, or short, thinly myelinated axons are interposed between normal size internodes. Any kind of damage of the myelin sheath causes changes in the electrical properties of the brain related to myelin loss and in the electrogenic features related

to alterations of the molecular organization within the axonal membrane that lead to conduction abnormalities. One of those major changes is the dispersion of Na^+ and K^+ channels observed in experimental models of demyelination [11, 12]. Na^+ channels, in fact, are no longer concentrated exclusively at the nodes of Ranvier, but a diffuse distribution along the naked demyelinated axon is reported. However, loose clusters of Na^+ channels persist on some denuded axons. The same pattern is observed in the distribution of potassium channels. Moreover, nodal and internodal axonal molecules, that are generally specific of nodal or internodal region, are now diffusely distributed along the naked axons [13, 14]. These changes impair definitively the transmission of nerve impulses.

1.3. Demyelinating diseases: the example of Multiple Sclerosis

Multiple sclerosis (MS) is a one of the most important inflammatory disease of CNS with a high incidence among Northern Europeans and white US population [15]. Moreover, MS is twice more common in women than men. However, men have a tendency for later disease onset with worse prognosis, supporting gender-dependent factors in etiology and phenotypic variability [16]. Even if the pathogenesis is still debated, the central hypothesis is that T lymphocytes with receptors for CNS myelin components enter the brain, respond locally to their target antigen, and 'indirectly' attack local cells [17]. These autoaggressive T cells trigger an inflammatory cascade that results in demyelination, loss of oligodendrocytes and axonal degeneration. Macroscopically, at the nervous system level, this inflammation is responsible for the generation of scars (scleroses or plaques or lesions) in which a substantial axonal damage has been described [18-21]. Typical lesions are usually small, round or oval in shape and may occur in any part of the central nervous system where myelin

exists. Although MS is a white matter disease, 5–10% of the lesions may involve the grey matter including cerebral cortex and basal ganglia [22]. At the onset, the resulting interruption of myelinated axons in CNS causes the symptoms typical of MS [17]: weakness or diminished dexterity in one or more limbs, a sensory disturbance, monocular visual loss, double vision, gait instability, and ataxia. As the disease worsens, bladder dysfunction, fatigue, and heat sensitivity occurs in most patients. Cognitive deficits are also common, especially in advanced cases, and include memory loss, impaired attention, problem-solving difficulties, slowed information processing, and difficulties in shifting between cognitive tasks. To quantify and monitor changes in the level of disability over time, the Kurtzke Expanded Disability Status Scale (EDSS) is the gold-standard measure [23]. The scale measures impairment or activity limitation based on the examination of eight functional systems (FS, i.e. areas of the central nervous system which control body functions): pyramidal (ability to walk), cerebellar (coordination), brainstem (speech and swallowing), sensory (touch and pain), bowel and bladder functions, visual, mental, and other (includes any other neurological findings due to MS). The examination results in a score ranging from 0 (normal neurologic examination) to 10 (death due to MS) in half-point increments (Table 1).

Table 1. EDSS score.

EDSS	Examination
0.0	Normal neurological exam.
0.5	/
1.0	No disability, but minimal signs in one FS are present.
1.5	No disability, but minimal signs in more than one FS are present.
2.0	Minimal disability in one FS is present.
2.5	There is mild disability in one FS or minimal disability in two FS.
3.0	There is moderate disability in one FS or mild disability in three or four FS. However, the person is still able to walk.
3.5	The person is still able to walk, but has moderate disability in one FS and mild

	disability in one or two FS; or moderate disability in two FS; or mild disability in five FS.
4.0	The person is still able to walk 500 meters without aid or rest, and is up and about most of the day (12 hours) despite relatively severe disability.
4.5	The person is still able to walk 300 meters without aid, and is up and about much of day. He or she is able to work a full day, but may otherwise have some limitations of full activity or require minimal assistance. This is considered relatively severe disability.
5.0	The person is able to walk 200 meters without aid or rest. Disability impairs full daily activities, such as working a full day without special provisions.
5.5	The person is able to walk 100 meters without aid or rest. Disability precludes full daily activities.
6.0	The person needs intermittent or unilateral constant assistance (cane, crutch or brace) to walk 100 meters with or without resting.
6.5	The person needs constant bilateral support (cane, crutch or braces) to walk 20 meters without resting.
7.0	The person is unable to walk beyond five meters even with aid, and is essentially restricted to a wheelchair. However, he or she wheels self and transfers alone, and is active in wheelchair about 12 hours a day.
7.5	The person is unable to take more than a few steps and is restricted to wheelchair, and may need aid to transfer. He or she wheels self, but may require a motorized chair for a full day's activities.
8.0	The person is essentially restricted to bed, a chair or a wheelchair, but may be out of bed much of day. He or she retains self-care functions and has generally effective use of arms.
8.5	The person is essentially restricted to bed much of day, but has some effective use of arms and retains some self-care functions.
9.0	The person is confined to bed, but still able to communicate and eat.
9.5	The person is totally helpless and bedridden and is unable to communicate effectively or eat and swallow.
10.0	Death due to MS.

Based on the symptoms, level of disability and the progression of the disease, three different major forms of MS can be detected [24, 25]:

1. Relapsing-Remitting Multiple Sclerosis (RRMS) is the most common form of MS, reaching almost 85% of patients. It is characterized by clearly defined attacks of worsening neurologic function. These attacks (i.e. relapses, flare-ups, or exacerbations) are generally followed by partial or complete recovery periods (remissions), during which symptoms improve and there is no apparent worsening or progression of disease.
2. Primary-Progressive MS (PPMS) is a less common form, affecting 10% of MS patients. The onset of this type is slow, but there is a steady worsening of neurologic functioning, without any distinct relapses. A person's rate of progression may vary over time with occasional plateaus or temporary improvements, but the progression is still continuous.
3. Secondary-Progressive MS (SPMS) may follow after having RRMS. There may be a break from this type of MS or the symptoms can remain constant with no break from the disease. It may result in a progressive disability for some people. 50% of people with Relapsing-Remitting MS will have developed some form of the Secondary-Progressive MS within 10 years.
4. Progressive Relapsing MS (PRMS) is the rarest type of MS, affecting only 5% of patients. It is characterized by steadily worsening disease from the beginning, but with occasional relapses along the way. People with this form of MS may or may not experience some recovery following these attacks, but the disease continues to progress without remissions.

In addition to these four types, a clinically isolated syndrome (CIS) has been described in which a first neurologic episode that lasts at least 24 hours occurs [24, 25]. It is caused by inflammation/demyelination in one or more sites in the central nervous system, leading respectively to single or more than one neurological symptom.

Relapses in the first years, occurrence of progressive phase and disability seem to be the most reliable prognostic factors for MS [26]. It is well established, in fact, that the evolution to an irreversible disability takes longer in patients with an exacerbating–remitting onset, compared to those with a progressive one. The transition from a relapsing-remitting phase to a secondary progression is also associated with a worse evolution. Factors related to relapses, as a mono-symptomatic onset, a complete recovery, a long time interval between the first and the second relapse, and a lower number of relapses within the first years, have consistently been associated with a better prognosis. Another clinical factor is strongly and consistently associated with the time course of disability: age at MS onset. It is accepted that a younger age at onset is related to a slower disease progression and therefore a better prognosis [27]. The clinical and epidemiological dissociation between relapses and disability accumulation in the long term is not contradictory with a short-term influence of relapses on MS course. For example, it has been shown many times that the higher the number of relapses in the first years of the disease, the shorter the time from disease onset to assignment of irreversible disability scores [28]. Unfortunately, despite important advances in therapeutics for MS, there is not an available drug that is able to significantly alter the long-term natural history of the disease [29-31].

1.4. Basic principles of magnetic resonance relaxation

Magnetic resonance imaging (MRI) has played an expanding and unique role in the diagnosis and management of different diseases, including multiple sclerosis, since the beginning of its application by Young et al. in this field [32, 33]. The initial evaluation of a patient suspected of MS, in fact, starts with MRI thanks to its

sensitivity to depict focal white matter abnormalities and clinically silent lesions. Despite their limitations to demonstrate diffuse damage to the white matter, neuroaxonal degeneration and irreversible demyelination, conventional T_2-weighted and T_1-weighted images are currently the standard assessment methods to confirm or reject the clinical diagnosis [34]. MRI is also used as a prognostic tool at the first presentation in patients with CIS [22, 35].

Briefly, MRI is based on the interaction of nuclear spin with an external magnetic field B_0 [36]. More in details, when a set of proton spins are placed in a strong magnetic field, B_0 (such as the MRI scanner), the individual spins align either parallel (with a lower energy state) or antiparallel (with a higher energy state) to the direction of the external field (z-axis) (Figure 9 b).

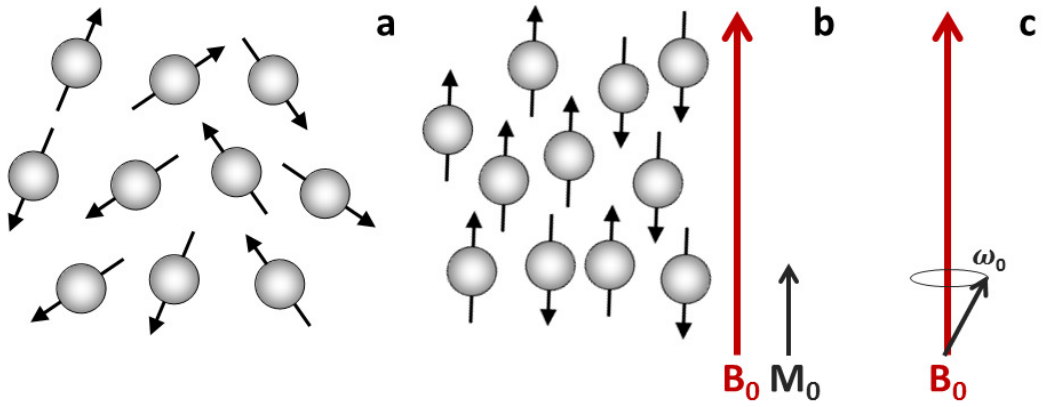

Figure 9. Principles of magnetic resonance: in a collection of protons, their tiny moments are randomly aligned (a); when placed in a large magnetic field (B_0), protons orient with the field, with slightly more in the parallel direction, producing the net magnetic moment (M_0) that is the basis for MRI signal (b); and, which, precesses about the direction of B_0 at the Larmor frequency (c).

At equilibrium, slightly more protons are aligned in the parallel orientation, resulting in a small but measurable net magnetic vector, M_0. If tilted away from the direction of B_0, this vector precesses about the external field at a specific frequency (the Larmor frequency) equal to B_0 multiplied by the so called proton gyromagnetic ratio (i.e. a constant value characteristic of each nucleus). At 1.5 T, the Larmor frequency for protons is 1.5 T × 42.58 MHz/T ≈ 64 MHz, just below the bottom end of the FM radio spectrum. In other words, a radiofrequency (RF) pulse applied at Larmor frequency tilts the magnetic vector away from the direction of B_0 into the transverse plane (xy-plane), producing a net magnetic moment in that plane (Figure 9 c). Transverse magnetization, in fact, results when an RF pulse tips the longitudinal magnetization away from the z-axis toward the transverse xy-plane: in particular, a 90° RF pulse tips the magnetization all the way into the xy-plane; while a 180° RF pulse (twice as strong or twice as long as a 90° pulse), tips the magnetization so it's pointing down, along the z-axis. This transverse magnetization is the source of the signal measured in MRI. When the RF pulse is removed, the magnetization recovers back to equilibrium, with the individual spins returning to their original parallel or antiparallel direction and dephasing in the transverse plane. The signal produced is caused by freely rotating, decaying transverse magnetization and it is called Free Induction Decay (FID).

The rate of return of the longitudinal magnetization and the rate of loss of the transverse magnetization are described by 3 characteristics: T_1, T_2, and T_2^* relaxation times.

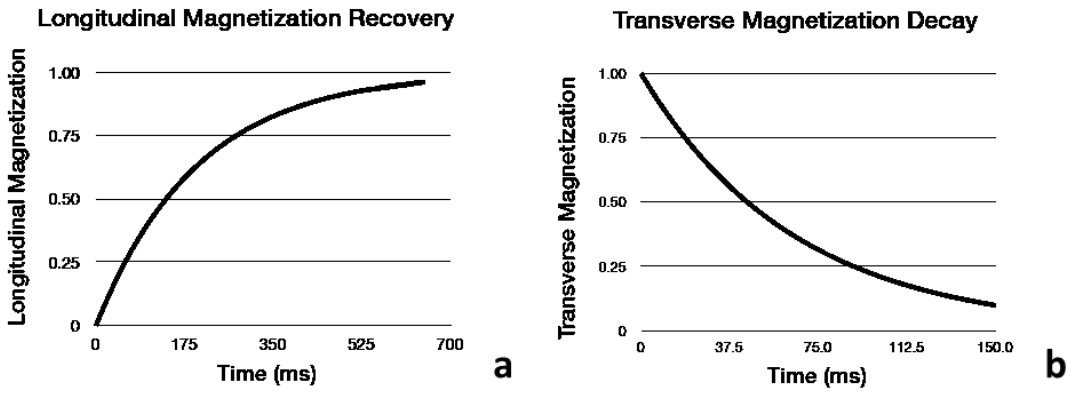

Figure 10. T_1 and T_2 relaxation times: when RF is removed, the protons return to their equilibrium orientation with rate $1/T_1$ and the net longitudinal magnetization recovers (a); while the net transverse magnetization decays with rate $1/T_2$ (b).

T_1 indicates the re-growth of the longitudinal magnetization (Figure 10 a), while T_2 and T_2^* describe the loss of phase coherence of the transverse magnetization (Figure 10 b). Since these processes of relaxation are driven by molecular motion, interaction, and energy exchange, T_1 relaxation represents an exchange of energy between water protons and protons attached to other macromolecules (lattice). Hence, T_1 is also referred to as the spin–lattice relaxation time. T_2 relaxation, instead, reveals exchanges of energy between the water protons themselves. For this reason, T_2 is called the spin–spin relaxation time. In these terms, it is clear that T_1 relaxation is an energy-loss process, while T_2 relaxation is an energy-conserving process. Similarly to T_2, T_2^* describes the decay of transverse magnetization, taking into account the macroscopic inhomogeneities of the external magnetic field and the presence of large paramagnetic molecules with different magnetic susceptibilities from tissue. Since these relaxation times derive from random molecular motion and proton–proton interactions, they are directly influenced by the local biophysical and biochemical environments and, therefore, contain information reflective of these environments, including tissue density (i.e. water content and mobility),

macromolecule, protein and lipid composition, paramagnetic atom (like iron) concentration, and other pathologically related characteristics [37]. Thus, T_1 and T_2 differ for tissues with different composition, and changes in T_1 and T_2 are indicative of tissue changes associated with disease or other biological processes, (such as learning, neuroplasticity, aging and so on). For example, typical T_1 and T_2 values of water content in normal tissue are roughly 1000 ms and 50 ms, respectively., while T_1 and T_2 of pathological tissue usually become longer than those [36].

To exploit the properties of relaxation times in mirroring tissue features with the aim of determining a good MRI contrast, different pulse sequences have been designed. The pulse sequences are sets of defined RF and gradient pulses repeated many times during a scan. They are divided into two major categories: spin echo (SE) and gradient echo sequences (GRE) [36].

Spin echo sequences are generated when a 90° pulse and a 180° pulse are applied sequentially. As mentioned before, the purpose of the 180° pulse is to refocus the phase of the protons, causing them to regain coherence and thereby to recover transverse magnetization, producing a spin echo. Following the spin echo, coherence is again lost as the protons continue to resonate at slightly different frequencies due to non-uniformities in the main magnetic field. If another 180° pulse is applied, coherence can again be established for a second spin echo and this pattern can be repeated forming an echo train. The deriving spin echo signal is given by:

$$S_{SE} = \rho_H \left[1 - \exp(-\frac{TR}{T_1})\right] \exp(-\frac{TE}{T_2})$$

where

- ρ_H is a constant proportional to the proton density;
- TE is the echo time, i.e. the time between the 90° RF pulse and the peak of the echo signal. The 180° RF pulse is applied at time $TE/2$;

- TR is the repetition time, i.e. the time between 2 excitations pulses (time between two 90° RF pulses).

From this formulation, T_2-weighting increases with long TE and TR, while T_1-weighting increases with a short TE and TR (Table 2). Proton Density weighting is, instead, characterized by a short TE and a long TR (Table 2).

Table 2. T_1- and T_2-weighted images.

Parameter Weighted Spin Sequences		
	$TR \ll 1000\ ms$	$TR \gg 1000\ ms$
$TE \ll 50\ ms$	T_1-weighted images	Proton Density Images
$TE \gg 50\ ms$	Not used	T_2-weighted images

Especially the T_2- and the T_1-weighted images are highly sensitive for detection of MS lesions.

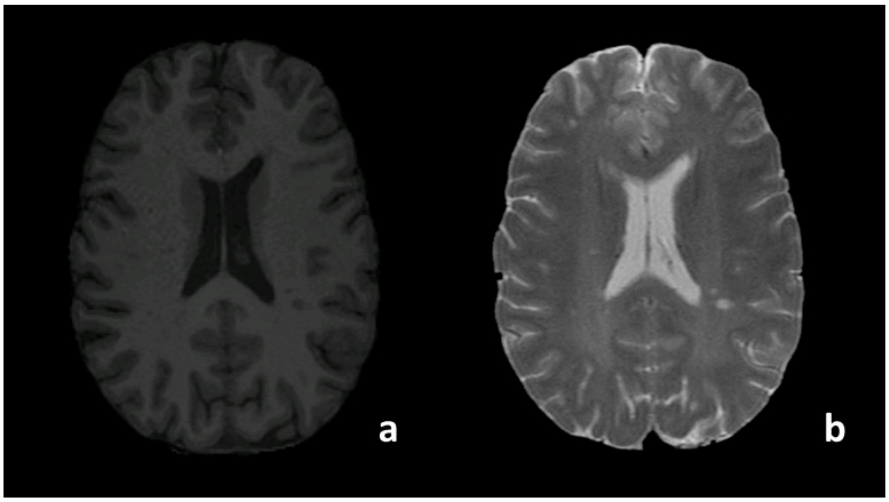

Figure 11. T_1- (a) and T_2- (b) weighted images.

Generally, on T_2-weighted images, lesions appear as hyperintense regions (Figure 11 b). The less common grey matter lesions are usually small with intermediate-high signal intensity and a less sever degree of inflammation, which may cause the obscure appearance of this kind of lesions on MR imaging compared with that of white matter lesions [38]. With T_2-weighted images, another abnormality in MS patients is highlithed: the grey matter hypointensity. Such hypointensities are thought to represent pathologic iron deposition [39]. T_2-hyperintense MS lesions may appear hypointense on corresponding T_1-weighted images (Figure 11 a). In general, most profound hypointensity is a sign of permanent lesions, pathologically correlated with the most profound demyelination and axonal loss [40].

GRE, the other sequences type, differs from the spin echo sequence because the flip angle (FA or α, i.e. the angle to which the net magnetization is rotated relative to the main magnetic field direction through the application of a RF excitation pulse at the Larmor frequency) is usually below 90° and there is not a 180° RF rephasing pulse. A flip angle lower than 90° decreases the amount of magnetization tipped into the transverse plane, causing a faster recovery of longitudinal magnetization, thus shorter

TR/TE and decreased scan time. However, TR reduction may cause that the transverse magnetization is completely disappeared at the onset of the following repetition and is submitted to the flip caused by the excitation pulse. Depending on how this residual transverse magnetization is managed, two main classes of gradient echo sequence can be distinguished: gradient echo sequences with spoiled residual transverse magnetization (such as SPGR); and steady state gradient echo sequences that conserve residual transverse magnetization and therefore participate in the signal (like SSFP).

The SPGR (or SPoiled Gradient Recalled echo) 'spoils' (or destroys) the transverse magnetization by adding a phase shift to successive RF pulses during the acquisition. By shifting the residual transverse components out of phase, in fact, the buildup of the transverse steady-state signal does not occur, effectively eliminating the T_2^* dependency of the signal. Although small T_2^* contributions are introduced by the gradient reversal, short TR, short TE, moderate to large flip angle, and spoiled transverse magnetization produces the greatest T_1 contrast.

The SSFP (Steady-State Free Precession), instead, applies strings of RF pulses rapidly and repeatedly with TR short compared to both T_1 and T_2. In so doing, the signal never completely decays, implying that the spins in the transverse plane never completely diphase, thus the flip angle and the TR maintain the steady state.

These two sequences establish the base of DESPOT1 (Driven-equilibrium single-pulse observation of T1) and DEPOT2 (Driven-equilibrium single-pulse observation of T2), which represent one of the most rapid, accurate and precise methods to evaluate the longitudinal and transverse relaxation times [41, 42]. DESPOT1 and DESPOT2 use respectively SPGR and bSSFP (fully-balanced SSFP, i.e. is a special type of SSFP sequence where the gradient-induced dephasing within TR is exactly zero [43]) data acquired over a range of FA with constant TR. These methods allow a significantly faster measure of T_1 and T_2 than the other traditional methods. The combination of DESPOT1 and DESPOT2, in fact, permits the acquisition of whole-

brain (25x25x10 cm), high spatial resolution (1 mm^3 isotropic voxels) T_1 and T_2 maps in clinically feasible 15 minutes acquisition [41], compared to, for instance, an acquisition time of about 20 minutes per slice of CPMG spin-echo sequence [42, 44].

1.5. Multiple component relaxation: the mcDESPOT method

Despite their advantages, both DESPOT1 and DESPOT2 are based on the hypothesis that the relaxation in each voxel is characterized by a combination of a single T_1 and a single T_2. In other words, this hypothesis implies the assumption that there is only a single water environment in each voxel. Unfortunately, this assumption is far from the real case, in which the water is compartmentalized into multiple distinct micro-anatomical environments, each with unique biophysical and biochemical features, and, therefore, distinct T_1 and T_2 relaxation times [45]. Moreover, if the boundaries between these compartments are permeable to water, protons may easily exchange between them. In this scenario, the T_1 or T_2 value computed so far represent a weighted average of the compartmental T_1 and T_2 values and exchange rate [45]. Assuming, thus, the brain tissue inhomogeneity, a four-pool model was suggested [46, 47]. The four pools are referred to the 4 main species that could be present in a voxel: myelin tissue (non-aqueous protons), water trapped between the lipid bilayers of the myelin sheath, other tissue different from myelin (non-aqueous protons), and water in the intra- and extra-cellular spaces. The quantification of the myelin tissue is fundamental for a better understanding of multiple sclerosis, but also of many other diseases. Unfortunately, this assessment is not possible with the current MRI techniques, since the non-aqueous proton signal decays to zero in less than 100 µs, while the signal of water in tissue has T_2 times longer than 10 ms [48-50]. However,

pathological changes in neurodegenerative diseases, in general, and in MS, in particular, affect directly the organization of non-aqueous molecules in cellular structures, and indirectly the quantity of water in the same structures. So, the previous four-pool model can be reduced in a two-pool one, in which each pool characteristics (T_1 and T_2 relaxation times) can be addressed with the current technology. This model, called mcDESPOT (MultiComponent-Driven Equilibrium Single-Pulse Observation of T1 and T2), is based, in fact, on the existence of two water environments (Figure 12): one referred to the intra- and extra-cellular water (F, free water), and the other to the water trapped between the hydrophobic lipid bilayers of the myelin sheath (M, myelin-associated water) [51, 52]. Quantification of this latter component provides a non-invasive means of measuring and monitoring myelin content in, for instance, multiple sclerosis [53].

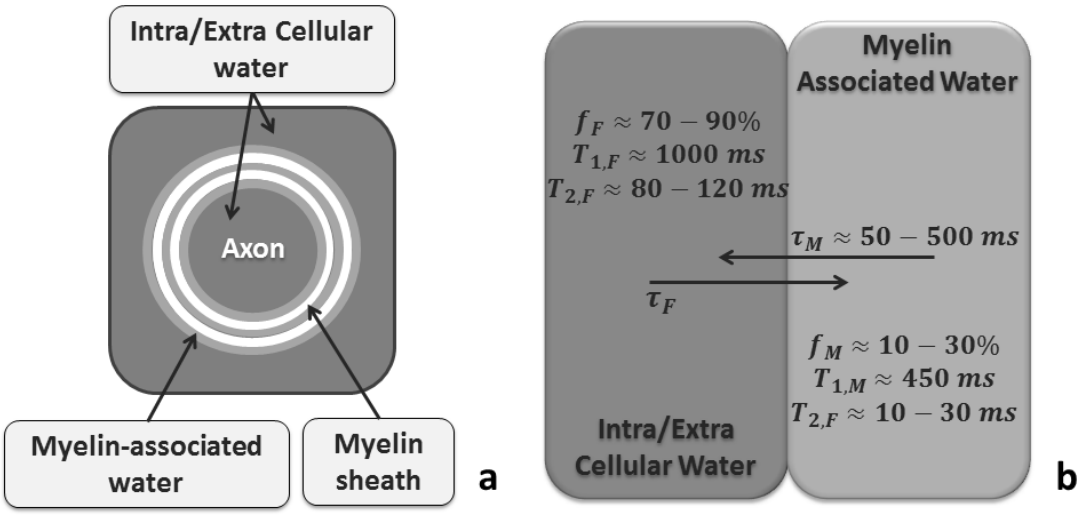

Figure 12. Multicomponent relaxation theory: a simple model of brain tissue contains two water components, free intra- and extra-cellular water and water trapped between the lipid bilayers of the myelin sheath (a); characteristic values of parameters of the two pool (b).

More in details, mcDESPOT is an evolution of previous techniques (DESPOT1 and DESPOT2 [41, 54]) and it combines SPGR and bSSFP acquired over a range of flip angle (α) and with constant TR, to derive properties of those two physically separated but exchanging species, F and M. These properties are represented by free-water T_1 and T_2 ($T_{1,F}$,$T_{2,F}$), myelin-associated water T_1 and T_2 ($T_{1,M}$,$T_{2,M}$), relative myelin and free-water volume fractions (f_M,f_F), and the myelin and free-water proton residence times (τ_M,τ_F). The latter are the average time a proton is expected to remain in a compartment before exchanging to the other. To derive those parameters, the general Bloch-McConnell magnetization equations [55] are modified for obtaining the closed form expressions of SPGR and bSSFP signals (S_{SPGR} and S_{bSSFP}, respectively).

The formulation that describes the two component SPGR signal involves only the longitudinal magnetization components:

$$S_{SPGR} = M_{SPGR}\left(I - e^{A_{SPGR}TR}\right)\sin\alpha \times \left(I - e^{A_{SPGR}TR}\cos\alpha\right)^{-1} \quad [1]$$

where

- $M_{SPGR} = \rho[f_M \quad f_F]$ is the magnetization that arises from the two species described by the volume fractions of myelin-associated water (f_M) and free water (f_F). Those fractions are weighted by a factor (ρ) proportional to the equilibrium longitudinal magnetization;
- I is the 2x2 identity matrix;
- $A_{SPGR} = \begin{bmatrix} -\frac{1}{T_{1,M}} - \frac{1}{\tau_M} & \frac{1}{\tau_F} \\ \frac{1}{\tau_M} & -\frac{1}{T_{1,F}} - \frac{1}{\tau_F} \end{bmatrix}$ is a matrix containing the T_1 and the exchange information of the two species. In particular, the T_1 relaxation of myelin-associated water is represented by $T_{1,M}$, while the T_1 relaxation of free water is $T_{1,F}$. The exchange rates are identified by the mean residence times (τ_M for M and τ_F for F);

- TR is the repetition time;
- α is the flip angle.

Extension of the above analysis, to include the x and y magnetization components, leads to the equation for bSSFP signal:

$$S_{bSSFP} = \sqrt{\left(M_{x,M}^2 + M_{y,M}^2\right) + \left(M_{x,F}^2 + M_{y,F}^2\right)} \quad [2]$$

where the elements $M_{x,M}, M_{y,M}, M_{x,F}, M_{y,F}$ compose the magnetization vector M_{bSSFP}

$$M_{bSSFP} = \left[M_{x,M} \;\; M_{x,F} \;\; M_{y,M} \;\; M_{y,F} \;\; M_{z,M} \;\; M_{z,F}\right]^T$$

This vector is specified by the following equation

$$M_{bSSFP} = \left(e^{A_{bSSFP}TR} - I\right)A_{bSSFP}^{-1}C \times \left[I - e^{A_{bSSFP}TR}R(\alpha)\right]^{-1}$$

where

- $$A_{bSSFP} = \begin{bmatrix} -\frac{1}{T_{2,M}} - \frac{1}{\tau_M} & \frac{1}{\tau_F} & \theta_{RF} + \Delta\omega_M & 0 & 0 & 0 \\ -(\theta_{RF} + \Delta\omega_M) & 0 & -\frac{1}{T_{2,M}} - \frac{1}{\tau_M} & \frac{1}{\tau_F} & 0 & 0 \\ 0 & -(\theta_{RF} + \Delta\omega_F) & \frac{1}{\tau_M} & -\frac{1}{T_{2,F}} - \frac{1}{\tau_F} & 0 & 0 \\ 0 & 0 & 0 & 0 & -\frac{1}{T_{1,M}} - \frac{1}{\tau_M} & \frac{1}{\tau_F} \\ 0 & 0 & 0 & 0 & \frac{1}{\tau_M} & -\frac{1}{T_{1,F}} - \frac{1}{\tau_F} \end{bmatrix}$$

  is a matrix containing T_1 and T_2 relaxation, exchange, off-resonance effects ($\Delta\omega_M, \Delta\omega_F$, effects generated when the transverse phase precession is nonzero), and the phase of the applied RF pulse (θ_{RF});
- TR is the repetition time;

- I is a 6x6 identity matrix;
- $C = \rho \begin{bmatrix} 0 & 0 & 0 & 0 & \frac{f_M}{T_{1,M}\tau_M} & \frac{f_F}{T_{1,F}\tau_F} \end{bmatrix}$ is related to the equilibrium longitudinal magnetization, with a term proportional to the proton density (ρ), volume fractions of the species (f_M and f_F), T_1 relaxation information ($T_{1,M}$ and $T_{1,F}$), and mean residence times (τ_M and τ_F);
- $R(\alpha)$ is a rotation matrix defining the RF pulse with excitation flip angle α.

These equations for the two component SPGR and bSSFP signal just defined comprise 11 free parameters: the free-water T_1 and T_2 ($T_{1,F}, T_{2,F}$); the myelin-associated water T_1 and T_2 ($T_{1,M}, T_{2,M}$); the relative myelin and free-water volume fractions (f_M, f_F); the myelin and free-water proton residence times (τ_M, τ_F); the myelin and free water off-resonance values ($\Delta\omega_M, \Delta\omega_F$); and a factor ($\rho$) related to the total equilibrium longitudinal magnetization and containing additional factors including scanner amplifier gains, RF coil receive biases, etc. The total number of free-parameters in this model may be reduced to 6 thanks to four assumptions:

1. If a normalization of all signals with respect to their mean is performed, ρ is eliminated;
2. If the two water pools are on-resonance, then $\Delta\omega_F = \Delta\omega_M = 0$;
3. If only two water pools are present, then $f_F + f_M = 1$;
4. If the water pools are in exchange equilibrium, then $\frac{f_M}{\tau_M} = \frac{f_F}{\tau_F}$.

With these assumptions, equations (1) and (2) can be fit to acquired SPGR and bSSFP data to derive estimates of the 6 parameters $T_{1,M}, T_{2,M}, T_{1,F}, T_{2,F}, \tau_M$ and f_M. However, errors could be introduced into these estimates when the flip angle α deviates from the prescribed nominal value, and when the transverse phase precession ($\Delta\omega_M, \Delta\omega_F$) is nonzero. These errors, in fact, alter the measured SPGR and bSSFP signals from their theoretically predicted values [54, 56] and lead to substantive errors in the derived multicomponent parameters. In general, flip angle

errors (or B_1 errors) occur from tissue dielectric effects, while the B_0 error is caused by main magnetic field inhomogeneities, particularly accentuated near air–tissue boundaries. B_0 variations lead to off-resonance conditions in the bSSFP signal, manifesting as bands of artificially reduced signal, which deviates from the theoretical signal model [57]. To correct for these effects, an additional term is taken into account in the multiparameter fit to eliminate the off-resonance effect ($\Delta\omega = \Delta\omega_M = \Delta\omega_F$) coupled with acquisition of bSSFP data with more than one phase-cycling pattern ($\theta_{RF} = 0$, SSFP0, and $\theta_{RF} = \pi$, SSFP180). Moreover, a calibration using DESPOT1-HIFI approach is included [58], in which the supplemental acquisition of at least one inversion-prepared SPGR (IR-SPGR) image is required. IR-SPGR involves the application of a 180° inversion pulse, followed by an SPGR low-angle RF pulses. This sequence provides a strong contrast between tissues having different T_1 relaxation times and suppresses tissues like fluid or fat, helping, in so doing, to reduce the B_0 inhomogeneities.

1.6. Nonlinear search and stochastic region contraction approach

Summarizing, the three acquired pulse sequences (SPGR and two sequences of bSSFP, $\theta_{RF} = 0$ and $\theta_{RF} = \pi$) represent the target of the model fitting in which theoretical signals (i.e. theoretical SPGR, SSFP0, SSFP180) are derived using equations (1) and (2). The fitting implies the identification of the 6 (or 7, if the off-resonance effect, $\Delta\omega$, is taken into account) parameters described above. Due to its nature, the problem addressed by mcDESPOT can be considered as a nonlinear optimization problem. In this context, finding global minima is a challenging task,

especially because nonlinear constraints form feasible regions that are hard to find and difficult to deal with (Figure 13).

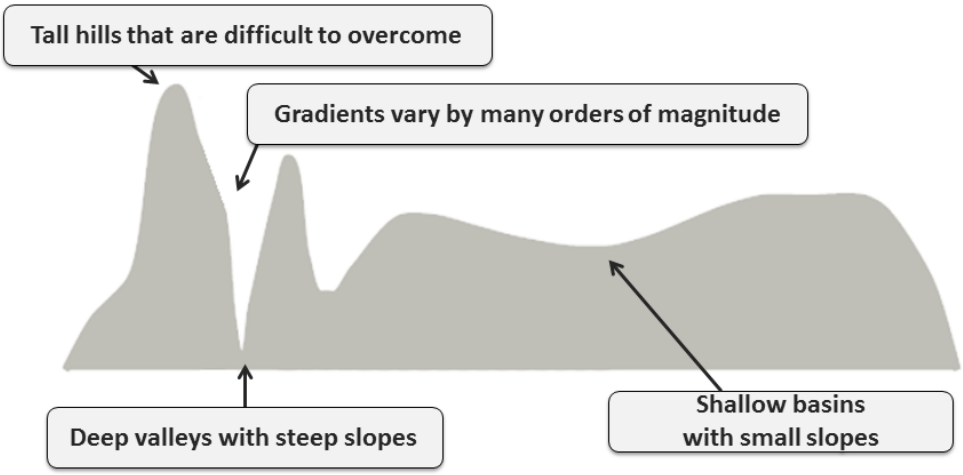

Figure 13. Difficulties that characterize the nonlinear search space.

mcDESPOT deals with the nonlinear fitting of the SPGR, SSFP0 and SSFP180 signals models to the acquired data using a particular approach called stochastic region contraction approach [59]. The outline of this method is reported in Figure 14. First of all, the solving process is performed through the implementation of two fits: one called NotSimplified, and the other Simplified fit. The differences between them regard the sequences used and the number of parameters searched. In the NotSimplified fit, in fact, all three pulse sequences are used (SPGR, SSFP0 and SSFP180) and all the 7 parameters are searched. In the Simplified fit, instead, the SSFP0 is not considered and, consequently, the two water pools are on-resonance, that means $\Delta\omega = 0$.

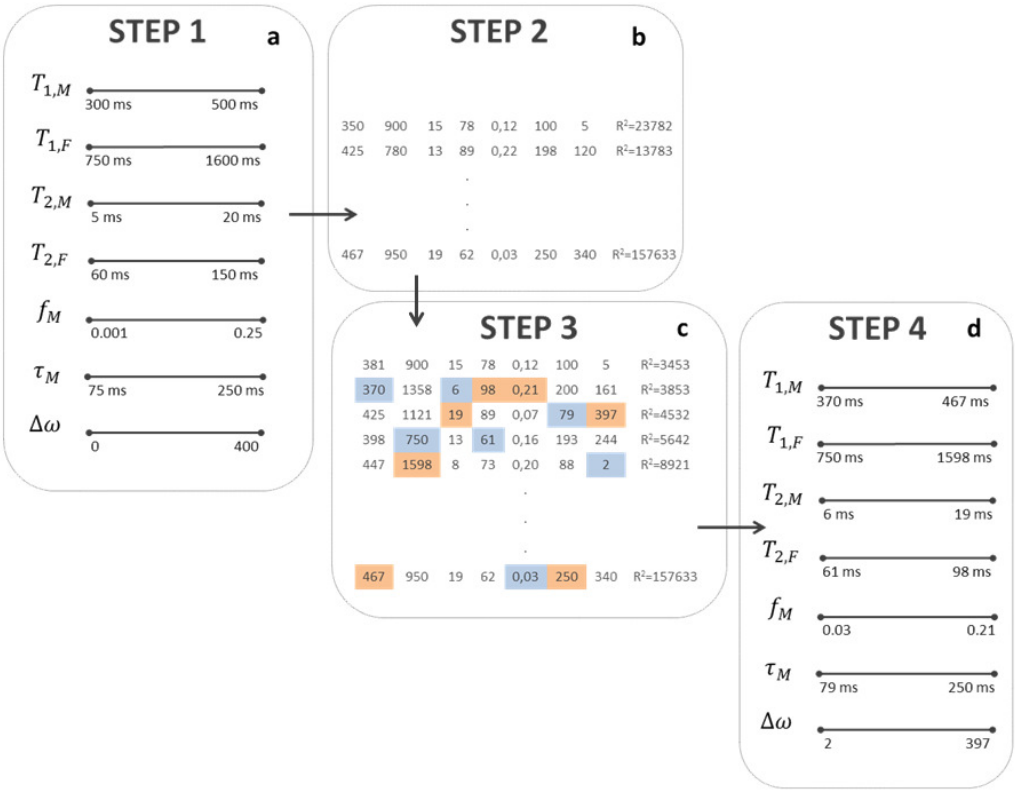

Figure 14. Outline of the stochastic region contraction approach implemented in mcDESPOT. After defining the expected search-space extents for each parameter (a), samples of $T_{1,M}, T_{2,M}, T_{1,F}, T_{2,F}, \tau_M, f_M$ and $\Delta\omega$ combinations are randomly chosen from these uniform distributions (b). For each sample, the theoretical signals are computed and the residuals between the theoretical signals and the acquired ones, both normalized respect to their mean, are calculated. The samples are then rank sorted by increasing residual and from a certain number of top samples, the minimum and maximum sampled value of each parameter is determined (c). These values are then used to update the extents of search-space (d) and the sampling process is repeated.

For each voxel, the first step of the stochastic region contraction approach consists of defining the expected search-space extents for each parameter (Figure 14 a). A certain number of samples ($N_{samples}$) of $T_{1,M}, T_{2,M}, T_{1,F}, T_{2,F}, \tau_M, f_M$ and $\Delta\omega$ combinations are randomly chosen from these uniform distributions forming, in so

doing, a set (population) of probable solutions (Figure 14 b). For each sample, the theoretical SPGR, SSFP0 and SSFP180 signals are generated using the equations (1) and (2). For each flip angle value, the residuals between the three theoretical signals and the SPGR, SSFP0 and SSFP180 acquired, both normalized respect to their mean, are calculated. The cumulative residuals are then computed across all flip angles values. The $N_{samples}$ combinations are then rank sorted by increasing residual and from a certain number of top samples ($N_{topChoices}$), the minimum and maximum sampled value of each parameter is determined (Figure 14 c). These values are then used to update the extents of search-space (Figure 14 d) and the sampling process is repeated. In this way, the search-space slowly contracts to the globally optimum solution (hence the name of the method). The algorithm continues until the difference between the minimum and maximum value of each parameter falls below a predefined threshold or a certain number of iterations ($N_{iterations}$) is reached. After the algorithm stops, the top five combinations are averaged and the result is taken as the solution. The mcDESPOT uses the options reported in Table 3.

Table 3. Options of the stochastic region contraction approach.

Option	Value
$N_{samples}$	3750
$N_{topChoices}$	50
$Threshold$	0.5%
$N_{iterations}$	5

The process just described is referred to the NotSimplified fit, since the parameter $\Delta\omega$ and SSFP0 are inserted in the routine. The Simplified fit process is equal to the previous one, except for excluding that parameter and the SSFP0 from the analysis.

After performing both fits, the average of the two solutions derived from the NotSimplified and Simplified process is taken as the final solution for the voxel considered.

1.7. Aim of the thesis

One of the key elements in the optimization algorithms, in general, and in nonlinear fitting, in particular, is the representation of the search space, i.e. the space in which solutions are sought. As mentioned before, in fact, the shape of the space for this kind of problems could be extremely complex, making it difficult to deal with. In this thesis, we address this issue in the particular case of the nonlinear fitting of mcDESPOT. In mcDESPOT, the solutions space of each voxel is scanned through the extraction of random samples. Then, the residuals associated to those samples drive the further search. However, no a priori knowledge is used to direct the search in specific regions rather than others. The only a priori knowledge used is the extent of the parameters range. With this work, we look for a priori knowledge of the search space using the information contained in the 24 volumes signals (SPGR, SSFP0 and SSFP180 across all flip angles values). The basic hypothesis, in fact, is that similar acquired signals are referred to portions of tissue that show close properties. This closeness could be translated into similar parameters combinations (i.e. similar solutions). The similarity information, thus, could be used to delineate feasible portions of space in which the global minima could be most likely placed. Assuming that the hypothesis is verified, in this way, a higher probability of avoiding local minima and reaching global one is obtained, since the search is no more dictated just

by random scans, but promising sub-spaces are provided. The effectiveness and, thus, the accuracy of the fit algorithm are improved. Moreover, introducing prior information in the search helps to address another issue typical of a nonlinear fitting: the efficiency (i.e. the computational costs). In the mcDESPOT case, for instance, the amount of computational time is due essentially to the stochastic region contraction approach. Using a single core machine, processing 128x128x86 voxels (a typical size of a MR image) takes about 7 days. Even parallelizing the code and using clusters of high-performance computers (at least 16 cores), it takes around 15 hours for one subject.

In conclusion, the aim of this thesis is to extract a priori knowledge from the MRI sequences, to relate it to tissue properties, and to introduce it into the optimization algorithm in order to increase the probability of reaching global minima in a reasonable amount of time.

2. SOM+mcDESPOT

In this chapter, the theory behind the modified version of mcDESPOT is described. Moreover, the details of the validation and application phases are reported.

2.1. Self-Organizing Maps

The Self-Organizing Map (SOM) has been proposed to model the sensory-to-cortex system mapping the unsupervised associative memory mechanism [60-64]. Visual information is processed mostly in the retina that is responsible for operations like extracting lines, angles, curves, contrasts, colours, and motion. The retina then encodes the information and sends them to the brain cortex in the left and/or right hemispheres for further processing. This processing includes the organization of the information that often involves both competition and correlative learning. When stimulus is presented, in fact, neurons compete among themselves for possession or ownership of this input. The winners then strengthen their weights or their relationships with this input. As stated in [60]: "When an axon of cell A is near enough to excite a cell B and repeatedly or persistently takes part in firing it, some growth process or metabolic changes take place in one or both cells such that A's efficiency as one of the cells firing B, is increased". This means that the change of the synaptic weight is proportional to the correlation between an input and its associated output.

Kohonen [65] abstracted the above self-organizing learning principle and function and proposed a simplified learning mechanism. Briefly, the SOM algorithm comprises two stages: a competitive and a cooperative one. In the former, the best matching neuron is selected, i.e. the "winner", and in the second stage, the weights of the winner are adapted as well as those of its immediate lattice neighbours. More in detail, the SOM uses a set of neurons, often arranged in a 2-D rectangular or hexagonal grid, to form a discrete topological mapping of an input space $S \in R^n$ (Figure 15 a). The number of neurons determines the granularity of the resulting mapping, which affects the accuracy and the generalization capability of the SOM. Each neuron *i* is represented by an *n*-dimensional weight vector, called prototype vector:

$$\boldsymbol{pv}_i = [pv_{i1}, \ldots, pv_{in}]^t$$

where n is equal to the dimension of the input vectors. Neighbourhood relation connects adjacent neurons, dictating the structure of the map. Generally the topological relations and the number of neurons are fixed from the beginning. Before the training phase, initial values are given to the weight vectors. The SOM is robust regarding the initialization, but properly accomplished it allows the algorithm to converge faster to a good solution. Typically three initialization procedures may be used: a random initialization, where the weight vectors are initialized with small random values; a sample initialization, where the weight vectors are initialized with random samples drawn from the input data set; and a linear initialization, where the weight vectors are initialized along the linear subspace spanned by the two principal eigenvectors of the input data set [66]. Good initialization can guide to a faster or even better convergence. For example, initializing the map to a principal linear sub-manifold can reduce the ordering time. In each training step, one sample vector $\boldsymbol{s}$ from the input data set is randomly chosen and a similarity measure is calculated between it and all the weight vectors of the map. The Best-Matching Unit (here denoted as BMU or $\boldsymbol{c}$), is the unit whose weight vector has the greatest similarity with the input sample. The similarity is usually defined by means of a distance measure, typically Euclidian distance. Formally the BMU is defined as the neuron for which

$$\|\boldsymbol{s} - \boldsymbol{pv}_c\| = \min_i\{\|\boldsymbol{s} - \boldsymbol{pv}_i\|\}$$

where $\|.\|$ is the distance measure. After finding the BMU, the weight vectors of the SOM are updated. The weight vectors of the BMU and its topological neighbours are moved closer to the input vector in the input space. This adaptation procedure stretches the BMU and its topological neighbours towards the sample vector (Figure 15 b).

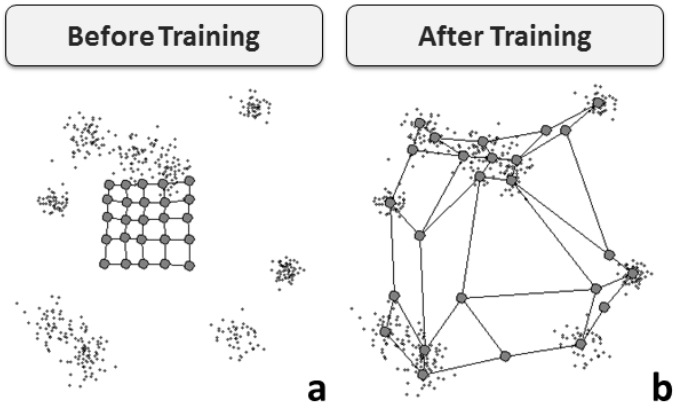

Figure 15. The SOM adapts its structure to the input vectors: the grid before the training (a) and after the adaptation (b).

The SOM update rule for the weight vector of the unit *i* is:

$$\boldsymbol{pv}_i(t+1) = \boldsymbol{pv}_i(t) + h_{ci}(t)[\boldsymbol{s}(t) - \boldsymbol{pv}_i(t)]$$

where

- t indicates time;
- $\boldsymbol{s}(t)$ is the input vector randomly drawn from the input data set at time t;
- $h_{ci}(t)$ is the neighborhood kernel around the winner unit c at time t.
- $\boldsymbol{pv}_i(t)$ is the prototype vector of the unit i at time t;
- $\boldsymbol{pv}_i(t+1)$ is the prototype vector of the unit i at time $t+1$.

The neighbourhood kernel is a non-increasing function of time and of the distance of unit i from the winner unit c. It defines the region of influence that the input sample has on the SOM. The kernel is formed of two parts: the neighbourhood function $h(d, t)$ and the learning rate function $\alpha(t)$:

$$h_{ci}(t) = h(\|\boldsymbol{r}_c - \boldsymbol{r}_i\|, t)\alpha(t)$$

where r_i is the location of unit i on the map grid. An example of neighbourhood function is the Gaussian one:

$$h(\|r_c - r_i\|, t) = \exp\left(-\frac{\|r_c - r_i\|^2}{2\sigma^2(t)}\right)$$

where $\sigma(t)$ is a suitable decreasing function of time. Usually the neighbourhood radius is bigger at first and is decreased linearly to one during the training. The learning rate is a decreasing function of time.

Also the batch training algorithm is iterative, but instead of using a single data vector at a time, the whole data set is presented to the map before any adjustments are made (hence the name 'batch'). In each training step, the data set is partitioned according to the Voronoi regions of the map weight vectors, i.e. each data vector belongs to the data set of the map unit to which it is closed. After this, the new weight vectors are calculated as:

$$pv_i(t+1) = \frac{\sum_{j=1}^{n} h_{ic}(t) s_j}{\sum_{j=1}^{n} h_{ic}(t)}$$

where $c = arg\min_k \{\|s_j - pv_k\|\}$ is the index of the BMU of data sample s_j. The new weight vector is a weighted average of the data samples, where the weight of each data sample is the neighbourhood function value $h_{ic}(t)$ at its c.

The training is usually performed in two phases. In the first phase, relatively large initial $\alpha(t)$ value and neighbourhood radius are used. In the second phase, instead, both $\alpha(t)$ value and neighbourhood radius are small compared to the beginning. This procedure corresponds to first tuning the SOM approximately to the same space as the input data and then fine-tuning the map. To guarantee convergence and stability of the map, the learning rate and neighbourhood radius are decreased at each iteration, thus converging to zero.

2.2. The modified mcDESPOT: SOM+mcDESPOT

From the previous paragraph, it is clear how the SOM can learn directly from the examples, without the need of solving functions or models, to extract patterns and perform recognition tasks preserving the topology of the input space. Moreover, SOM is able to carry out similar recognition tasks, not only on the trained data but also on unseen examples. For these reasons, SOM is depicted as a suitable and promising tool to extract a priori knowledge buried in the MRI sequences.

This a priori knowledge is built through the creation of a noise free database, in which an exclusive correspondence between combinations of the 7 parameters and the theoretical signals is established. The database is designed to explore some of the possible tissue properties that could be found in a brain. Furthermore, once defined the sequences options (such as TR, TE, α and so on), the database does not change over time and over subject, since the model that dictates the correspondence between combinations of the 7 parameters and the theoretical signals does not change. More in details, the database is formed by *in silico* voxels characterized by specific theoretical SPGR, SSFP0, and SSFP180 signals and the parameters combination ($T_{1,M}, T_{2,M}, T_{1,F}, T_{2,F}, \tau_M, f_M$ and $\Delta\omega$) used to generate those. The signals are normalized by their mean. To organize the information contained in the database revealing, thus, patterns hidden in it, the signals are queued forming a vector (signals vector) with 24 elements or volumes (i.e. one volume for each flip angle: 8 SPGR, 8 SSFP0 and 8 SSFP180). All signals vectors are then collected and used for training the SOM. The SOM is trained and the association between each voxel and its BMU (or c) is obtained. Since a sort of clustering is performed, each neuron is considered also as a cluster. Hence, clusters of similar signals are obtained.

The information got from this procedure is then used to derive the a priori knowledge that will drive the optimization algorithm in mcDESPOT. Supposing to process a subject, the algorithm followed is reported in Figure 16.

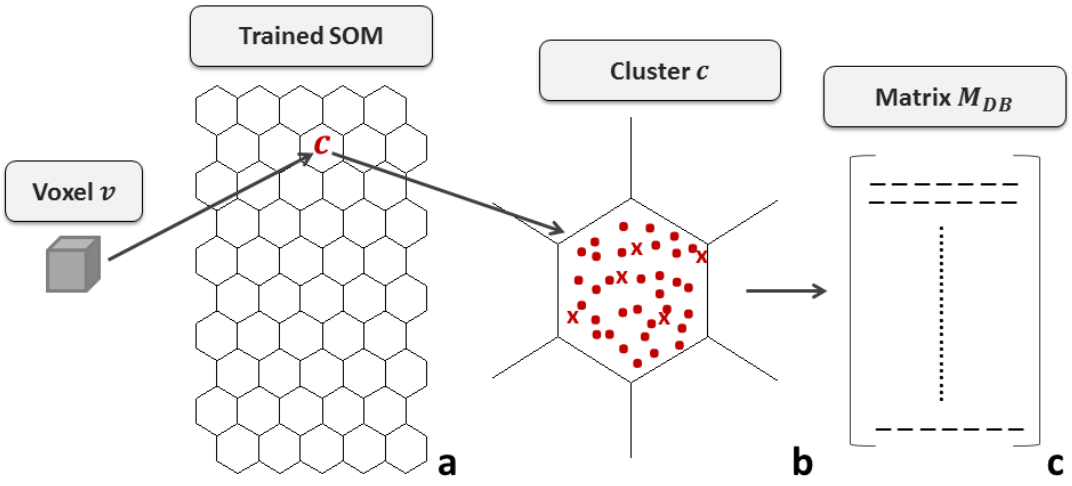

Figure 16. Process of creation of a matrix containing a priori knowledge: each voxel v is associated to its BMU (a). Since the basic hypothesis is that similar signals are associated to similar parameters, a certain number (N_{DB}) of voxels similar to v are randomly selected (b) and the corresponding parameters vectors are collected together in M_{DB} (c).

For each voxel v, its signals vector is compared to the prototype vectors of the SOM previously trained by the noise free database. The prototype vector winner is found and the BMU (i.e. the corresponding cluster, c) is obtained (Figure 16 a). Since the basic hypothesis is that similar signals are associated to similar parameters, a certain number (N_{DB}) of voxels similar to v are randomly selected (Figure 16 b) and the corresponding parameters vectors (derived by noise free data) are collected together in a matrix M_{DB} (Figure 16 c). Both the information given by c and the N_{DB} parameters vectors are saved. In the mcDESPOT, the first step of the optimization algorithm deals with the generation of a population of random solutions (or

parameters vectors). At this step, the a priori knowledge is introduced. The information previously saved (i.e. M_{DB}), in fact, is inserted. The N_{DB} solutions derived from the database replace the equivalent amount of random samples in the population. Moreover, if subject's other voxels that are mapped to c are already computed, their solutions are also used to replace other random samples of the population forming another matrix ($M_{subject}$). The size of $M_{subject}$ may vary from 0 (if no voxel belonging to c is already processed) to $N_{subject}$. If more than $N_{subject}$ voxels are previously computed, then a random choice is done to reach just that number. This process of suggesting solutions that are likely similar to the one to compute is done at the first iteration, after that, the stochastic region contraction is let run as usually. The other samples (their amount is equal to $N_{samples} - N_{DB} - N_{subject}$) are randomly chosen from the uniform distributions of the parameters. In this way, the first iteration population of the fit is composed by three contributions, two of them imputable to the a priori knowledge:

1. noise-free information that should also help to reduce the effect of noise in the computation of the parameters;
2. the current subject information that highlights the features of that particular subject's images; and
3. random samples that helps to avoid to be trapped in local minima or to drive the optimization algorithm in unfeasible region of the solutions space.

The method just described is called SOM+mcDESPOT, underlining the role of the SOM in generating the a priori knowledge that is used in the mcDESPOT.

2.3. Implementation

The Self-Organizing Maps were implemented in Matlab® (www.mathworks.com), while the mcDESPOT and its modification to take into account of the a priori information were written in C code, compiled with gcc (http://gcc.gnu.org/) and debugged with gdb (http://www.gnu.org/s/gdb/). All pre-processing was accomplished using in-house Python scripts to automate usage of the FMRIB Software Library (FSL, http://www.fmrib.ox.ac.uk/fsl/)

2.4. Validation

To assess the performances of SOM+mcDESPOT, a validation was conducted on *in silico* dataset, considering both the case of noise free and with noise, and on real images.

2.4.1. *In Silico* experiments

To investigate if it is possible to couple the similarity information contained in MRI sequences to the similarity of tissue properties (i.e. the parameters values), a small *in silico* database was created mimicking a slice of a brain: given 4525 voxels with different combinations of the 7 parameters above mentioned, theoretical SPGR and

bSSFP (SSFP0 and SSFP180) data were generated using the equations (1) and (2) with the sequences parameters reported in Table 4.

Table 4. Sequence specific parameters.

	SPGR	**IRSPGR**	**bSSFP180**
TE	1.57	2.18	1.72
TR	3.97	5.28	3.45
TI	-	-	450
α	{3,4,5,6,7,9,13,18}°	10°	{10,13,17,22,27,32,41,55}°
Voxel Volume	1x1x1.5	1x1x1.5	1x1x1.5

These signals were then normalized by their mean and queued forming the signals vectors. Depending on the presence or the absence of SSFP0, the signals vectors could have 24 (NotSimplified SOM) or 16 volumes (Simplified SOM), respectively. Effects of B0 and B1 inhomogeneities were considered zero. All signals vectors were collected and used as training set for the neural network analysis. For the SOM design, a hexagonal lattice map, a linear initialization and a batch training algorithm was chosen. 3 different size of SOM were evaluated: small (number of neurons = 52), medium (number of neurons = 85) and large (number of neurons = 340).

After trained the SOMs, to evaluate the quality of its clustering in the signals space, a simple metrics was used: the intra- and inter-cluster distances. For each cluster (c), the intra-cluster distance in the signals space ($INTRAD_c^{SS}$) was defined as the

distance between the prototype vector ($\boldsymbol{pv_c}$) of that cluster and the signal vectors ($\boldsymbol{s}$) mapped to that cluster:

$$INTRAD_c^{SS} = \|s - pv_c\|$$

In the signals space, the inter-cluster distance $INTERD_c^{SS}$, instead, was calculated as the distance among the prototype vectors:

$$INTERD_c^{SS} = \|pv_c - pv_i\|$$

with $c \neq i$. For each cluster, each signals vector was related to the 7 parameters (parameters vector or solution) that were used to generate it. In this way, an exclusive correspondence between clusters and parameters vectors was found. To evaluate if the clusters obtained in the signals space could be linearly moved to the parameters space, the intra- and inter-cluster distances relative to parameters space were also computed:

$$mp_c = \frac{1}{N_c}\sum_{k=1}^{N_c} p_{ck}\ , mp_i = \frac{1}{N_i}\sum_{k=1}^{N_i} p_{ik}$$

$$INTRAD_c^{PS} = \|p - mp_c\|$$

$$INTERD_c^{PS} = \|mp_c - mp_j\|$$

where

- N_c is the number of vectors mapped to c;
- N_i is the number of vectors mapped to the unit i;
- p_c are the parameters vectors associated to the voxels mapped to c;
- p_i are the parameters vectors associated to the voxels mapped to the unit i;
- mp_c is the mean parameters vector given by averaging all the N_c parameters vectors associated to N_c signals vectors mapped to c;

- mp_i is the mean parameters vector given by averaging all the N_i parameters vectors associated to N_i signals vectors mapped to the unit i;
- $c \neq i$.

Moreover, to check if the SOM clustering was able to identify similar (in terms of anatomy and know properties) tissue portions, a visual inspection of the clustering was sought: labelled each cluster with a number according to the topological order on the grid, the map of these labels was plotted.

To test the hypothesis that similar acquired signals imply similar parameters, the suggesting process designed for the SOM+mcDESPOT was simulated (Figure 17).

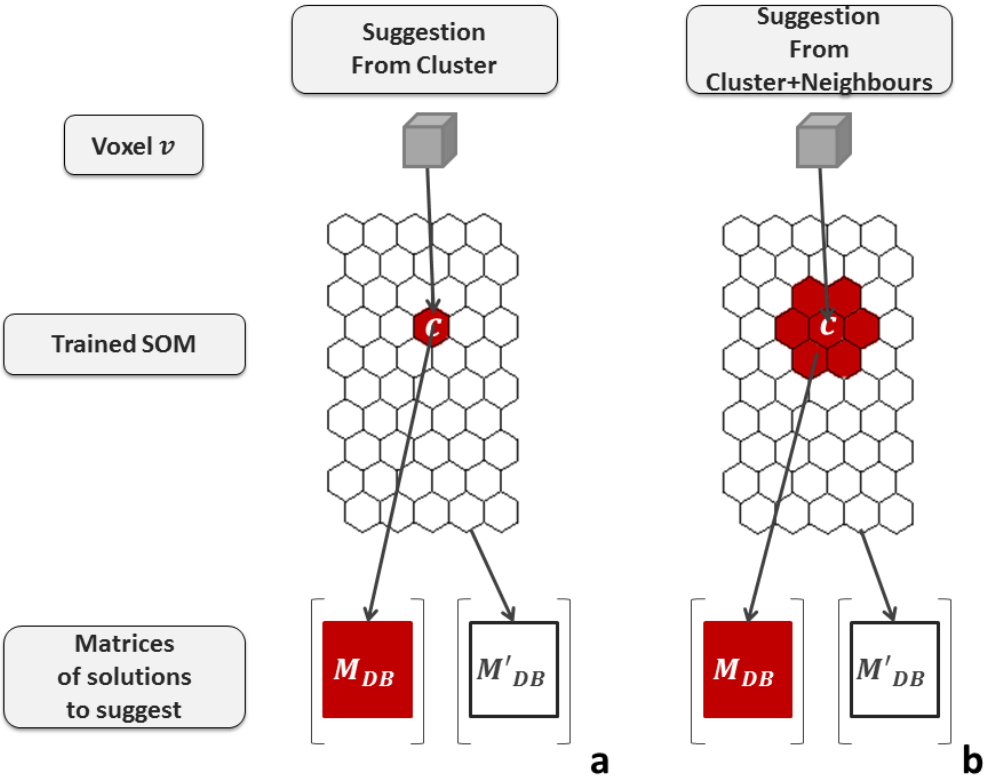

Figure 17. Process of collecting suggested solutions: each voxel v is associated to the corresponding BMU. A certain number (N_{DB}) of parameters vectors were then randomly chosen inside that cluster (a). If the number of element inside the cluster is less than N_{DB},

then two different actions may be followed. The first one was to decide not to suggest solutions. The second one was to use the elements inside the cluster and, then, look for the remaining solutions among the elements mapped to neighbouring neurons (b). In the rare event in which, also using neighbours, the N_{DB} was not reached, no solution was considered. The two procedures ended with the formation of a matrix (M_{DB}) containing the N_{DB} similar parameters vectors. Moreover, in both cases, an equal number of solutions placed in clusters different from c or also from its neighbourhood was chosen (forming M'_{DB}).

For each voxel v, the corresponding BMU (i.e. the corresponding cluster c) was found comparing its signals vector and the prototype vectors of the previous trained SOM. A certain number (N_{DB}) of parameters vectors were then randomly chosen inside that neuron/cluster. If the number of element inside the cluster is less than N_{DB}, then two different actions may be followed. The first one was to decide not to suggest solutions. The second one was to use the elements inside the cluster and, then, look for the remaining solutions among the elements mapped to neighbouring neurons. The number of neighbouring neurons taken into account was at most 6, since the lattice of the SOM was hexagonal, and the neighbourhood was generated as the first 6 neurons with prototype vectors closer to the prototype vector of c. In the rare event in which, also using neighbours, the N_{DB} was not reached, no solution was considered. The two procedures just described are referred in the following to as 'Suggestions From Cluster' (Figure 17 a) and 'Suggestions From Cluster+Neighbours' (Figure 17 b) and ended with the formation of a matrix (M_{DB}) containing the N_{DB} similar parameters vectors. To demonstrate that the N_{DB} chosen solutions (just inside the cluster or within the cluster and the neighbours) were closer to the correct solution of v than other random solutions, an equal number of solutions placed in clusters different from c or also from its neighbourhood was chosen (forming M'_{DB}). Two values of N_{DB} were tested: 50 and 100. The residual between the solution of v and the two sets of N_{DB} chosen solutions was computed as follows:

$$Parameters\ Residuals_h = \|\boldsymbol{p}_v - \boldsymbol{p}_h\|$$

where $\boldsymbol{p}_v$ is the correct solution of v, and $\boldsymbol{p}_h$ is the solution of the voxel h belonging to M_{DB} or M'_{DB}, with h that varied between 1 to N_{DB}. Since the ranges of the parameters were different from each other, a previous normalization of each parameter by its maximum value was done. The solution characterized by the minimum value of residual was considered and the percentage of times that this solution belonged M_{DB} rather than M'_{DB}. Furthermore, since this step involved a random process, 100 different simulations were performed and that percentage was given in terms of mean and standard deviation.

To investigate if the noise can corrupt the process of associating signal vectors to the correct cluster, three datasets with different levels of signal-to-noise ratio (SNR) were built. The noise was added to the *in silico* slice using the Rice distribution [67]. SPGR, SSFP0 and SSFP180 signals showed thus a total SNR equal to 50, or 100 or 150. The percentage of voxels that were assigned to the correct cluster was then computed.

After building the matrix M_{DB} and saving the information of which cluster a voxel is mapped to, in order to evaluate the effect of suggesting similar solutions in the mcDESPOT routine, the *in silico* noise free slice was processed. For each voxel v, at the first iteration, the suggested solutions (parameters vectors saved in M_{DB} and, if exists, in $M_{subject}$) were inserted into the population of the fit algorithm (both NotSimplified and Simplified fit). The $N_{subject}$ was 50. After that, the code ran normally. To compare the results, the not modified mcDESPOT was also run on the same data. The analysis of the results was performed on two levels (signals and parameters) and at each iteration (it). First of all, a comparison between the theoretical signals ($\boldsymbol{s}^{theoretical}$) generated from the solutions resulting from the optimization algorithm and the acquired signals ($\boldsymbol{s}^{acquired}$) was rendered through the computation of mean residuals:

$$Signals\ residual_v(it) = \left\| s_v^{theoretical}(it) - s_v^{acquired}(it) \right\|$$

$$Signals\ Mean\ Residual(it) = \frac{1}{N_{voxels}} \sum_{v=1}^{N_{voxels}} Signals\ Residual_v(it)$$

where N_{voxels} is the number of voxels with a nonzero signals of the image. For understanding how much the cumulative SOM+mcDESPOT residuals (i.e. the sum of residuals of all voxels) improved or deteriorated the mcDESPOT ones, the ratio between them was calculated:

$$Signals\ Cumulative\ Residual(it) = \sum_{v=1}^{N_{voxels}} Signals\ Residual_v(it)$$

$$Cumulative\ Residuals\ Ratio(it) = \frac{Signals\ Cumulative\ Residuals^{SOM+mcDESPOT}(it)}{Signals\ Cumulative\ Residuals^{mcDESPOT}(it)}$$

For a visual inspection, a map of the voxels that were characterized by lower signals residuals using mcDESPOT+SOM was plotted and the percentage of those voxels was computed. To investigate how much adding similar solutions to the fit population influenced the difference magnitude between the correct signals and the theoretical ones, the fraction of voxels with lower SOM+mcDESPOT signals residuals as a function of the amount of the difference between the SOM+mcDESPOT and mcDESPOT residuals was computed. In other words, defining

$$\delta(it) = \left| Signals\ Residuals^{SOM+mcDESPOT}(it) - Signals\ Residuals^{mcDESPOT}(it) \right|$$

The fraction of voxels with lower SOM+mcDESPOT signals residuals for each $\delta(it)$ was calculated as

$$f_v^{SOM+mcDESPOT}(\delta, it) = \frac{n^{SOM+mcDESPOT}(\delta, it)}{n^{SOM+mcDESPOT}(\delta, it) + n^{mcDESPOT}(\delta, it)}$$

where $n^{SOM+mcDESPOT}(\delta, it)$ is the number of voxels that had improved SOM+mcDESPOT residual:

$$Signals\ Residuals^{SOM+mcDESPOT}(it) \leq Signals\ Residuals^{mcDESPOT}(it) - \delta(it)$$

while $n^{mcDESPOT}(\delta, it)$ is the number of voxels with worse SOM+mcDESPOT residuals:

$$Signals\ Residuals^{SOM+mcDESPOT}(it) > Signals\ Residuals^{mcDESPOT}(it) + \delta(it)$$

Plotting the $f_v^{SOM+mcDESPOT}$ for each $\delta(it)$ allowed easily identifying how many voxels were improved (i.e. with lower residuals) after suggesting solutions and how much this improvement was.

Since the correct solution for each voxel was known, it was possible to perform the same analysis described above, but comparing the real parameters vector ($\boldsymbol{p}^{real}$) with the one resulting from the optimization algorithm ($\boldsymbol{p}$). Thus, similarly to the signals, the mean parameters residuals were computed:

$$Parameters\ Residual_v(it) = \|\boldsymbol{p}_v^{real}(it) - \boldsymbol{p}_v(it)\|$$

$$Parameters\ Mean\ Residual(it) = \frac{1}{N_{voxels}} \sum_{v=1}^{N_{voxels}} Parameters\ Residual_v(it)$$

The ratio between SOM+mcDESPOT cumulative parameters residuals and mcDEPOST ones was also calculated:

$$Parameters\ Cumulative\ Residual(it) = \sum_{v=1}^{N_{voxels}} Parameters\ Residual_v(it)$$

$$Parameters Cumulative Residuals Ratio(it) = \frac{Parameters\ Cumulative\ Residual^{SOM+mcDESPOT}(it)}{Parameters\ Cumulative\ Residuals^{mcDESPOT}(it)}$$

Maps of voxels with lower and higher SOM+mcDESPOT parameters residuals were plotted and the percentage of voxels with lower residuals due to the process of suggesting solutions was computed. Moreover, as before, the fraction of voxels with lower SOM+mcDESPOT parameters residuals as a function of $\delta(it)$ was plotted. To investigate the effect of SOM+mcDESPOT on each parameter, the residuals of $T_{1,M}$, $T_{2,M}$, $T_{1,F}$, $T_{2,F}$, τ_M, f_M and $\Delta\omega$ across all the iterations were plotted.

An evaluation of the precision and the reproducibility of the solutions generated by the SOM+mcDESPOT process was done running the process 100 times. The precision of each parameter was then computed as the mean of the 100 values divided by the standard deviation. The reproducibility or coefficient of variation was calculated as the reciprocal of the precision.

The last step of this validation phase was to evaluate the behaviour of the SOM+mcDESPOT in presence of acquired signals with low SNR. Thus, another *in silico* slice of brain with Rice distributed noise (SNR=50) was processed and the comparison between results from SOM+mcDESPOT and mcDESPOT was performed in the same way as for the noise free dataset.

2.4.2. *In vivo* experiments

The next phase was to validate the SOM+mcDESPOT model in a real scenario, i.e. using real images. A bigger *in silico* noise free database was built. 1676874 voxels were simulated mimicking the features of 3 normal brains and 3 brains affected by MS. For each voxel and given the 7 parameters combinations, the corresponding theoretical SPGR, SSFP0 and SSFP180 were generated as for the *in silico* slice. The signals vectors were collected, normalized by their mean and then clustered using the

Self Organizing Map. As previously, a hexagonal lattice map, a linear initialization and a batch training algorithm was chosen. In this case, the SOM size was large (number of cluster = 6480).

The images necessary for the validation were SPGR, SSFP0 and SSFP180 of 3 controls and 3 MS patients. Both were recruited at the University of California San Francisco with an informed consent and the study was performed with ethics approval from the host institute.

Table 5. Demographic data of the validation phase.

Demographic Data						
	C1	**C2**	**C3**	**P1**	**P2**	**P3**
Age (years)	45	36	54	37	58	53
Age at onset (years)	-	-	-	30	40	34
EDSS score	-	-	-	1	1.5	3.5

Imaging was performed on a 3 T GE scanner. Sagittally-oriented data were acquired with the sequence-specific parameters reported in Table 5. Following data acquisition, scalp and other nonbrain signals were removed from each image volume using the function BET of FSL (http://www.fmrib.ox.ac.uk/fsl/). The data from each individual were the linearly coregistered with FLIRT (FSL) to a reference volume (the first SPGR volume) to correct for subject motion throughout the exam. The Single-component T_1 and T_2 estimates were also calculated for each voxel using conventional DESPOT1 and DESPOT2 analysis [41].

The mcDESPOT+SOM and the normal mcDESPOT were run and the results were compared. As for the *in silico* slice, the evaluation of the results was conducted at two levels: one regarded the signals, and the other the solutions/parameters obtained. Concerning the signals results, the mean residuals between the acquired signals and the theoretical ones generated by the solutions of the optimization algorithm were computed and plotted for each iteration and for each fit. Moreover, the map of voxels and the percentage of them with lower residuals reached with the SOM+mcDESPOT were computed. Since the real parameters were not known, it was not possible to compute the parameters residuals. However, histograms comparing the distribution of the parameters values obtained from the two methods were compared.

2.5. Clinical application

The SOM+mcDESPOT was applied to 10 healthy controls and 55 MS patients. All participants were recruited in conformance with local ethics board requirements of the Univeristy of California San Francisco, CA, USA. Among the MS patients, 33 were diagnosed as affected by SPMS, while 22 showed a clinically isolated syndrome (CIS). In all patients, the MS extended disability status scale (EDSS) was evaluated. The patients and controls populations were indistinguishable by age according to a rank sum test at the 5% significance level. The demographic data are reported in Table 6.

Table 6. Demographic data of the application phase.

Demographic Data				
	Controls	**All patients**	**CIS**	**SPMS**
n	10	55	22	33
Median age (years)	40	52	50	55
Median Age at onset (years)	-	34	42	31
Median EDSS score	-	3	1.75	4

Images were acquired following the same procedure previously described in the section on *in vivo* experiments.

For the SOM+mcDESPOT process, the reference database from which the M_{DB} and c were extracted was the same one reported in the previous section and clustered with a large SOM ($n_{clusters} = 6480$). Only the process of suggesting solutions from the clusters (Figure 17 a) was used to generate M_{DB}.

To evaluate the distribution of the f_M values in the portion of tissue called normal appearing white matter (NAWM) that is defined as all white matter voxels minus the lesions, the conventional MRI data (T_1-weighted images) were used to segment the NAWM of each subject. This step was performed using FREESURFER (http://surfer.nmr.mgh.harvard.edu/). The segmented binary masks were then applied to the myelin-water fractions (f_M) maps, after a linear registration (FLIRT, FSL). Among all the parameters, only the f_M was analysed since it is the most important in determining the quantity of myelin in the voxel. The histograms of all f_M maps were then plotted, averaged across the different groups, normalized and compared to the

ones obtained with the traditional mcDESPOT. Moreover, the mean and median values of each f_M map were computed and compared among the groups using the two-samples T-test.

3. Results

The results derived from the validation and the application phases of SOM+mcDESPOT are reported in the following.

3.1. Validation

3.1.1. *In silico* experiments

Given the 4525 simulated combinations of the 7 parameters (mapped in the first column of Figure 18), the theoretical 24 volumes belonging to SPGR, bSSFP0, and bSSFP180 (8 volumes for each) were computed using the equations (1) and (2) (Figure 18).

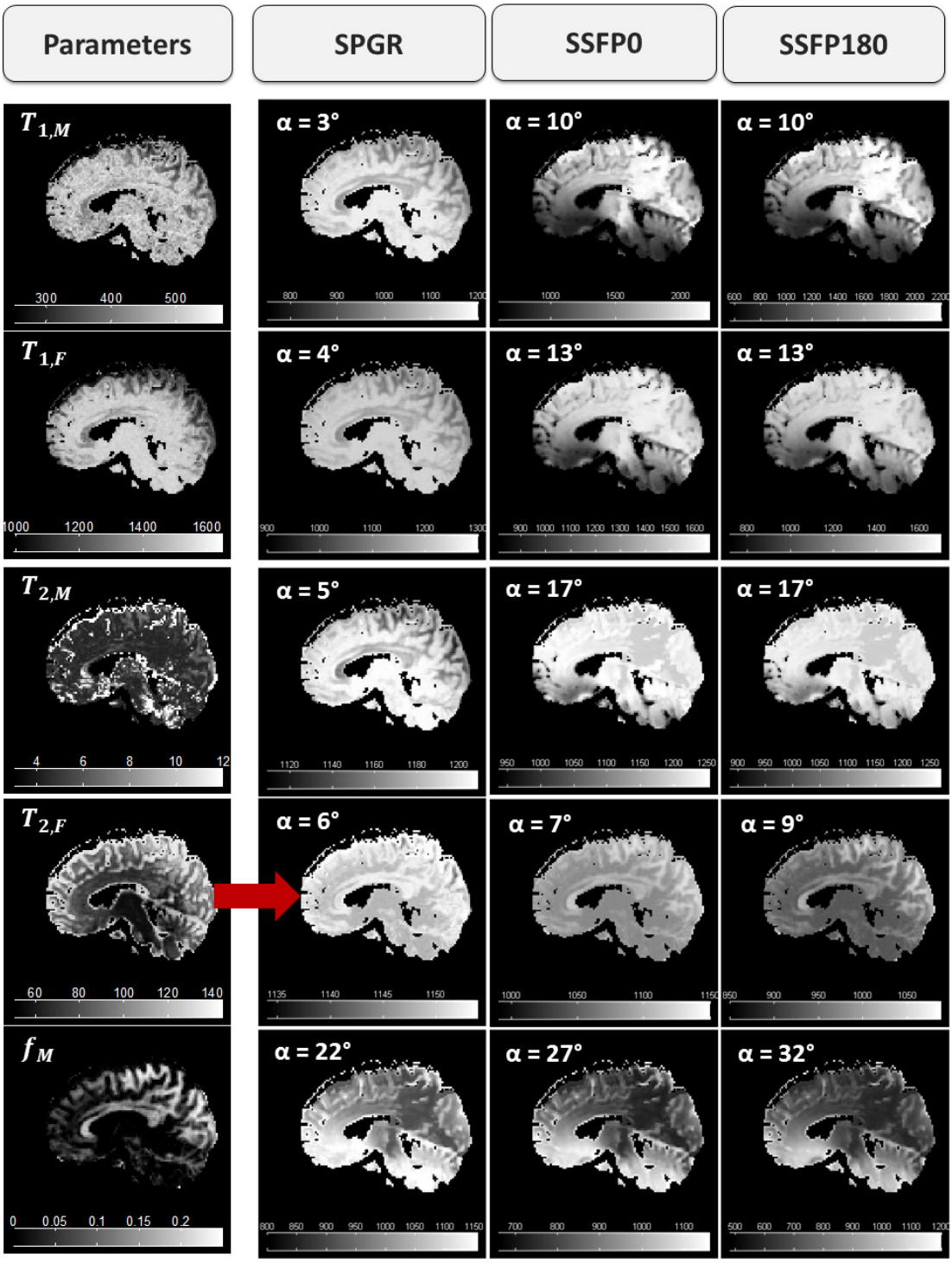
Parameters
SPGR
SSFP0
SSFP180
$T_{1,M}$
$T_{1,F}$
$T_{2,M}$
$T_{2,F}$
f_M
α = 3°
α = 10°
α = 10°
α = 4°
α = 13°
α = 13°
α = 5°
α = 17°
α = 17°
α = 6°
α = 7°
α = 9°
α = 22°
α = 27°
α = 32°

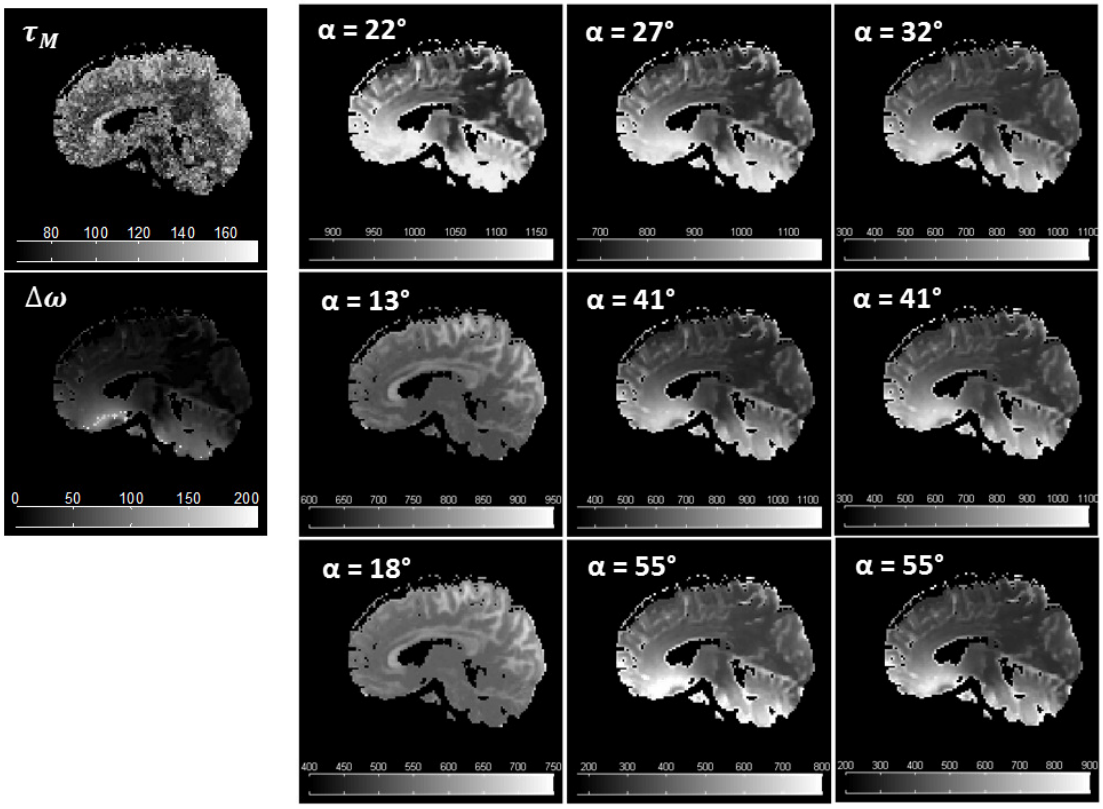

Figure 18. An *in silico* slice of human brain was simulated. Given 4525 voxels of different combinations of 7 parameters (first column), 8 volumes of SPGR (second column), SSFP0 (third column), and SSFP180 (forth column) signals were generated.

The volumes were normalized by their mean and queuing forming signals vectors of 24 or 16 (i.e. excluding the 8 volumes of SSFP0) elements. Those vectors were used as training set of a small, medium and large SOM. The number of neurons chosen for the architecture of the SOM was 52, 85 and 340, respectively. Considering each neuron as a cluster and labelled each voxel with its BMU, it was possible to obtain the clustering of the images based on their signals (Figure 19). Using both the NotSimplified and the Simplified SOM, a good segmentation of the major brain structures was achieved: the grey and white matter, the cerebellum, with its white and grey matter, and the brainstem were segmented using 24 volumes, while the corpus callosum was highlighted using just 16 volumes (Figure 19).

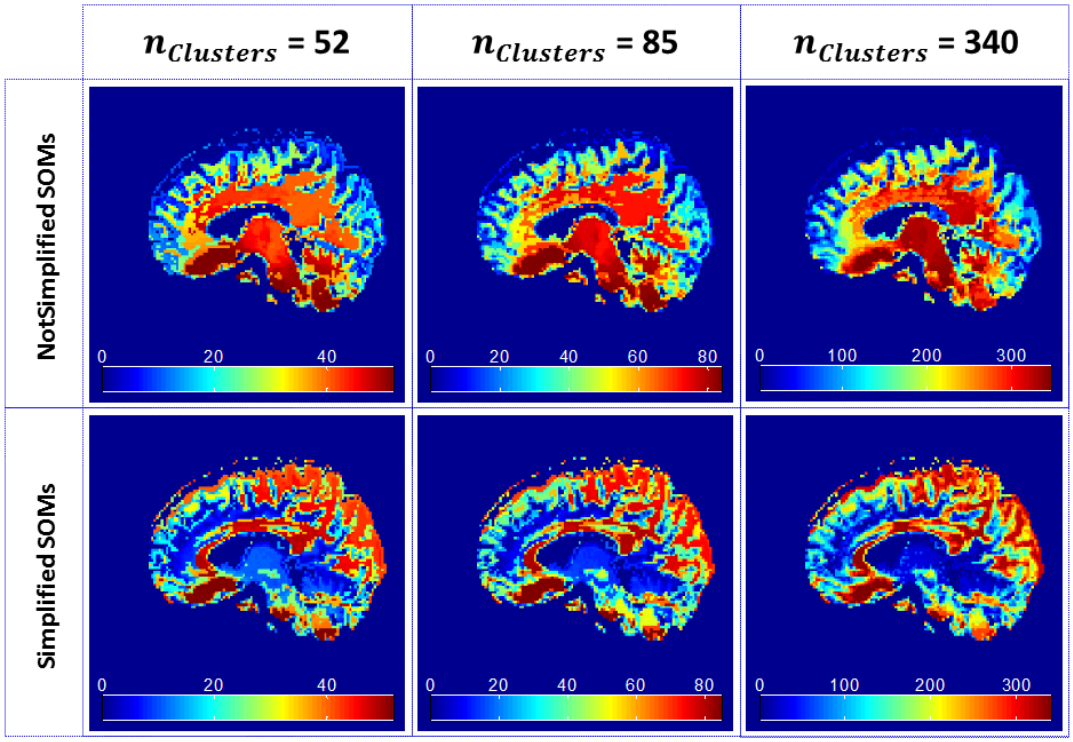

Figure 19. Small, medium and large SOM used to cluster the signals vectors of the *in silico* slice. A good segmentation of the major brain structures was achieved: the grey and white matter, the cerebellum, with its white and grey matter, and the brainstem were nicely segmented using 24 volumes (NotSimplified SOM, first row), while the corpus callosum was highlighted using just 16 volumes (Simplified SOM, second row).

Changing the number of neurons did not vary the topographic distribution of them: increasing that number, in fact, allowed discriminating better among different signals, but the main distinctions were still preserved. To evaluate the quality of SOM clustering in the signals space, the intra- and inter-cluster distances were computed. In every case, the distance between the prototype vector of the cluster c and the other prototype vectors was at least 8 times bigger than the intra-cluster distance of c (data not shown). This difference was statistically significant

($p < 0.01$). The SOM size that minimized and maximized most the intra- and inter-cluster distances, respectively, was the large one.

The next step sought a linear relationship between the two spaces, assuming that the shape of signals space could be detected in the shape of the parameters space in some way. To investigate that hypothesis, the inter- and intra-cluster distances were computed, but, this time, in terms of parameters vectors. As expected, the results showed close distances (data not shown), meaning that the shapes were different and the clustering was optimized for the signals space, but not in the parameters space.

Despite that, another test was performed to understand if clusters designed by SOM could be informative of the similarity among voxels in terms of parameters and not only in terms of signals. For each voxel v belonging to cluster c, N_{DB} solutions randomly chosen from the same cluster (or at most also from the neighbouring clusters) were compared to the parameters vector of v. Since testing this hypothesis involved a random process, 100 different simulations were performed. The results are reported in Table 7.

Table 7. Mean percentage and standard deviation of similar voxels belonging to M_{DB}.

		Suggestions From Cluster		Suggestions From Cluster+Neighbours	
	N_{DB}	50	100	50	100
NotSimplified SOM size	Small	64.59 ± 1.00	64.7 ± 2.09	61.44 ± 0.97	61.44 ±1.00
	Medium	66.90 ± 0.70	68.25 ± 1.51	61.28 ± 0.83	62.36 ± 0.75
	Large	74.21 ± 2.45	/	63.92 ± 0.60	63.96 ± 0.97
Simplified SOM size	Small	60.51 ± 1.09	63.64 ± 1.20	61.87 ± 0.58	63.07 ± 0.68
	Medium	62.47 ± 0.59	63.65 ± 1.35	62.70 ± 0.97	63.02 ± 0.98
	Large	63.24 ± 2.73	/	65.64 ± 0.67	65.31 ± 0.51

On the whole, the process allowed suggesting solutions more similar to the one to be computed in more than 60.51% of the voxels. This implied that the information similar to the one that we wanted is at least 60.51% of the times contained in the same cluster (or at most in the neighbouring clusters). Moreover, the similarity was given by very small residuals, i.e. with values around 10^{-3}. The best result was obtained using the large NotSimplified SOM (74.21% ± 2.45%). However, in this case and in the Simplified one, using 100 suggested solutions, it was not possible to derive the amount of voxels that had the most similar parameters vector in the cluster because the number of neurons with at least 100 voxels mapped inside was zero. The general trend showed that increasing the size of the SOM led to an increase of this percentage. Moreover, using 16 volumes (Simplified SOM) without including the

neighbours information made the results worse, while, considering the neighbours clusters elements slightly improved the percentage of voxels. Analysing the standard deviations for each test showed that the randomness used for choosing the solutions did not influence the results.

In the process of collecting N_{DB} similar solutions, the crucial part is represented by assigning a voxel to its BMU (i.e. its cluster). To evaluate how much this process is influenced by the noise of the images, a Rice distribution noise was added to the training set leading to images characterized by SNR equal to 200, 100 and 50 (for instance, Figure 20).

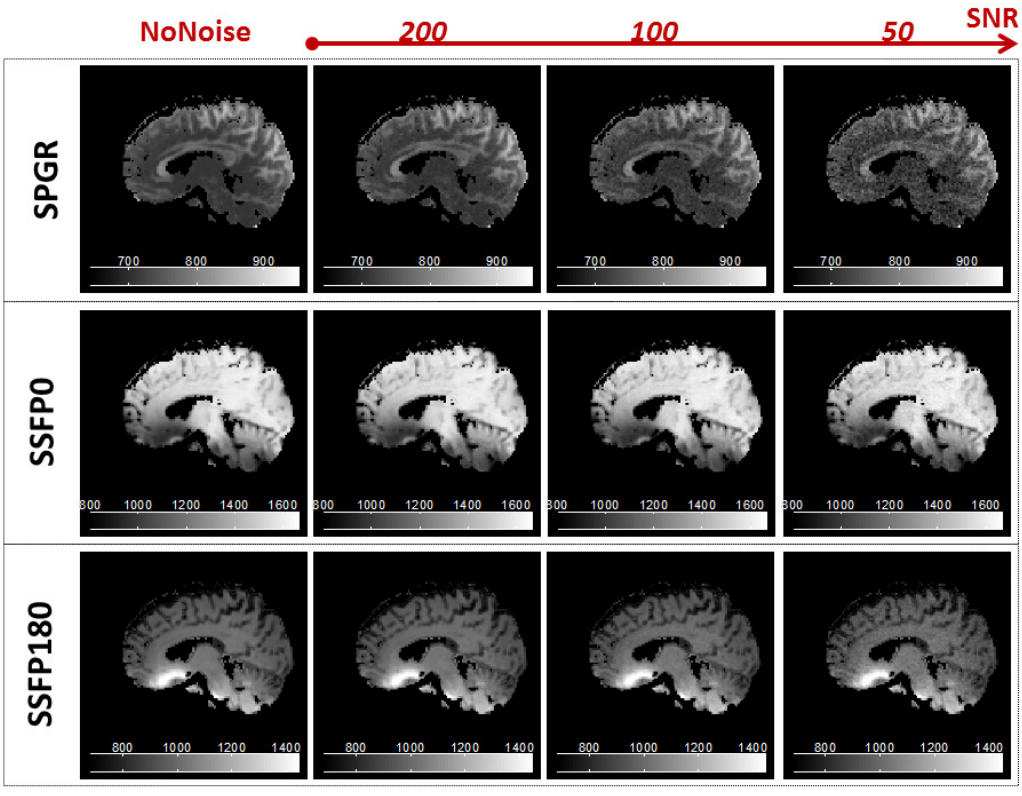

Figure 20. Comparison of effects on the first volume of SPGR, SSFP0 and SSFP180 after adding a Rice distribution noise.

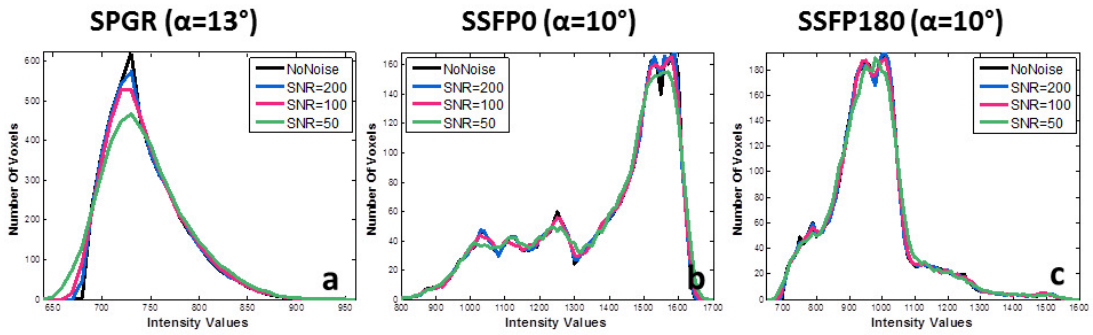

Figure 21. Comparison of effects on the histograms of the first volume of SPGR, SSFP0 and SSFP180 after adding a Rice distribution noise.

Even if the different level of noise could significantly change the signals (for example, Figure 21), the correct association between a voxel and its cluster was not affected, especially using 24 volumes SOM (Table 8). In general, increasing the SOM size led to a decrease of percentage of voxels mapped to the correct c. Since larger SOM implies more similar prototype vectors, it was easier to associate corrupted signals to another cluster. Obviously, this percentage decreased also when the SNR reduced. However, this decrease was not dramatic considering the small and medium NotSimplified SOMs: in those cases, the percentage of voxels mapped to the correct cluster was still high (85.28% and 81.04%, respectively). Using 16 volumes made the results worse up to just 32.46% with SNR equal to 50 and a large SOM.

Table 8. Percentage of voxels corrupted by noise and mapped to the correct cluster.

% of voxels mapped to the correct BMU						
	NotSimplified SOMs			Simplified SOMs		
SNR	**200**	**100**	**50**	**200**	**100**	**50**
Small SOM	96.22	92.27	85.28	91.23	82.63	66.36
Medium SOM	94.50	90.10	81.04	87.85	75.98	57.68
Large SOM	91.60	82.85	66.28	75.23	54.59	32.46

Looking for a compromise among all results described so far, a large SOM was chosen and the relative clusters information was used to run SOM+mcDESPOT. Moreover, mcDESPOT was run on the same data. The results were compared in terms of signals residuals, since it is the metric used in mcDESPOT to evaluate the goodness of a solution, and in terms of parameters residuals, since, in this case, the real solutions were known.

The mean signals residuals trend over all iterations is reported in Figure 22 (a, b).

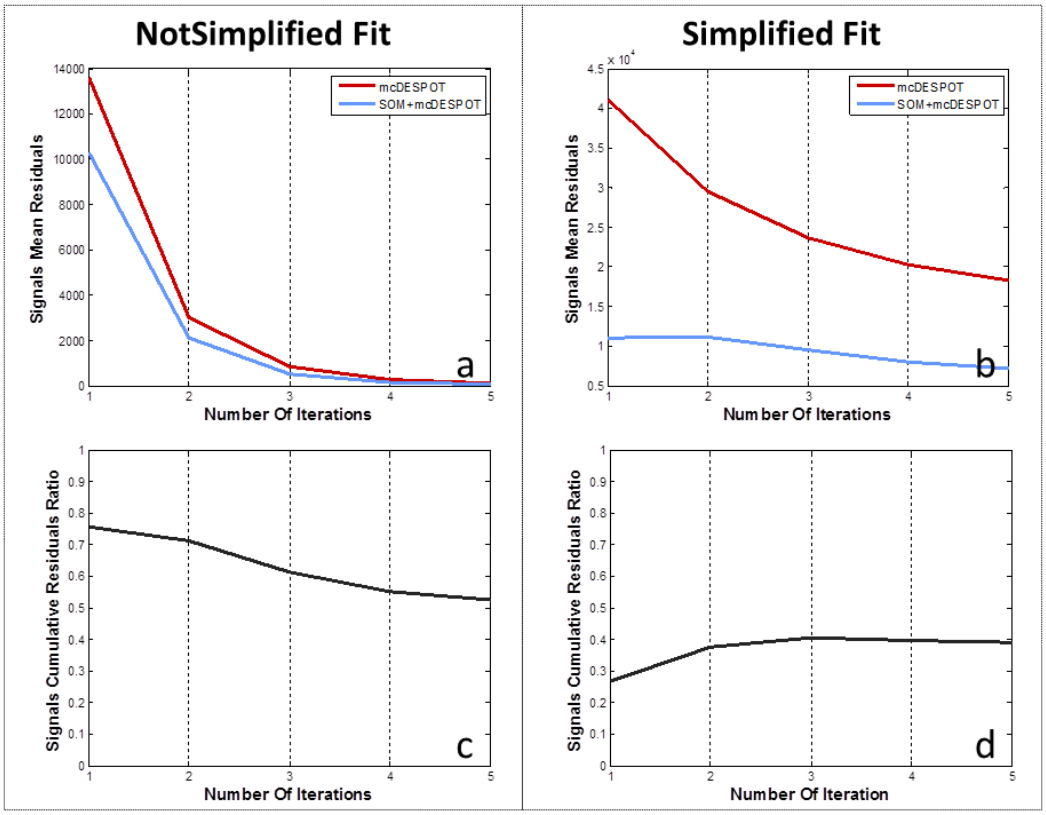

Figure 22. Noise free data: signals mean residuals derived from NotSimplified (a) and Simplified (b) fit, and cumulative residuals ratio of NotSimplified (c) and Simplified (d) fit.

In both fits, suggesting parameters vectors at the first iteration caused an improvement of the total residual. This improvement was more accentuated and maintained until the end of the process in the Simplified fit (Figure 22 b). Plotting the ratio between the cumulative signals residuals obtained with SOM+mcDESPOT and the ones obtained with mcDESPOT, the improvement is clearer (Figure 22 c and d). For the NotSimplified fit, an initial gain of 20% in the residuals evolved towards an almost 50% at the end of the process. In the Simplified fit, instead, the results were even more outstanding: at the beginning, the SOM+mcDESPOT residuals represented just the 30% of the mcDESPOT residuals value; and, at the end, this percentage slightly increased reaching the 40%.

Mapping the voxels that were characterized by a lower SOM+mcDESPOT signals residuals showed that there was not a specific region in which the improvement was registered, but it was a diffused phenomenon for the NotSimplified fit (Figure 23, first row); while, with 16 volumes, a light prevalence in the white matter, brainstem and cerebellum was noticed (Figure 23, second row).

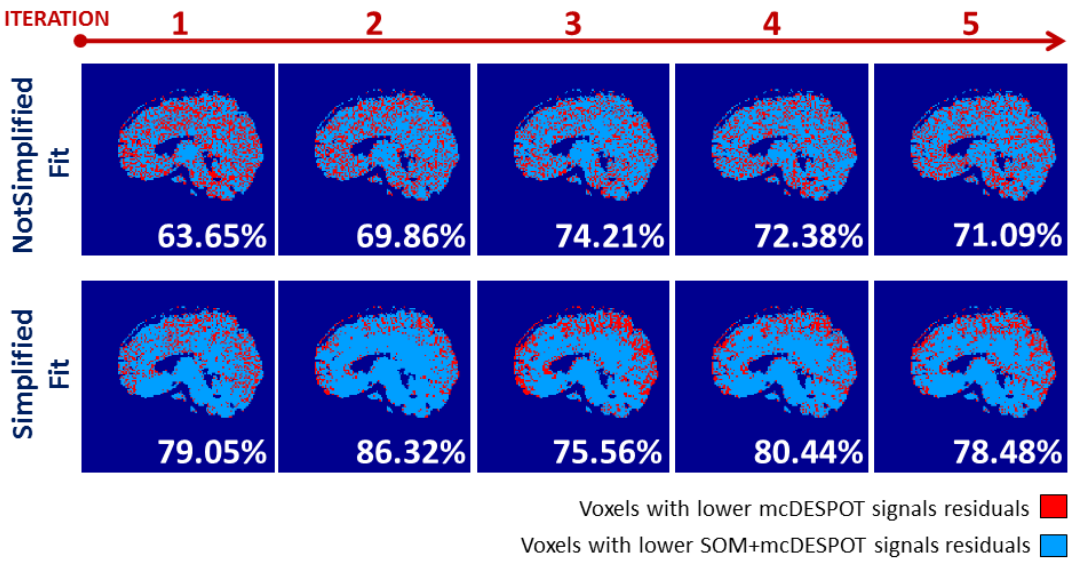

Figure 23. Noise free data: maps of voxels characterized by lower mcDESPOT signals residuals (red) and SOM+mcDESPOT signals residuals (blue) across all iterations and in both fits.

The percentage of voxels involved in this improvement ranged from 63.65% to 74.21% in the NotSimplified fit, and from 75.56% to 86.32% in the Simplified one. This means that at least 63% of the voxels benefited from SOM+mcDESPOT approach, reducing remarkably their signals residuals.

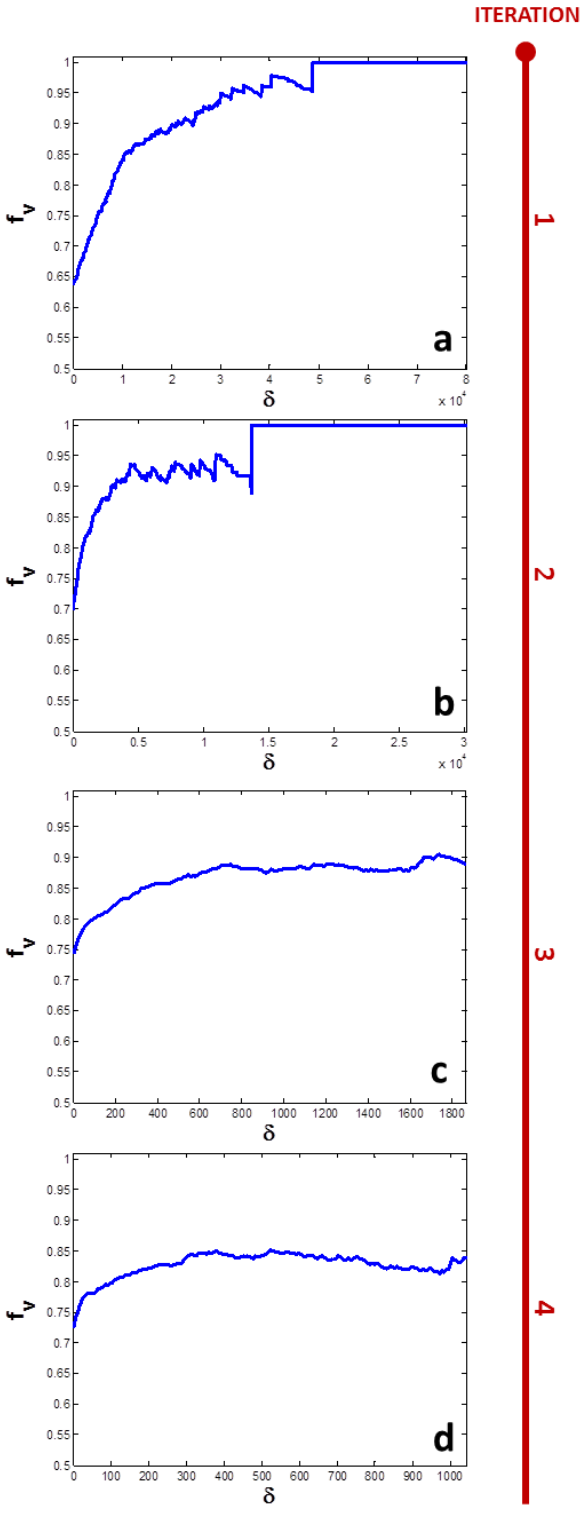
ITERATION
1
2
3
4
a
b
c
d
f_v
δ
x 10^4

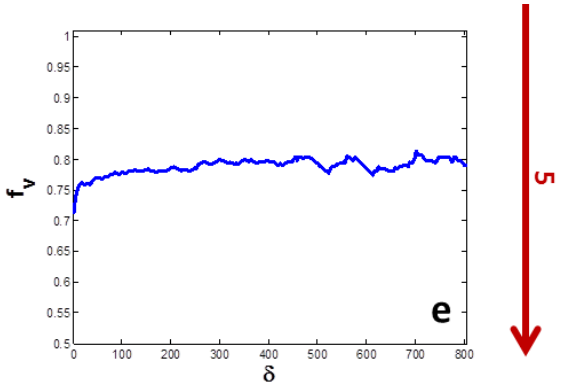

Figure 24. Noise free data: plots of $f_v^{SOM+mcDESPOT}$ in function of δ at first (a), second (b), third (c), forth (d) and fifth (e) iteration. This plot is referred to only the NotSimplified fit. In this case, δ is the difference among signals residuals.

To confirm this result, another analysis was performed (Figure 24). For each voxel, the magnitude of the difference between the SOM+mcDESPOT and mcDESPOT signals residuals was computed and reported on x-axis. Then, the corresponding fraction of voxels that showed a residuals difference greater than each value on x-axis and that had a lower SOM+mcDESPOT residuals was plotted on y-axis. Considering the Not Simplified fit, using the information from the trained SOM allowed us to obtain lower signals residuals in more than 60% of the voxels (Figure 24 a). This percentage increases to 100% as the difference between the SOM+mcDESPOT and mcDESPOT residuals increases, meaning that in the cases where the suggestions are very different, the SOM+mcDESPOT always gives the better suggestions. The same reasoning can be followed for the other iterations (Figure 24 b, c, and d): most voxels (at least 70% of them) showed much lower SOM+mcDESPOT residuals. In the Simplified fit, this situation was more accentuated: in fact, for each iteration, almost all the voxels (more than 95%) showed lower SOM+mcDESPOT residuals at δ (data not shown).

To investigate the results also in terms of parameters, the previous analysis was performed evaluating the difference between the solutions obtained by

SOM+mcDESPOT and the ones by mcDESPOT. The main observations derived from the signals residuals could be also applied to the parameters ones. Plotting the mean parameters residuals at each iteration showed how the accuracy was affected using SOM+mcDESPOT (Figure 25 a and b).

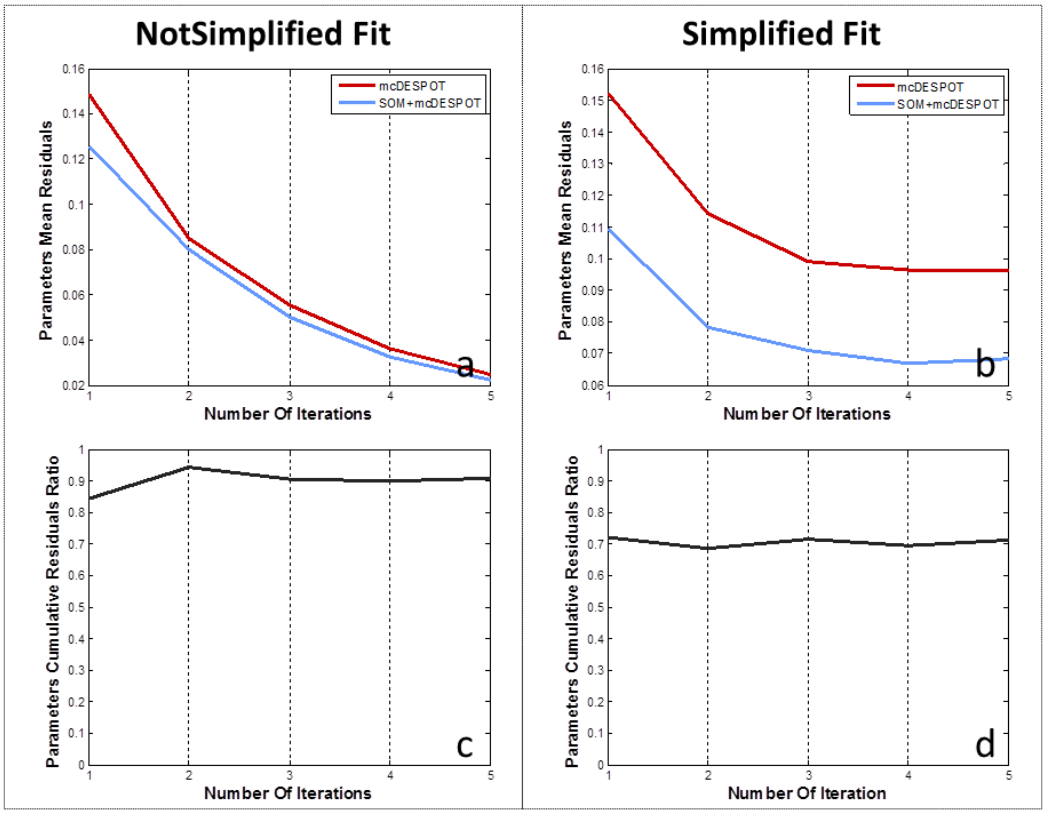

Figure 25. Noise free data: parameters mean residuals derived from NotSimplified (a) and Simplified (b) fit, and cumulative residuals ratio of NotSimplified (c) and Simplified (d) fit.

As before, when the solutions derived by SOM analysis were introduced in the optimization algorithm, a big difference between residuals was noticed, especially in the Simplified fit. This improvement was then reduced in the NotSimplified fit up to almost reach the convergence, and maintained in the Simplified one. The improvement amount was around 10-15% using 24 volumes and around 30% using

16 volumes (Figure 25 c and d). In other words, the mean accuracy was improved of 10-15% and 30% within the NotSimplified and Simplified fit, respectively.

The percentage of voxels that showed lower SOM+mcDESPOT parameters residuals ranged from 53.79% to 57.35% using 24 volumes to generate the solutions, and from 54.08% to 66.23% using 16 signals volumes (Figure 26). Their distribution did not reveal any particular region of preference (Figure 26).

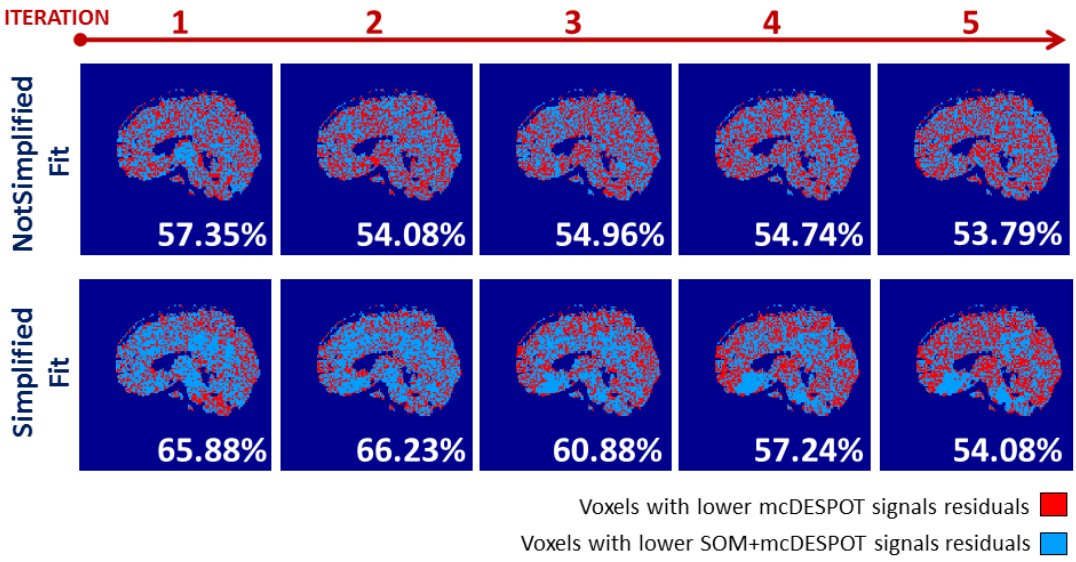

Figure 26. Noise free data: maps of voxels characterized by lower mcDESPOT parameters residuals (red) and SOM+mcDESPOT parameters residuals (blue) across all iterations and in both fits.

Figure 27 highlights the contribution of SOM+mcDESPOT in determining each parameter total residuals.

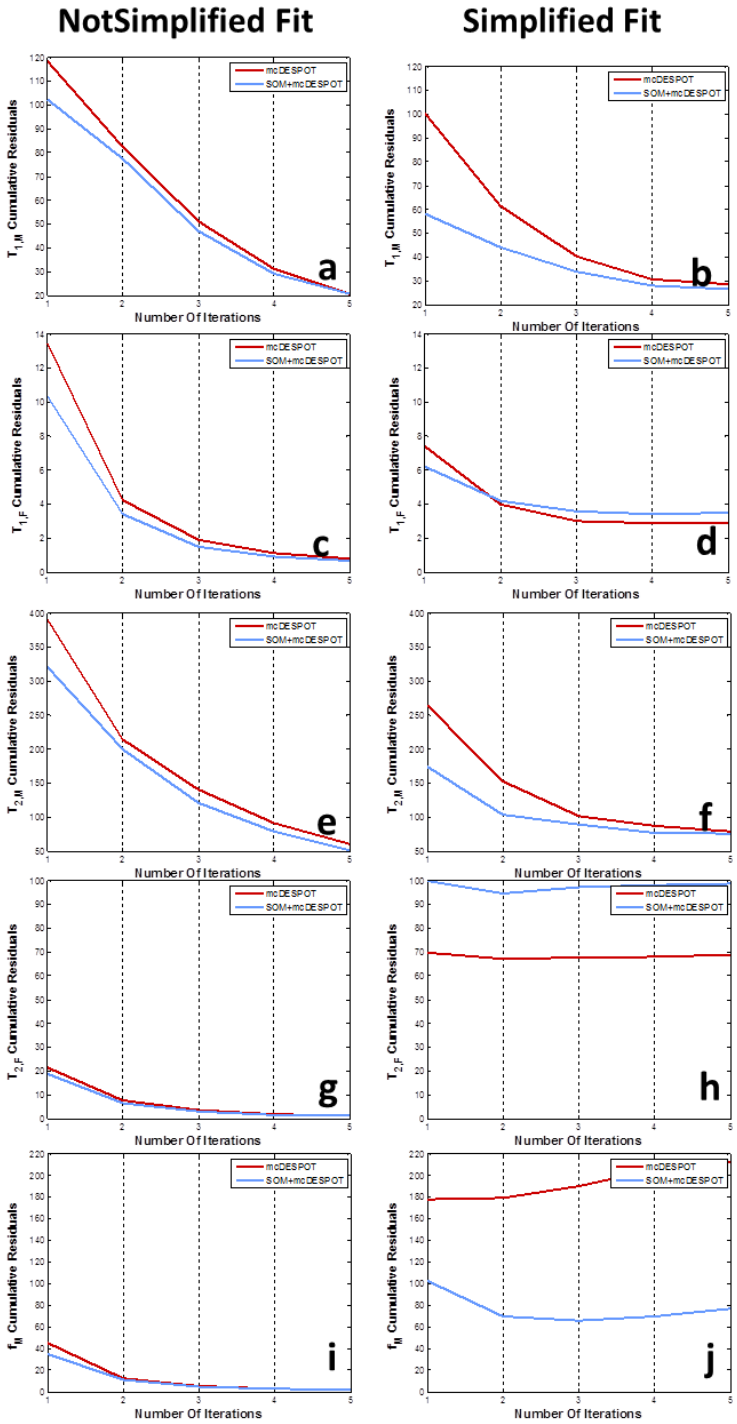
NotSimplified Fit
Simplified Fit
mcDESPOT
SOM+mcDESPOT
Number Of Iterations
$T_{1,M}$ Cumulative Residuals
$T_{1,F}$ Cumulative Residuals
$T_{2,M}$ Cumulative Residuals
$T_{2,F}$ Cumulative Residuals
f_M Cumulative Residuals
a
b
c
d
e
f
g
h
i
j

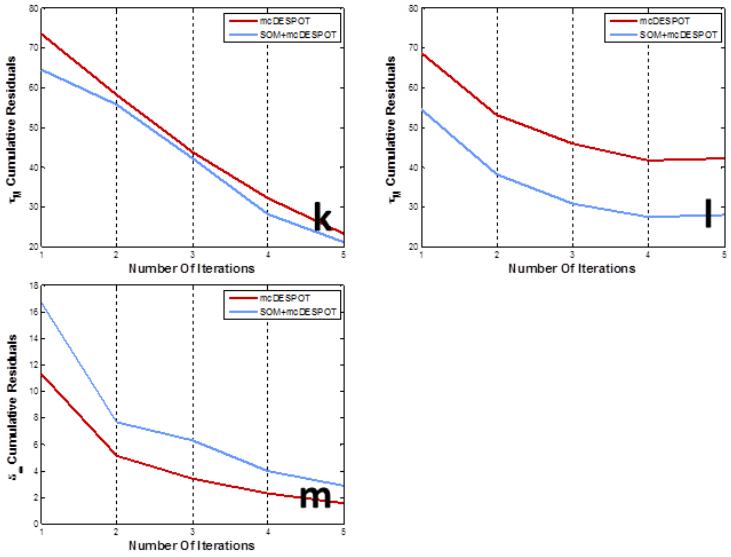

Figure 27. Noise free data: $T_{1,M}$ (a,b), $T_{1,F}$ (c,d), $T_{2,M}$ (e,f), $T_{2,F}$ (g,h), f_M (i,j), τ_M (k,l) and $\Delta\omega$ (m) cumulative residuals obtained with both fit.

At the first iteration, the improvement due to the suggested feasible solutions was always present. At the end of the iterations of the NotSimplified fit, most of parameters obtained with SOM+mcDESPOT converged at the same values of mcDESPOT (Figure 27 a, c, g and i). A reduced cumulative residual, instead, was noticed for the parameter $T_{2,M}$ and τ_M (Figure 27 k and e). For the Simplified fit, a more complex situation was registered: almost converging curves were obtained for $T_{1,M}$, $T_{2,M}$ and $T_{1,F}$ (Figure 27 b, d and f); lower SOM+mcDESPOT residuals were noticed for f_M and τ_M (Figure 27 j and l); while $T_{2,F}$ had a higher SOM+mcDESPOT curve (Figure 27 h).

To investigate how many voxels were characterized by a SOM+mcDESPOT solution different from a mcDESPOT solution and how much this difference was, the fraction of voxels with lower SOM+mcDESPOT parameters residuals as a function of δ was plotted for each iteration (Figure 28).

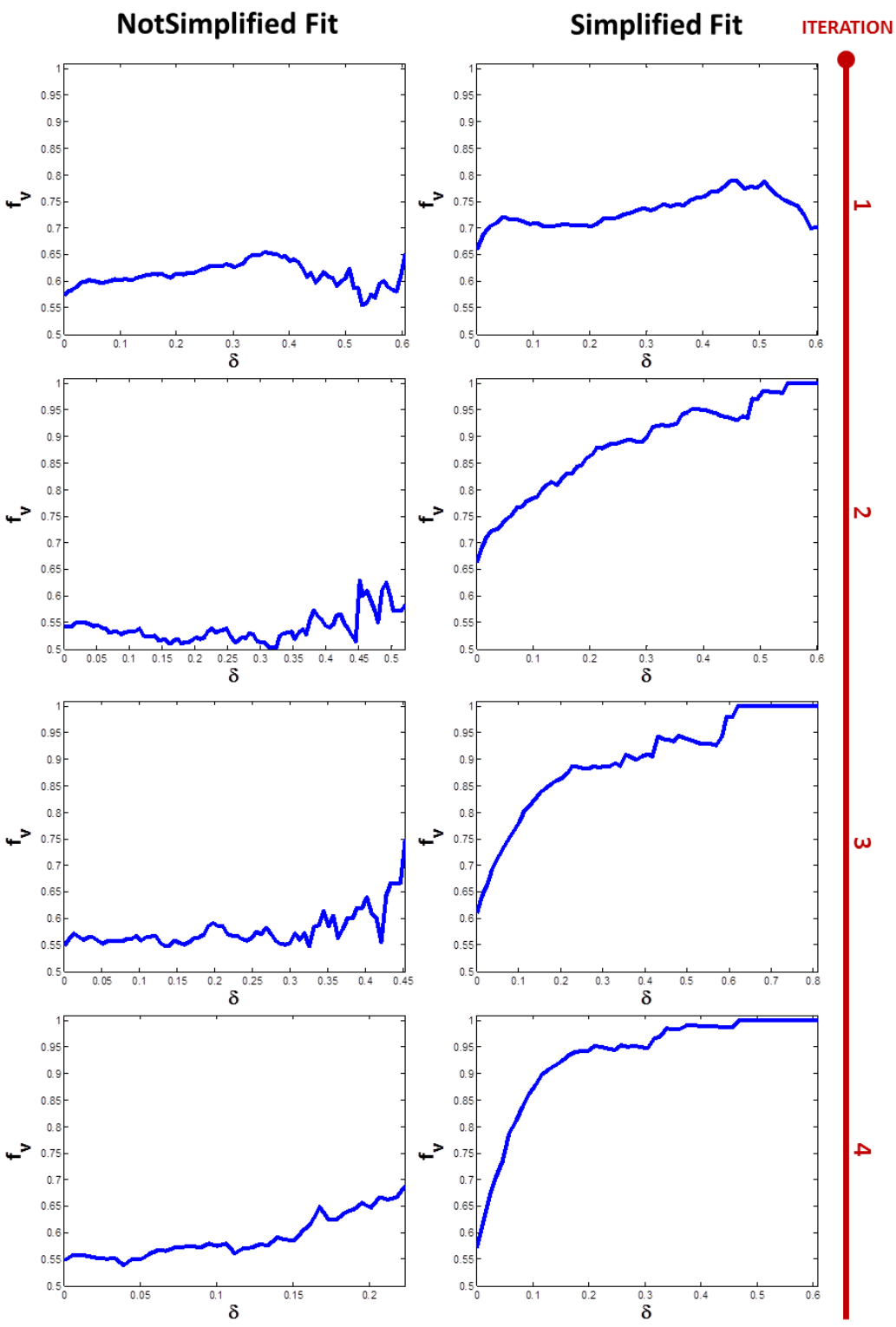
NotSimplified Fit
Simplified Fit
ITERATION
1
2
3
4
f_v
δ

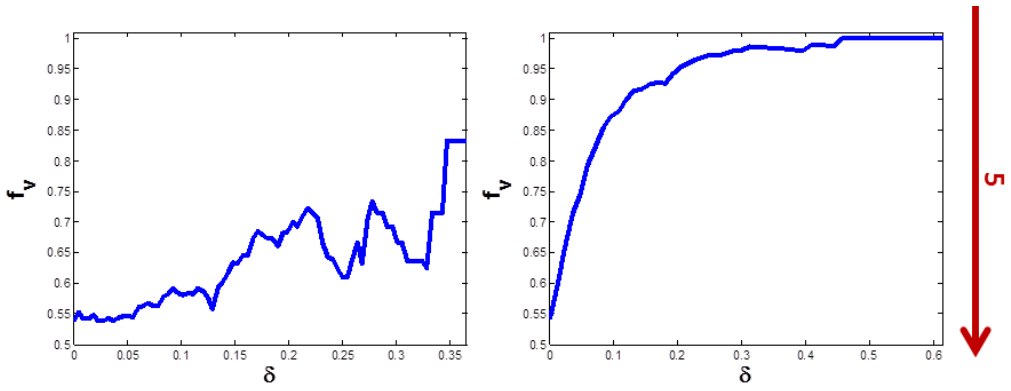

Figure 28. Noise of free data: plots of $f_v^{SOM+mcDESPOT}$ in function of δ across all iterations and referred to NotSimplified fit (first column) and Simplified one (second column). In this case, δ is the difference among parameters residuals.

Computing the NotSimplified fit, the SOM+mcDESPOT was responsible of remarked different and accurate solution in a rough mean of 60% of voxels (Figure 28, first column). Using the Simplified fit, this percentage increased reaching 100% in almost all iterations as the difference between solutions obtained by SOM+mcDESPOT and mcDESPOT increased (Figure 28, second column). This indicates that also the parameters, as the signals before, benefited from the process of suggesting solutions.

Since the analysis so far was done on noise free data, to evaluate the behaviour of SOM+mcDESPOT and mcDESPOT on a worse scenario, images characterized by a SNR equal to 50 were processed. Even in this case, the mean signals residuals were lower using SOM+mcDESPOT (Figure 29 a and b).

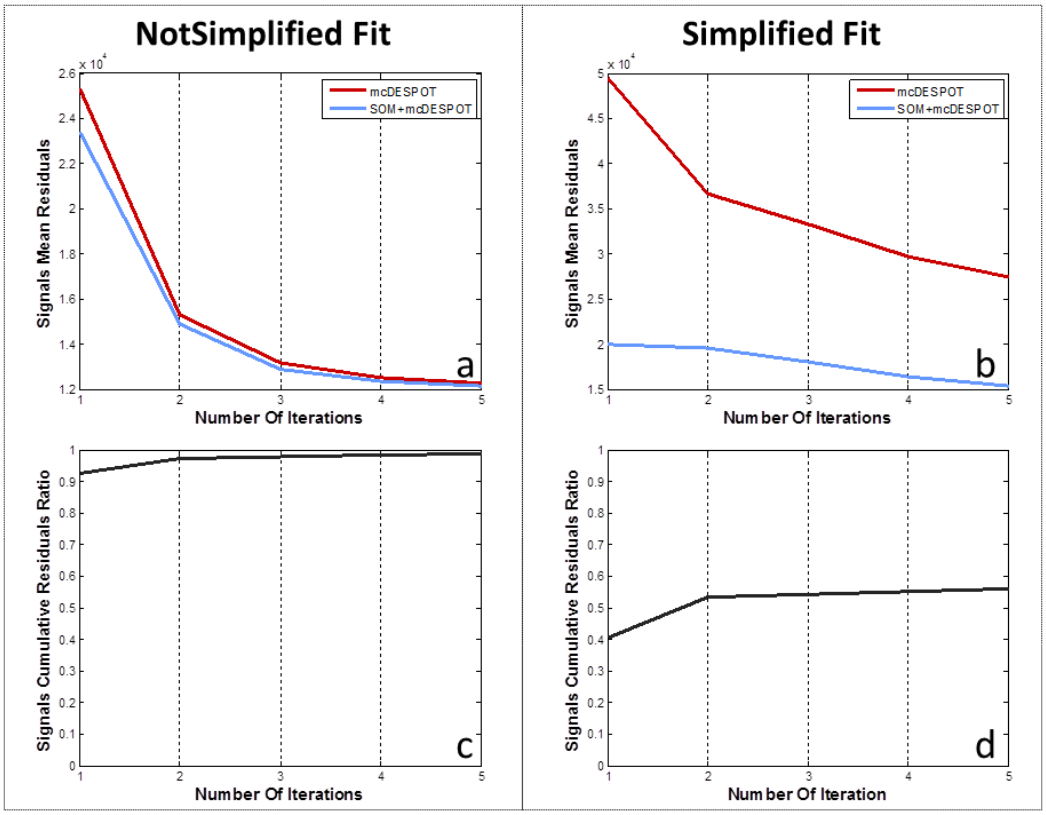

Figure 29. Data with SNR=50: signals mean residuals derived from NotSimplified (a) and Simplified (b) fit, and cumulative residuals ratio of NotSimplified (c) and Simplified (d) fit.

In particular, in the NotSimplified fit, the difference between the two methods was less than 10% (Figure 29 c); in the Simplified fit, instead, the SOM+mcDESPOT residuals was, roughly, 50-60% lower than mcDESPOT ones (Figure 29 d). The total percentage of voxels with lower SOM+mcDESPOT signals is reported in Table 9. There was a worsening compared to the noise free data (Figure 23), but still the 50-60% (NotSimplified fit) and 70% (Simplified fit) of voxels showed lower residuals with the new approach.

Table 9. Percentage of voxels corrupted by noise and with lower SOM+mcDESPOT signals residuals.

% voxels with lower SOM+mcDESPOT signals residuals					
Iteration	**1**	**2**	**3**	**4**	**5**
NotSimplified Fit	56.27	55.38	59.82	59.29	59.29
Simplified Fit	71.45	70.14	69.02	69.44	69.04

The distribution of these voxels and the fraction of voxels with lower SOM+mcDESPOT as a function of δ were close to ones obtained in the noise free data (data not shown).

As expected, analysing the results from the point of view of the parameters, a general worsening in both fits was noticed (Figure 30): in this case, in fact, the accuracy of SOM+mcDESPOT improved of 10-15% in the Simplified algorithm (Figure 30 d), while it was almost equal or at most less than 5% worse in the NotSimplified one (Figure 30 d).

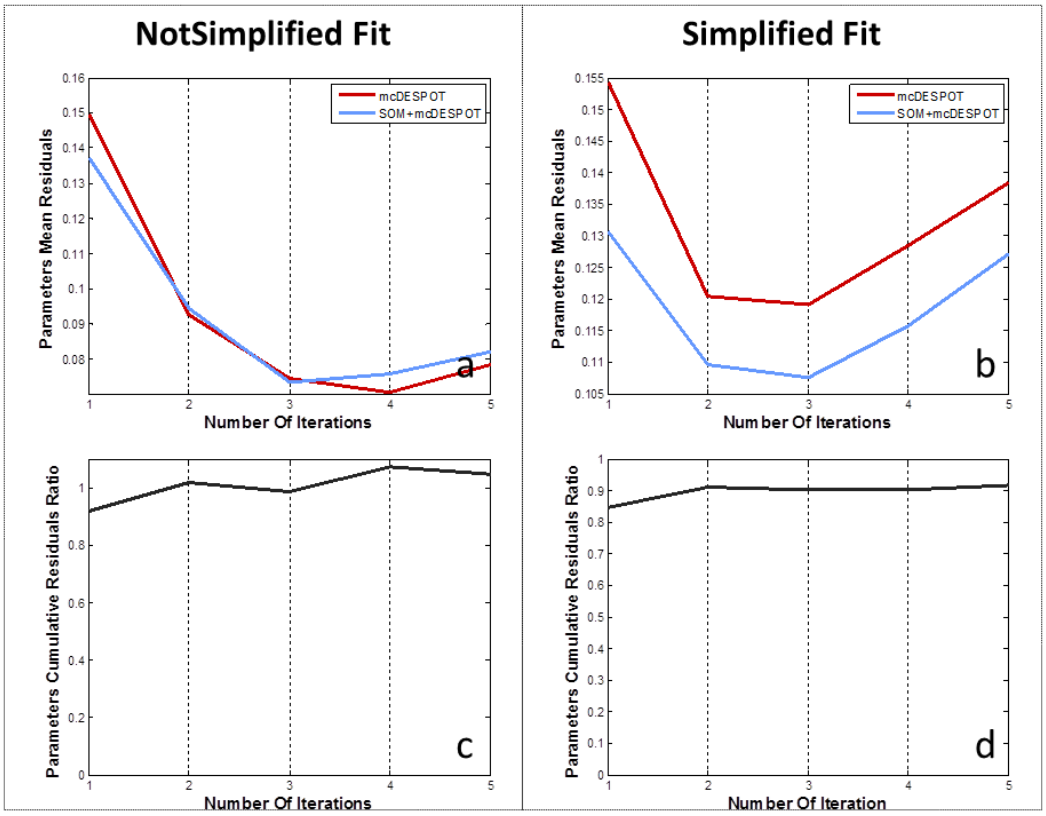

Figure 30. Data with SNR=50: parameters mean residuals derived from NotSimplified (a) and Simplified (b) fit, and cumulative residuals ratio of NotSimplified (c) and Simplified (d) fit.

However, major emphasis should be given to the first iteration, since it was the point in which the solutions were suggested: considering just that iteration, the improvement of all residuals (both signals and parameters ones) was clear (Figure 29 and 30). A worsening was also noticed in the total percentage of voxels with lower SOM+mcDESPOT parameters residuals (Table 10) compared to noise free data: nevertheless around 46.45 to 59.65% of voxels showed improvements in their residuals after suggesting solutions.

Table 10. Percentage of voxels corrupted by noise and with lower SOM+mcDESPOT parameters residuals.

% voxels with lower SOM+mcDESPOT parameters residuals					
Iteration	**1**	**2**	**3**	**4**	**5**
NotSimplified Fit	53.19	49.55	49.75	47.03	46.45
Simplified Fit	59.65	50.23	48.13	48.18	46.19

However, the SOM+mcDESPOT method showed a leading role on determining different solutions with higher accuracy: the voxels that were characterized by higher accuracy values were the one with the solutions generated by the modified method, showing behaviour close to (Figure 24 and 28).

100 different simulations of SOM+mcDESPOT on noise free and with noise data: the precision and the reproducibility were comparable to the ones obtained with mcDESPOT (data not shown), meaning that incorporating a priori knowledge did not influence the main processes implemented in mcDESPOT.

3.1.2. *In vivo* experiments

After demonstrating that suggesting solutions improved the accuracy in a simulated scenario, SOM+mcDESPOT and mcDESPOT were run in 6 real cases (3 controls and 3 MS patients). Before running the two methods, a pre-processing, consisting of

brain extraction and coregistration, was performed. Then, for each subjects, the association between each voxel and its c was found and M_{DB} was built.

The results in terms of mean signals residuals were reported in Figure 31.

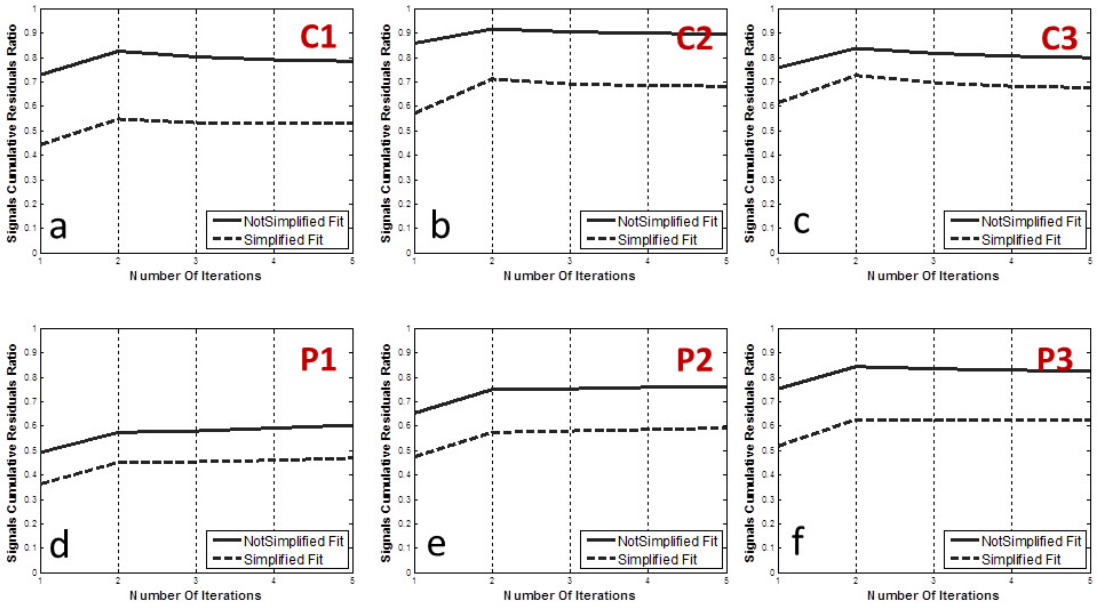

Figure 31. Signals cumulative residuals ratio in 3 healthy subjects (a, b and c) and 3 patients (d, e and f).

In all cases, the SOM+mcDESPOT obtained lower residuals, reaching a gain that ranged from 10 to 50% for the NotSimplified fit, and from 30 to 60% for the Simplified one. A larger overall improvement in the patients group was noticed (Figure 31 d, e and f).

To compare the final solutions, histograms of each parameter were plotted (Figure 32 and 33). In general, suggesting solutions in the optimization algorithm led to lower the major peak in the histograms, because the trend in proximity of the boundaries of each parameters was smoother than mcDESPOT. A cut-off at each boundary was, in fact, observed in the histograms derived by mcDESPOT, while it was not present in

the SOM+mcDESPOT. This behaviour was observed without distinction in both patients (for instance, Figure 33) and healthy subjects (for instance, Figure 32).

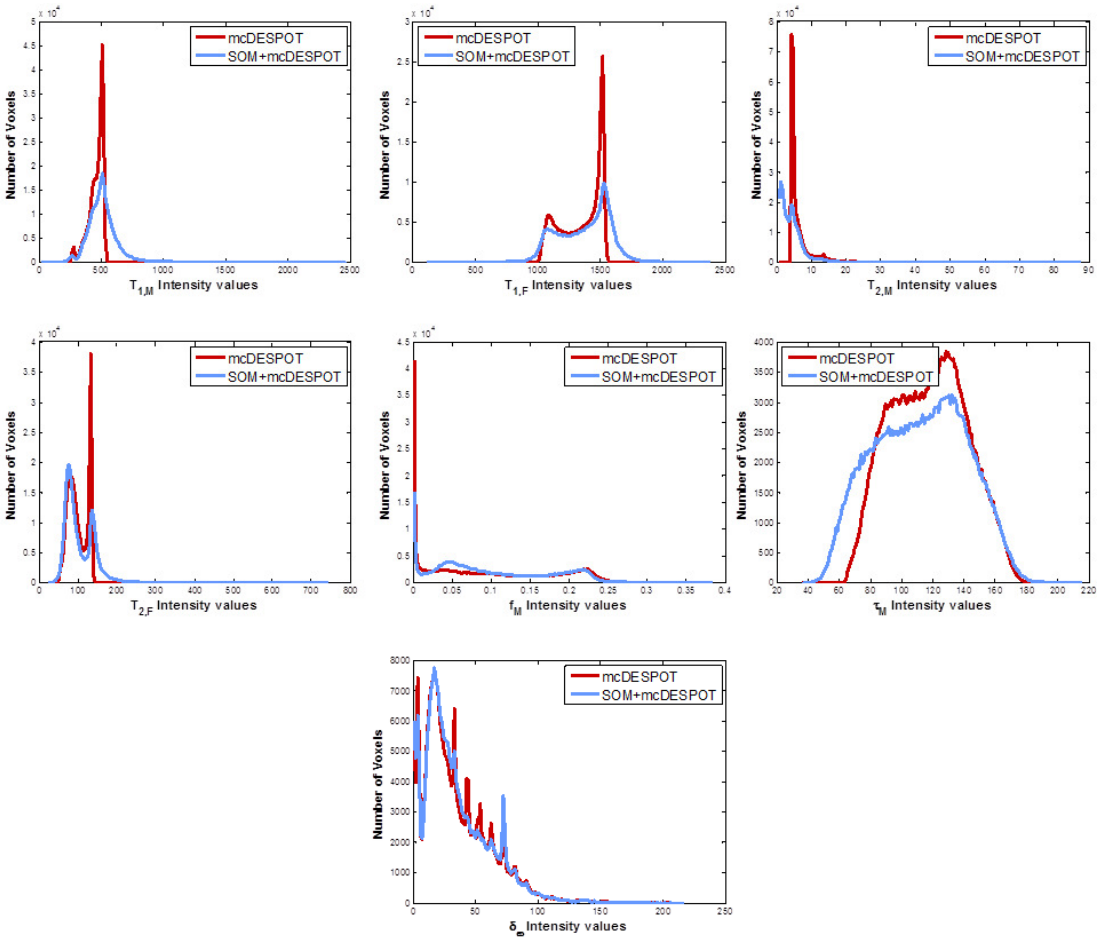

Figure 32. Histograms of the distribution of each parameter on the whole brain of C1.

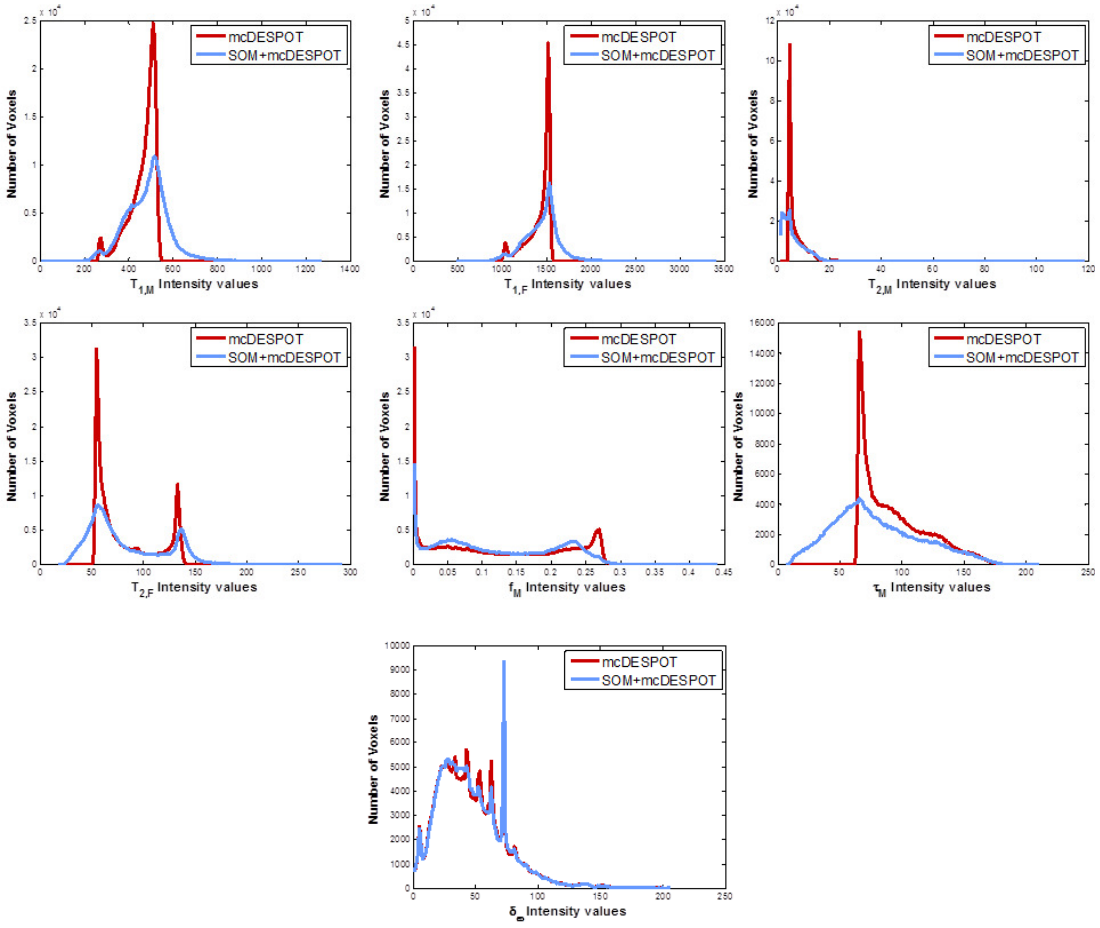

Figure 33. Histograms of the distribution of each parameter on the whole brain of P1.

3.2. Clinical application

The results obtained in the *in vivo* experiments were confirmed after applying SOM+mcDESPOT to a total of 65 subjects. Plotting the histograms of the f_M values in the NAWM highlighted the difference between the two procedures (i.e. SOM+mcDESPOT and mcDESPOT). In Figure 34 (a), an artificial second peak was

observed in all histograms obtained by averaging histograms across different groups. Using SOM+mcDESPOT, instead, that peak disappeared and the histograms resulted smoother and more feasible (Figure 34 b).

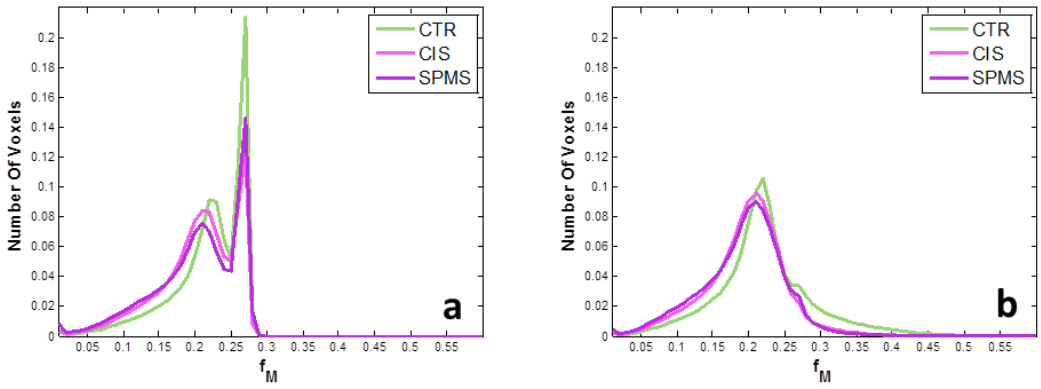

Figure 34. Histograms of the distribution of f_M in the NAWM. Comparison between mcDESPOT (a) and SOM+mcDESPOT (b) and among the different groups (controls, CIS and SPMS patients).

Considering the results obtained with SOM+mcDESPOT, the mean and the median of each f_M NAWM map were computed and compared across the different groups. The controls' f_M averaged values were found significantly higher than MS patients' ones ($p = 0.0117$). In particular, the drop in the values of SPMS subjects was found statistically significant compared to healthy ones ($p = 0.0144$), but not the drop in the CIS group ($p = 0.0537$). No difference was instead noticed between CIS and SPMS mean values, even if this results was not statistically significant ($p = 0.5683$). The same behaviour was registered considering the median values.

4. Discussion

This study demonstrates that using prior information extracted from MRI sequences can improve the nonlinear search implemented in the indirect quantification of brain myelin content performed by mcDESPOT.

Prior knowledge is generally used to guide the exploration of the search space, speeding up the convergence to a good solution and increasing the accuracy of the guessed solutions during the optimization process [68, 69]. Generally speaking, prior information deals with probability distributions that drive the search towards more

feasible regions, instead of scanning randomly all the domain (for instance, [70]). Unfortunately, in our case, a priori information of search space shape in terms of probability distributions is not known. However, another prior information can be extracted directly from the model: the exclusive connection between some feasible parameters and the corresponding signals (SPGR, SSFP0 and SSFP180 signals). Using both the *in silico* slice or brains, we showed how this connection permeates also the similarity relationship among voxels (each one defined by its 24 signals volumes and 7 parameters). Our findings, in fact, indicate that similar signals correspond to similar parameters, verifying one of the main hypotheses done at the beginning of this work. Using a large SOM, at least 74.21% of the voxels has the most similar one (in terms of parameters and signals) in the same cluster that it belongs to (Table 7). This means that the information on voxels similarity given by the clusters built and optimized in the signals space, is valid also in the parameters space for more than 74.21% of the times. This is a really important result because, on one hand, it establishes a link based on similarity among voxels, and, on the other hand, it legitimates to look for a voxel solution in the cluster c in which the voxel is mapped to, i.e. in the space defined by solutions that correspond to signals of similar voxels mapped to c. Since the nature of the MRI sequences signals, it is clear how signals reflect the tissue properties [36] and it is also known that different brain structures are characterized by different values of the 7 parameters previously described [41, 51, 52, 58, 71]. However, at the best of our knowledge, none has investigated the similarity relationship among voxels, in terms of signals and parameters, and, above all, none has used this information to drive the computation of $T_{1,M}, T_{2,M}, T_{1,F}, T_{2,F}, \tau_M, f_M$ and $\Delta\omega$.

The importance of this similarity relationship is further demonstrated through the validation phase performed using SOM+mcDESPOT. In the *in silico* noise free slice, for instance, for each voxel mapped to a certain cluster c, using solutions that are related to the voxel through a similarity relationship (i.e. using N_{DB} solutions randomly picked in c from the noise free database and up to $N_{subject}$ solutions from

voxels belonging to the processed subject and mapped to c) as feasible samples in the initial population of the optimization algorithm allows reducing both signals (63.65% of voxels using the NotSimplified fit, and 79.05% using the Simplified one) and parameters residuals (57.35% of voxels using the NotSimplified fit, and 65.88% using the Simplified one) at the first iteration (Figure 22 and 25). The SOM+mcDESPOT signals mean residuals, in fact, is about 25% or 70% (NotSimplified and Simplified fit, respectively) lower than mcDESPOT ones (Figure 22 c and d). Considering the SOM+mcDESPOT parameters mean residuals, instead, a gain of about 15% (NotSimplified fit) and 30% (Simplified fit) is reached (Figure 25 c and d). The same effect is observed processing the *in silico* slice characterized by SNR equal to 50 (Figure 29 and 30). Using SOM+mcDESPOT allows obtaining at least 56.27% (NotSimplified fit) and 71.45% (Simplified fit) of voxels with lower signals residuals that become 53.19% (NotSimplified fit) and 59.65% (Simplified fit) considering the voxels with lower parameters residuals at the first iteration (Table 9 and 10). Thus, the validation phase conducted on *in silico* images demonstrates how useful the similarity relationship among voxels is and how much more feasible the solutions suggested are, compared to the random ones. This initial improvement is reflected on both signals and parameters residuals and helps to achieve a higher accuracy after all process is executed. Moreover, the approach of suggesting similar solutions is more effective when the model is not complete and, so, less accurate, i.e. using 16 volumes to determine the Simplified fit.

These important results have been also validated through the processing of 6 subjects (3 patients and 3 controls). The SOM+mcDESPOT signals mean residuals are from 15% to 60% lower than mcDESPOT residuals at first iteration. The extent of the improvement is then lowered after 5 iterations, but a gain of at least 10% is still present (Figure 31). Since the results previously obtained for the *in silico* images, we can deduce that an improvement in terms of parameters is also reached. Moreover, SOM+mcDESPOT deletes an artificial effect caused by the initial extents of search space of each parameter. Plotting, in fact, the intensity values of the final solutions across the whole brain obtained with mcDESPOT shows very sharp peaks that are

unfeasible (Figure 32 and 33). These artificial effects are attributable to the optimization algorithm and to the initialization of the search space. The stochastic region contraction approach [59], in fact, is a method that, starting with a big search domain, is able to reduce this space considering only smaller feasible regions. In this sense, the search space contracts across all the iterations. In the mcDESPOT, at the first iteration, samples are randomly chosen from uniform distributions with boundaries defined as 95% and 105% of lower and upper bounds, respectively, reported in Figure 14 (a). At the second iteration, the new lower and upper bounds are established again. For instance, the new lower bound can be equal to 95% of the old one: this causes a slight enlargement of the search space, instead of a contraction. The process of randomly choosing solutions within the range defined by the 95% of the lower bound and 105% of the upper one is then repeated. The same procedure is followed in the next iterations. Designed like this, the optimization algorithm is able to overcome the possibility of being in a not promising region, evolving towards a more feasible one through enlargements, but it is a slow process. Using SOM+mcDESPOT, instead, allows seeding the initial population with feasible values beyond the original limits of each parameter. Since when the new lower and upper bounds are established no control is performed on their values (such as the new lower bound value must be greater than the old one and the new upper bound must be lower than the old one), one of or both boundaries can enlarge temporarily to allow a search in other promising regions. For this reason, SOM+mcDESPOT is able to eliminate the artificial effect noticed in the mcDESPOT results.

The application of SOM+mcDESPOT to 10 controls and 55 MS patients has reinforced the advantages described so far. The fractions of myelin-associated water have been investigated in the normal appearing white matter to evaluate the effect of the disease on the portion of tissue not involved into lesions. With the new method, the artificial peak showed in every histogram in Figure 34 (a) is definitively removed (Figure 34 b). This agrees with previous study on f_M, in which no second peaks are reported [47, 53, 72]. Analysing the mean and the median value of each subject's histogram, we observe a statistically significant difference between the group of

healthy participants and the patients ($p = 0.0117$). However, investigating better the differences among groups, for SPMS but not for CIS patients, mean f_M values were significantly lower ($p = 0.0144$) than the corresponding values for healthy controls. Confirmed by Kitzler's previous work [72], this result supports the hypothesis that the quantity of myelin in NAWM is significantly influenced by the progression of the disease [73].

Despite the remarkable advantages introduced by SOM+mcDESPOT, the new method still suffers from some limitations. The first one if that the similarity relationship is highly dependent on the model implemented in mcDESPOT. To couple the signals with the parameters, in fact, the equations (1) and (2) are solved. Even if the accuracy of the model has been demonstrated [51, 52], it is anyway a representation of the reality and not the reality. Moreover, the noise is not treated when a voxel is associated to its BMU: the signals belonging to the voxel are directly compared to noise free data. Despite the fact that we demonstrated that high noise level does not significantly influence the association voxel-its BMU (Table 8), however a small error could affect the process. Another limitation regards the optimization algorithm: this is designed and optimized just for random guessed solutions. Sometimes, the improvement of adding feasible samples to the population was deleted by the design of the search method (data not shown) even if it did not refer to a local minimum.

Hence, the further works can be designed. A new optimization algorithm or a modified stochastic region contraction will be implemented to better exploit the information contained in the feasible samples chosen from the SOM analysis. The aim will be to speed up the entire process. Moreover, a broader application will be performed to investigate the differences in the myelin-associated water fraction among MS patients and among different brain regions. Finally, a deeper analysis of the SOM as a segmentation method using the SPGR and bSSFP sequences will be conducted.

In conclusion, we proposed the novel method SOM+mcDESPOT that is able to extract and exploit the information contained in the MRI signals to drive appropriately the optimization algorithm implemented in mcDESPOT. In so doing, the overall accuracy of the method in both the signals fitting and in the determination of the 7 parameters improves. Thus, the outstanding potentiality of SOM+mcDESPOT could assume a crucial role in improving the indirect quantification of myelin in both healthy subjects and patients.

5. References

1. Purves D, Augustine GJ, Fitzpatrick D, Katz LK, LaMantia AS, McNamara JO, Williams SM: **Neuroscience**. 2nd edition. Sunderland (MA): Sinauer Associates; 2001.
2. Patestas MA, Gartner LP: **A textbook of neuroanatomy**: John Wiley & Sons; 2006.
3. Tomasch J: **Size, distribution, and number of fibers in the human corpus callosum**. *Anat Rec* 1954, **119**(1):119-135.
4. Alberts B, Johnson A, Lewis J, Raff M, Roberts K, Walter P: **Molecular Biology of the Cell**. New York: Garland Science; 2002.
5. Sherman DL, Brophy PJ: **Mechanisms of axon ensheathment and myelin growth**. *Nature Reviews Neuroscience* 2005, **6**(9):683-690.

6. Simons M, Trajkovic K: **Neuron-glia communication in the control of oligodendrocyte function and myelin biogenesis**. *Journal of Cell Science* 2006, **119**(21):4381-4389.
7. Bartsch U, Peshava P, Raff M, Schachner M: **Expression of janusin (J1-160/180) in the retina and optic nerve of the developing and adult mouse**. *Glia* 1993, **9**:57-69.
8. Raine CS: **Morphological aspects of myelin and myelination**. New York: Plenum Press; 1977.
9. Laule C, Vavasour IM, Kolind SH, Li DKB, Traboulsee TL, Moore GRW, MacKay AL: **Magnetic resonance imaging of myelin**. *Neurotherapeutics* 2007, **4**(3):460-484.
10. Pham-Dinh D, Baumann N: **Biology of Demyelinating Diseases**. In *Neurochemical Mechanisms in Disease. Volume 1*. Edited by Blass JP; 2011:537-583.
11. Craner MJ, Hains BC, Lo AC, Black JA, Waxman SG: **Co-localization of sodium channel Na(v)1.6 and the sodium-calcium exchanger at sites of axonal injury in the spinal cord in EAE**. *Brain* 2004, **127**:294-303.
12. Craner MJ, Newcombe J, Black JA, Hartle C, Cuzner ML, Waxman SG: **Molecular changes in neurons in multiple sclerosis: Altered axonal expression of Na(v)1.2 and Na(v)1.6 sodium channels and Na(+)/Ca(2+) exchanger**. *Proceedings of the National Academy of Sciences of the United States of America* 2004, **101**(21):8168-8173.
13. Coman L, Barbin G, Charles P, Zalc B, Lubetzki C: **Axonal signals in central nervous system myelination, demyelination and remyelination**. *Journal of the Neurological Sciences* 2005, **233**(1-2):67-71.
14. Ogawa Y, Schafer DP, Horresh I, Bar V, Hales K, Yang Y, Susuki K, Peles E, Stankewich MC, Rasband MN: **Spectrins and ankyrinB constitute a specialized paranodal cytoskeleton**. *Journal of Neuroscience* 2006, **26**(19):5230-5239.
15. Kantarci O, Wingerchuk D: **Epidemiology and natural history of multiple sclerosis: new insights**. *Current Opinion in Neurology* 2006, **19**(3):248-254.
16. Kantarci OH, Weinshenker BG: **Natural history of multiple sclerosis**. *Neurologic Clinics* 2005, **23**(1):17-38.
17. Hauser SL, Oksenberg JR: **The neurobiology of multiple sclerosis: Genes, inflammation, and neurodegeneration**. *Neuron* 2006, **52**(1):61-76.
18. Kornek B, Lassmann H: **Axonal pathology in multiple sclerosis. A historical note**. *Brain Pathology* 1999, **9**(4):651-656.
19. Bitsch A, Schuchardt J, Bunkowski S, Kuhlmann T, Bruck W: **Acute axonal injury in multiple sclerosis - Correlation with demyelination and inflammation**. *Brain* 2000, **123**:1174-1183.
20. Ferguson B, Matyszak MK, Esiri MM, Perry VH: **Axonal damage in acute multiple sclerosis lesions**. *Brain* 1997, **120**:393-399.
21. Trapp BD, Peterson J, Ransohoff RM, Rudick R, Mork S, Bo L: **Axonal transection in the lesions of multiple sclerosis**. *New England Journal of Medicine* 1998, **338**(5):278-285.

22. Ormerod IEC, Miller DH, McDonald WI, Duboulay E, Rudge P, Kendall BE, Moseley IF, Johnson G, Tofts PS, Halliday AM *et al*: **THE ROLE OF NMR IMAGING IN THE ASSESSMENT OF MULTIPLE-SCLEROSIS AND ISOLATED NEUROLOGICAL LESIONS - A QUANTITATIVE STUDY**. *Brain* 1987, **110**:1579-1616.
23. Kurtzke JF: **Rating neurological impairment in multiple sclerosis: An expanded disability status scale (EDSS)**. *Neurology* 1983, **33**:1444-1452.
24. Confavreux C, Vukusic S: **Natural history of multiple sclerosis: a unifying concept**. *Brain* 2006, **129**:606-616.
25. Confavreux C, Vukusic S: **Natural history of multiple sclerosis: implications for counselling and therapy**. *Current Opinion in Neurology* 2002, **15**(3):257-266.
26. Langer-Gould A, Popat RA, Huang SM, Cobb K, Fontoura P, Gould MK, Nelson LM: **Clinical and demographic predictors of long-term disability in patients with relapsing-remitting multiple sclerosis - A systematic review**. *Archives of Neurology* 2006, **63**(12):1686-1691.
27. Confavreux C, Vukusic S: **Age at disability milestones in multiple sclerosis**. *Brain* 2006, **129**:595-605.
28. Binquet C, Quantin C, Le Teuff G, Pagliano JF, Abrahamowicz M, Moreau T: **The prognostic value of initial relapses on the evolution of disability in patients with relapsing-remitting multiple sclerosis**. *Neuroepidemiology* 2006, **27**(1):45-54.
29. Feldmann M, Steinman L: **Design of effective immunotherapy for human autoimmunity**. *Nature* 2005, **435**(7042):612-619.
30. Hohlfeid R, Wekerle H: **Autoimmune concepts of multiple sclerosis as a basis for selective immunotherapy: From pipe dreams to (therapeutic) pipelines**. *Proceedings of the National Academy of Sciences of the United States of America* 2004, **101**:14599-14606.
31. Noseworthy JH: **Management of multiple sclerosis: current trials and future options**. *Current Opinion in Neurology* 2003, **16**(3):289-297.
32. Young IR, Hall AS, Pallis CA, Legg NJ, Bydder GM, Steiner RE: **Nuclear magnetic-resonance imaging of the brain in multiple-sclerosis**. *Lancet* 1981, **2**(8255):1063-1066.
33. Sormani MP, Molyneux PD, Gasperini C, Barkhof F, Yousry TA, Miller DH, Filippi M: **Statistical power of MRI monitored trials in multiple sclerosis: new data and comparison with previous results**. *Journal of Neurology Neurosurgery and Psychiatry* 1999, **66**(4):465-469.
34. Filippi M, Rocca MA: **Conventional MRI in multiple sclerosis**. *Journal of Neuroimaging* 2007, **17**:3S-9S.
35. O'Riordan JI, Thompson AJ, Kingsley DPE, MacManus DG, Kendall BE, Rudge P, McDonald WI, Miller DH: **The prognostic value of brain MRI in clinically isolated syndromes of the CNS - A 10-year follow-up**. *Brain* 1998, **121**:495-503.
36. Haacke EM, Brown RW, Thomposon MR, Venkatesan R: **Magnetic Resonance Imaging. Physical Principles and Sequence Design**.Wiley-Liss; 1999.
37. Bloembergen N, Purcell EM, Pound RV: **Relaxation effects in nuclear magnetic resonance absorption**. *Physical Review* 1948, **73:**679-712.

38. Bo L, Vedeler CA, Nyland H, Trapp BD, Mork SJ: **Intracortical multiple sclerosis lesions are not associated with increased lymphocyte infiltration**. *Multiple Sclerosis* 2003, **9**(4):323-331.
39. Neema M, Stankiewicz J, Arora A, Dandamudi VSR, Batt CE, Guss ZD, Al-Sabbagh A, Bakshi R: **T1-and T2-based MRI measures of diffuse gray matter and white matter damage in patients with multiple sclerosis**. *Journal of Neuroimaging* 2007, **17**:16S-21S.
40. Bitsch A, Kuhlmann T, Stadelmann C, Lassmann H, Lucchinetti C, Bruck W: **A longitudinal MRI study of histopathologically defined hypointense multiple sclerosis lesions**. *Annals of Neurology* 2001, **49**(6):793-796.
41. Deoni SC, Rutt BK, Peters TM: **Rapid combined T1 and T2 mapping using gradient recalled acquisition in the steady state**. *Magn Reson Med* 2003, **49**(3):515-526.
42. Meiboom S, Gill D: **Modified spin-echo method for measuring nuclear relaxation times**. *Review of Scientific Instruments* 1958, **29**(8):688-691.
43. Oppelt A, Graumann R, Barfuss H, Fischer H, Hartl W, Schajor W: **Fast imaging with steady precession a new fast magnetic resonance imaging sequence**. *Electromedica (English Edition)* 1986, **54**(1):15-18.
44. Carr HY, Purcell EM: **Effects of diffusion on free precession in nuclear magnetic resonance experiments**. *Physical Review* 1954, **94**(3):630-638.
45. Whittall KP, MacKay AL, Li DKB: **Are mono-exponential fits to a few echoes sufficient to determine T-2 relaxation for in vivo human brain?** *Magnetic Resonance in Medicine* 1999, **41**(6):1255-1257.
46. Bjarnason TA, Vavasour IM, Chia CLL, MacKay AL: **Characterization of the NMR behavior of white matter in bovine brain**. *Magnetic Resonance in Medicine* 2005, **54**(5):1072-1081.
47. MacKay A, Laule C, Vavasour I, Bjarnason T, Kolind S, Madler B: **Insights into brain microstructure from the T-2 distribution**. *Magnetic Resonance Imaging* 2006, **24**(4):515-525.
48. Fischer HW, Rinck PA, Vanhaverbeke Y, Muller RN: **Nuclear-relaxation of human brain gray and white matter - Analysis of field-dependence and implications for MRI**. *Magnetic Resonance in Medicine* 1990, **16**(2):317-334.
49. Menon RS, Allen PS: **Application of continuous relaxation-time distributions to the fitting of data from model systems and excised tissue**. *Magnetic Resonance in Medicine* 1991, **20**(2):214-227.
50. Stewart WA, Mackay AL, Whittall KP, Moore GRW, Paty DW: **Spin-spin relaxation in experimental allergic encephalomyelitis - Analysis of CPMG data using a nonlinear least-squares method and linear inverse-theory**. *Magnetic Resonance in Medicine* 1993, **29**(6):767-775.
51. Deoni SCL, Rutt BK, Arun T, Pierpaoli C, Jones DK: **Gleaning Multicomponent T1 and T2 Information From Steady-State Imaging Data**. *Magnetic Resonance in Medicine* 2008, **60**(6):1372-1387.
52. Deoni SCL: **Correction of Main and Transmit Magnetic Field (B0 and B1) Inhomogeneity Effects in Multicomponent-Driven Equilibrium Single-Pulse**

Observation of T1 and T2. *Magnetic Resonance in Medicine* 2011, **65**(4):1021-1035.

53. Laule C, Leung E, Li DKB, Troboulsee AL, Paty DW, MacKay AL, Moore GRW: **Myelin water imaging in multiple sclerosis: quantitative correlations with histopathology**. *Multiple Sclerosis* 2006, **12**(6):747-753.
54. Christensen KA, Grant DM, Schulman EM, Walling C: **Optimal determination of relaxation-times of Fourier-transform nuclear magnetic-resonance - Determination of spin-lattice relaxation-times in chemically polarized species**. *Journal of Physical Chemistry* 1974, **78**(19):1971-1977.
55. McConnell HM: **Relaxation rates by nuclear magnetic resonance**. *J Chem Phys* 1958, **28**:430-431.
56. Freeman R, Hill HDW: **Phase and intensity anomalies in Fourier transform NMR**. *Journal of Magnetic Resonance* 1971, **4**(3):366-&.
57. Zur Y, Wood ML, Neuringer LJ: **Motion-insensitive, steady-state free precession imaging**. *Magnetic Resonance in Medicine* 1990, **16**(3):444-459.
58. Deoni SCL: **High-resolution T1 mapping of the brain at 3T with driven equilibrium single pulse observation of T1 with high-speed incorporation of RF field inhomogeneities (DESPOT1-HIFI)**. *Journal of Magnetic Resonance Imaging* 2007, **26**(4):1106-1111.
59. Berger MF, Silverman HF: **Microphone array optimization by stochastic region contraction**. *Ieee Transactions on Signal Processing* 1991, **39**(11):2377-2386.
60. Hebb D: **The organization of behavior**. New York: Wiley; 1949.
61. Marr D: **A theory of cerebellar cortex**. *Journal of Physiology-London* 1969, **202**(2):437-470.
62. Willshaw DJ, Buneman OP, Longuet-Higgins HC: **Non-holographic associative memory**. *Nature* 1969, **222**(5197):960-962.
63. von der Malsburg C: **Self-organization of orientation sensitive cells in the striate cortex**. *Kybernetik* 1973, **14**(2):85-100.
64. Willshaw DJ, Malsburg CVD: **How patterned neural connections can be set up by self-organization**. *Proceedings of the Royal Society of London Series B-Biological Sciences* 1976, **194**(1117):431-445.
65. Kohonen T: **Self-organized formation of topologically correct feature maps**. *Biological Cybernetics* 1982, **43**(1):59-69.
66. Kohonen T: **Self-Organizing Maps**. Berlin: Springer; 1995.
67. Rice SO: **Mathematical analysis of random noise. I-IV**. *Bell System Technical Journal* 1944, **23**:282-332.
68. Haubelt C, Gamenik J, Teich J: **Initial population construct for convergence improvement of MOEAs**. In *Evolutionary Multi-Criterion Optimization. Volume 3410*. Edited by Coello CACAAHZE; 2005:191-205.
69. Hill RR, Hiremath C: **Improving genetic algorithm convergence using problem structure and domain knowledge in multidimensional knapsack problems**. *International Journal of Operational Research* 2005, **1**(1-2):145-159.

70. Gao S, Wang X: **Quantitative utilization of prior biological knowledge in the Bayesian network modeling of gene expression data**. *Bmc Bioinformatics* 2011, **12**:359.
71. Deoni SCL: **Magnetic Resonance Relaxation and Quantitative Measurement in the Brain**. In *Magnetic Resonance Neuroimaging: Methods and Protocols. Volume 711*. Edited by Modo MBJWM; 2011:65-108.
72. Kitzler HH, Su J, Zeineh M, Harper-Little C, Leung A, Kremenchutzky M, Deoni SC, BK. R: **Deficient MWF mapping in multiple sclerosis using 3D whole-brain multi-component relaxation MRI**. *Neuroimage* 2011 [Epub ahead of print].
73. Husted C: **Structural insight into the role of myelin basic protein in multiple sclerosis**. *Proceedings of the National Academy of Sciences of the United States of America* 2006, **103**(12):4339-4340.

6. Appendix

In this chapter, a brief description of two other main projects that I did during my PhD school is reported.

6.A. Discovering information in OGTT curves shape for predicting the metabolic condition in women with previous gestational diabetes

6.A.1. Abstract

Gestational diabetes mellitus (GDM) makes women at risk of type 2 diabetes during their life. Here, we proposed OGTT curve shapes at baseline as predictor of this later abnormal glucose intolerance. To test our hypothesis, we analysed a total of 253 glucose, insulin and C-peptide OGTT curves of women with a history of GDM and 40 controls. Firstly, shapes peculiar of different glucose tolerance conditions were investigated by Self-Organizing Maps. These shapes were then used to build a classifier based on Kullback-Liebler distance to test if previous GDM affects shapes of curves classified as normal after delivery, and if glucose, insulin and C-peptide kinetics measured at time T_0 can predict metabolic evolution within two years. As results, two most common morphologies, monophasic and triphasic, related respectively to a diabetic and normal condition, were identified. Using these shapes as reference, the classifier did not highlight any influence of previous GDM on normal curves. It underlined instead the great potential of shapes in predicting metabolic evolution: for example, 82.6% of women that developed diabetes within two years was correctly predicted using glucose curve information. This shows how shape of OGTT curves can reflects still not symptomatic changes occurring in glucose metabolism.

6.A.2. Introduction

Gestational diabetes mellitus (GDM) is defined as the diabetic condition during pregnancy [1] with symptoms close to type 2 diabetes, i.e., an increased insulin resistance, and a decline in insulin secretion [2, 3]. GDM prevalence seems to be proportional to type 2 diabetes occurrences, ranging from 1% to 14% of all pregnancies depending on the population studied [4]. Shortly after delivery, glucose homoeostasis is commonly restored to the antepartum condition, but women with a history of GDM often show high blood pressure, atherogenic lipid profiles [5, 6], and have a high risk of developing type 2 diabetes [7]. A systematic review showed that the incidence of diabetes among women with a history of GDM ranges from 3% to 65%, because of differences in the duration of the follow-up period and ethnicity [8]. This means that women who had gestational diabetes have at least a seven-fold increased risk of developing type 2 diabetes compared with those who had a normoglycaemic pregnancy [9]. Moreover, the risk of type 2 diabetes seems to be maintained for several years, making necessary the monitoring of women glucose tolerance condition. Knowledge of early metabolic abnormalities that predispose to diabetes may be useful for development of rational prevention strategies. For this reason, it is generally recommended that women with GDM undergo testing for glycemia within the first 6 months postpartum [10, 11] and women who are found to have pre-diabetes or diabetes on this test typically will receive counseling on lifestyle modification and possibly anti-diabetic therapy [12]. However, the majority of women with GDM have normal glucose tolerance on this early postpartum testing, despite their considerable risk of future T2DM [13]. For this reason, there is the need to find reliable prognostic factors that are able to predict this risk.

In the last years, different antepartum and postpartum independent predictors of later abnormal glucose tolerance have been identified [14-18]. Indicators such as family

history of diabetes, recurrence of GDM, maternal age, body mass index and metabolic factors (i.e., high fasting glucose level during pregnancy, impaired β-cell function, areas under curves for OGTT glucose and insulin curves) were reported to be predictive for development of diabetes postpartum [6, 8, 19-21]. However a clear, automatic, reliable method for predicting the risk of diabetes starting from a GDM condition is still lacking.

The main aim of this study is to give a contribution to the identification of tools for the prediction of the metabolic condition in women with a history of gestational diabetes. In particular, since the shape of OGTT curves has been studied as related to glucose tolerance condition [22-24], we focus our attention on glucose, insulin and C-peptide curves derived from OGTTs of women with former GDM. Here we hypothesize that an evolution towards a normal or type 2 diabetes condition is predictable from the entire morphology of the OGTT curves at baseline.

A multiple-step analysis is performed to evaluate whether the metabolic condition of GDM subjects can be predictable or not from the morphological features of the OGTT curves. Firstly, we investigate if a relationship exists between the shape of OGTT curves and the glucose tolerance condition. To do it, we apply an unsupervised neural network, i.e., the Self-Organizing Maps (SOMs) to a control group (normal glucose tolerance without previous GDM) and a group affected by type 2 diabetes and with a history of previous GDM. Then, a classifier based on a similarity measure, i.e., the Kullback-Liebler distance (*KLd*) is applied to OGTT curves to classify a so called normal group (normal glucose tolerance with previous GDM) with the aim to test if a memory of the previous disease is maintained in the morphology of the NGT curves (memory-of-disease-driven shape hypothesis). Finally, the same classifier was applied to predict the metabolic condition at time T_{fu} from glucose (GLU), insulin (INS) and C-peptide (CPEP) kinetics measured at time T_0. The rationale for this approach is that we conjecture that the evolution from a condition A at time T_0 to a condition B at time T_{fu} could be traceable in the shape of

OGTT curves at time T_0. This means that the morphology of the kinetics curves of condition A-subjects at time T_0 show features that are similar to the kinetics curves of condition B-subjects at time T_{fu}.

Summarizing, the goal of the study is evaluating (a) if there are morphological features in OGTT curves that are peculiar of different glucose tolerance conditions, (b) if there is a memory of the previous disease (i.e. GDM) in the shape of OGTT curves of subjects classified as having normal glucose tolerance, and finally (c) if the shape of OGTT curves at time T_0 can be used to predict the evolution of the glucose tolerance status at time point T_{fu}.

6.A.3. Materials and Methods

Subjects and test

The OGTT curves of 178 Caucasian women (138 with a history of GDM, and 40 controls -CNT-, i.e. with previous uncomplicated pregnancy and with normal glucose tolerance at the time of the study) were investigated. All women were recruited during pregnancy from the outpatient department of the University Clinic of Vienna, and gave written informed consent for participation in the study, which was approved by the local Ethics Committee. The population here investigated underwent up to five years follow-up.

After an overnight fast, all the 178 subjects underwent a standard 75-g OGTT with venous blood samples collected at fasting and at 10, 20, 30, 60, 90, 120, 150 and 180 min afterward. Plasma glucose was measured with the glucose oxidase method by an automated glucose analyzer (Beckman, Fullerton, CA), with an interassay coefficient of variation <2%. Insulin (Serono Diagnostics, Freiburg, Germany) and C-peptide (CIS Bio International, Gif-sur-Yvette, France) were determined in duplicate by

commercially available radioimmunoassay kits, with an interassay coefficient of variation <5%.

The glucose curves showed values matching the American Diabetes Association 2003 criteria [25] for normal glucose tolerance (NGT), impaired glucose metabolism (including impaired glucose tolerance and/or impaired fasting glucose, IGT), and type 2 diabetes (T2DM). In this study, we referred to NGT as 'normal' condition, while to IGT and T2DM as 'diabetic' one.

The entire analysis was performed on a total of 293 curves ($n_{CNT} = 40$; $n_{NGT} = 182$; $n_{IGT} = 34$; $n_{T2DM} = 37$) reported in Figure A1.

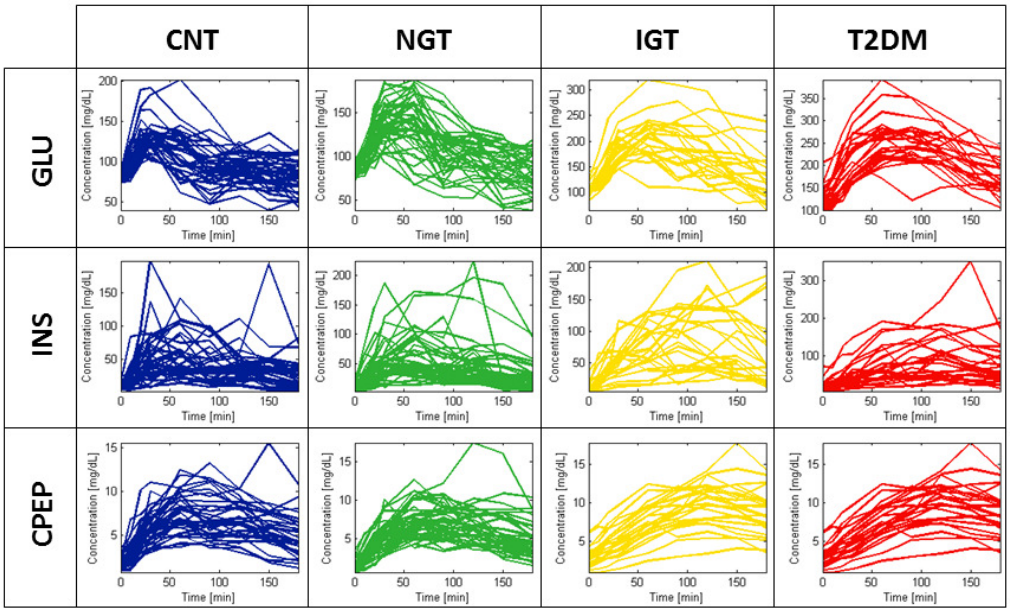

Figure A1. Curves measured by OGTT. Each row represents a type of curves measured by the Oral Glucose Tolerance Test: first row is referred to Glucose (GLU) curves, the second to Insulin (INS) and the third to C-peptide (CPEP). The first column shows curves belonging to the controls, i.e. women with previous pregnancy/pregnancies not affected by gestational diabetes (GDM). The other columns group Glucose, Insulin and C-peptide curves of women with previous GDM according to the ADA criteria [25]. More in detail, the second column represents women with a restored normal glucose tolerance (NGT), the third women with an impaired glucose tolerance (IGT), and the last one show curves of women that have develop type 2 diabetes (T2DM).

GLU, INS, CPEP curves and a combination of them, given by glucose and insulin (GLU+INS), insulin and C-peptide (INS+CPEP), glucose and C-peptide (GLU+CPEP) and glucose and insulin and C-peptide curves (GLU+INS+CPEP) were considered. The combination was simply obtained queuing two or three type of curves.

Some of the OGTT data presented here were already included in previous studies [22, 26].

Curve morphology and information

To evaluate whether specific shapes are associated to different conditions or not, we investigated the existence of specific morphological features in normal and diabetic OGTT curves. To do it, 65 subjects were considered and their OGTT curves at baseline were used ($n_{CNT} = 40$; and $n_{T2DM} = 25$).

Self-Organizing Maps (SOMs) are applied to test the OGTT curve shape hypothesis. A SOM is a subtype of artificial neural network which uses a competitive learning technique to train itself in an unsupervised manner [27]. It consists of nodes (neurons) that, arranged as a regular, two dimensional lattice, are directly associated with a weight vector, called prototype vector. In a SOM, weight vectors are set in order to achieve a configuration where the distribution of the input data is reflected and the most important metric relationships are preserved. In this way, data that are "similar" in the input space map to nearby neurons on the lattice. This feature of a SOM is enforced by a competitive learning, performed in an iteratively manner. Briefly, at each training step t, a data sample x is selected from the input space and, as a rule, its distance from all prototype vectors is computed. In this application, the Kullback-Liebler distance was adopted. *KLd* is a similarity measure between conceptual reality, p, and approximating model, q [28]. It is widely used in information theory, even if in the last years it was applied to other fields such as image analysis and classification problems.

For discrete distributions, the basic *KLd* is defined as:

$$KLd(p,q) = \sum_i p(i) log_2 \frac{p(i)}{q(i)} \quad (1)$$

$$\Sigma_i p(i) = 1 \;\; ; \Sigma_i q(i) = 1$$

$$p(i) > 0 \;\; \forall i$$

$$q(i) > 0 \;\; \forall i$$

$$KLd(p,q) = 0 \;\; if \; p = q$$

Roughly, *KLd(p,q)* is the information lost when *q* is used to approximate *p*. Since the definition of the Kullback-Liebler distance in Eq. (1) is asymmetric, here we used a symmetric version:

$$KLd(p,q) = \frac{1}{2}\left(\sum_i p(i) log_2 \frac{p(i)}{q(i)}\right)\left(\sum_i q(i) log_2 \frac{q(i)}{p(i)}\right) \quad (2)$$

In this study the *KLd* was preferred to other distance measures because of its property to include the order of samples in the formula. In fact, each variation occurring at sample *i* is weighted by the values that curves *p* and *q* assume at sample *i* (equations 1 and 2), thus weighting properly local shape changes.

A winning neuron *c* (called Best Matching Unit, BMU), whose prototype vector *m(c)* is the most similar to the input sample *x,* is determined on the basis of the value of the KL distance of *x* from prototype vectors. The weight vector *m(c)* is modified in order to match the sample *x* even closer. As an extension to standard competitive learning, the neurons surrounding the BMU are adapted as well (Figure A2 a) and their prototype vectors *m(i)* are also moved towards the sample *x*, during the training time *t*, following the update rule

$$m(i,t+1) := m(i,t) + h_{ci}(t) \cdot [x - m(i,t)] \quad (3)$$

where the scalar factor $h_{ci}(t)$ is referred to a neighbourhood function.

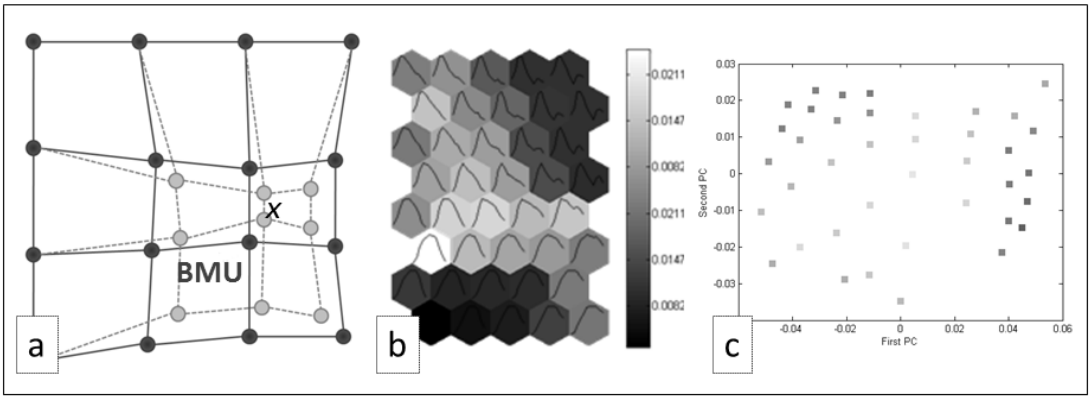

Figure A2. SOM training process (a), U-matrix (b) and principal components plot (c). The SOM is a two dimensional lattice, in which each neuron is directly associated to a weight vector, called prototype vector. The principal objective of a Self-organizing map is to modify these weight vectors in order to achieve a configuration in which the distribution of the input data is reflected. For each data sample *x* selected from the input space, the most similar prototype vectors (called Best Matching Unit, BMU) is detected. BMU and its neighbouring are adapted to the input curve *x*. Solid lines represent the situation before the updating phase, while dashed lines after (a). At the end of the training, each neuron is characterised by an updated prototype vector that is more or less similar to its neighbours. The U-matrix (the unified distance matrix) represents this similarity because it shows the distance among neurons. In this case (b), dark colours stand for low distance values, while light one for high distance values. Nevertheless, sometimes, the U-matrix interpretation can be very hard, especially for small U-matrices. For this reason, to visually depict clusters, we plotted also the prototype vectors in their first two principal components space (c). The colours of squares correspond to distance values reported in the U-matrix.

In this study we used a Gaussian distribution for $h_{ci}(t)$, which decreases from the neighbourhood centre node $r(c)$ to the outer limits of the neighbourhood $r(i)$ as follows

$$h_{ci}(t) = \alpha(t) \cdot exp\left[-\frac{\|r(c)-r(i)\|^2}{2\cdot\sigma(t)^2}\right] \quad (4)$$

The term $\alpha(t)$ in Eq. (4) is the so called learning rate and it can be regarded as the height of the neighbourhood kernel, while $o(t)$ is the radius or the width of the neighbourhood kernel and it specifies the region of influence that the input sample x has on the map. Both the height and the width of the neighbourhood function decrease monotonically with the increase of the training time.

As can be seen from equation (4), neurons closer to the best matching unit will be adjusted more than nodes further away. Moreover, while at the beginning the best matching unit is heavily modified and the neighbourhood is fairly large, modifications become more and more irrelevant as the learning process takes place. Given that not only the winning node is tuned towards the input pattern but also the neighbouring nodes, it is expected that similar input patterns in future training cycles will find their best matching weight vector at nearby neurons on the map: the more similar two input patterns are, the closer their best matching units are likely to be on the final map [29].

In this study SOMs were designed as hexagonal lattice maps. A linear initialization of prototype vectors was adopted and a batch training algorithm was applied. The dimension of the grid depended on the size of subsets used.

A visual representation of the similarity among neurons can be obtained by plotting the Unified distance matrix (U-matrix), i.e., the matrix of the distances among adjacent neurons: high values in the matrix indicate a frontier region between clusters, while low values highlight high degree of similarity among neurons on a region, i.e. low U-matrix values identify clusters. This can be visually rendered using a colour map, in which, for instance, dark colour stands for low distance value and light colour for high distance value (Figure A2 b). Being sometimes the U-matrix map hard to be interpreted by visual inspection, especially for small U-matrices, we also applied the Principal Components Analysis (PCA). PCA allows identifying new variables, the principal components, which are linear combinations of the original variables. Briefly, the first principal component is the direction along which data show the largest variation; the second component is the direction of largest variance which is perpendicular to the first principal component; and so on. In general, the *k*-

th principal component is the leading component of the variance after subtracting off the first *k-1* components. Exhaustive detail on the Principal Components Analysis can be found in [30]. Here we plotted the prototype vectors in the first two principal components (PCs) space (Figure A2 c) to visually depict clusters: this visualization allows to integrate the visual inspection of the U-matrix map because it plots the first two uncorrelated components in which the meaningful amounts of variance is stored.

To investigate whether curves can be someway clustered exclusively in terms of their morphology, or if there is an influence of each sample exact value, the analysis was conducted both on measured and normalized curves (i.e. the area under curves became equal to 1). In the latter, two different normalization procedures were followed when combination of curves were considered: (a) the not-normalized OGTT curves were serialized, and the resulting curve was then normalized; and (b) GLU, INS, and CPEP curves were separately normalized, serialized, and then the resulting curve was again normalized to obtain the area under curve equal to 1.

Since we are interested in the individuation of peculiar morphological features characterizing OGTT curves of normal and diabetic subjects, we built up two reference curves. Those curves were obtained by averaging prototype vectors of the two major clusters derived from SOMs analysis (as described in the previous section) and they were used in the following two other steps.

Curve morphology and classification

To test memory-of-disease-driven shape hypothesis, i.e., if a memory of the previous disease (the GDM condition) is maintained in the morphology of the NGT curves, a similarity measure between the reference OGTT curves and the 43 NGT ones (derived from baseline OGTT of 43 NGT subjects) was performed.
The similarity measure between reference and individual OGTT curves was calculated using the Kullback-Leibler distance (equation 2). The analysis was

conducted on normalized OGTT curves (i.e. the area under curves became equal to 1) as follows: for each NGT curve measured, the distance from reference curves was computed and, according to the distance values, a normal or diabetic classification was provided.

Curve morphology and prediction

To evaluate the potency of the OGTT curves shape at time T_0 as predictor of the metabolic state at time T_{fu}, a similarity measure between the reference OGTT curves and a subset of 185 individual curves was performed. All 185 OGTT curves considered here belong to subjects with a recorded follow up: at time point T_{fu} subjects became or remained 'normal' in 139 cases and 'diabetic' in 46 cases. For this analysis, the difference between T_{fu} and T_0 was less than 2 years, i.e. we predicted the evolution within two years from T_0, and more than one curve for each subject could be used. The similarity measure between reference and individual OGTT curves was calculated using the Kullback-Leibler distance (equation 2). The analysis was conducted on normalized OGTT curves (i.e. the area under curves became equal to 1) as follows: for each OGTT curve measured at time point T_0, the distance from reference curves was computed and, according to the distance values, normal or diabetic evolution of the subject was predicted. As the real follow up is well known, a contingency table was built and sensitivity and specificity were computed. Moreover, a statistical analysis (Chi Square Test) was also performed.

The whole study was performed in the MATLAB environment (The MathWorks, Inc., Natick, MA).

6.A.4. Results

Morphology and Information

The morphological analysis showed that considering measured or normalized curves did not introduce any significant difference. In fact, despite normalization process made curves closer to each other (Figure A3), it did not produce different results, and similar SOMs were obtained maintaining or normalizing the exact value of OGTT sample.

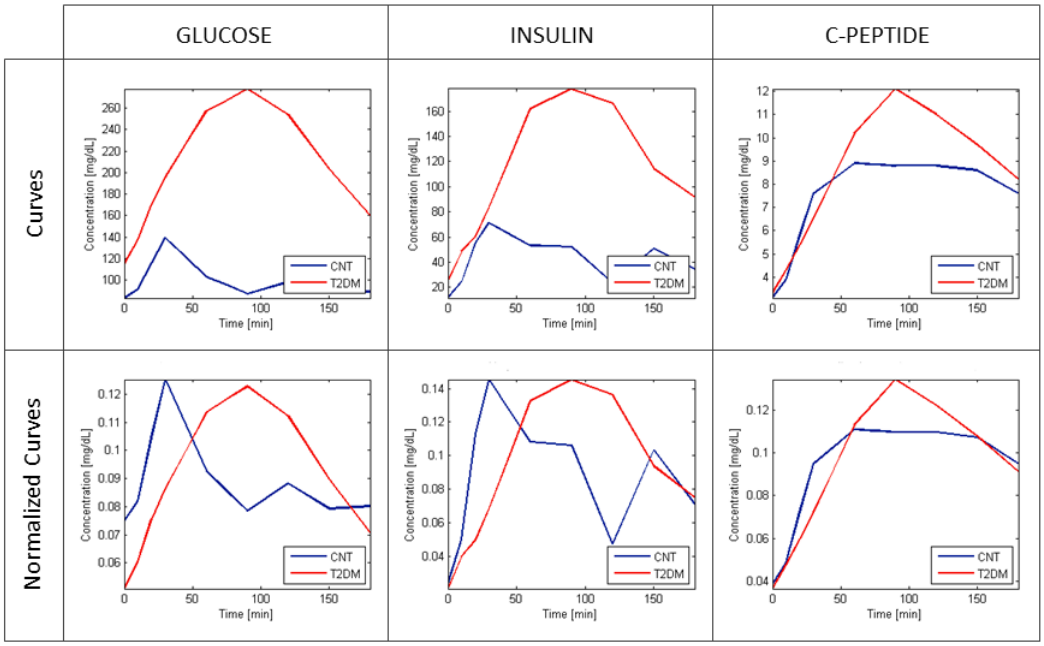

Figure A3. Comparison between measured curves and normalized ones. To evaluate the influence of shape on different Glucose conditions, the curves were normalized, i.e. the area under the curves was made equal to 1. The effect of this normalization process is clear if two examples of curves from the controls and the T2DM group are compared. The first row shows Glucose, Insulin and C-peptide curves as they were measured by OGTT: the differences between CNT and T2DM groups are due to the shape and to the values of each curve sample. In the second row, instead, normalized curves are plotted: the differences, in this case, are generated only by morphology.

For this reason, in the forthcoming we present only results obtained over the normalized OGTT curves. Moreover, when combination of curves was considered,

only the results obtained on OGTT curves normalized after their serialization are reported here, since they were found more predictive.

The application of SOMs to investigate on the existence of different morphological features in OGTT curves of CNT and T2DM groups shows interesting results. The visual inspection of the U-matrices shows the presence of two clearly distinct dark clusters (Figure A4), corresponding to different curve shapes.

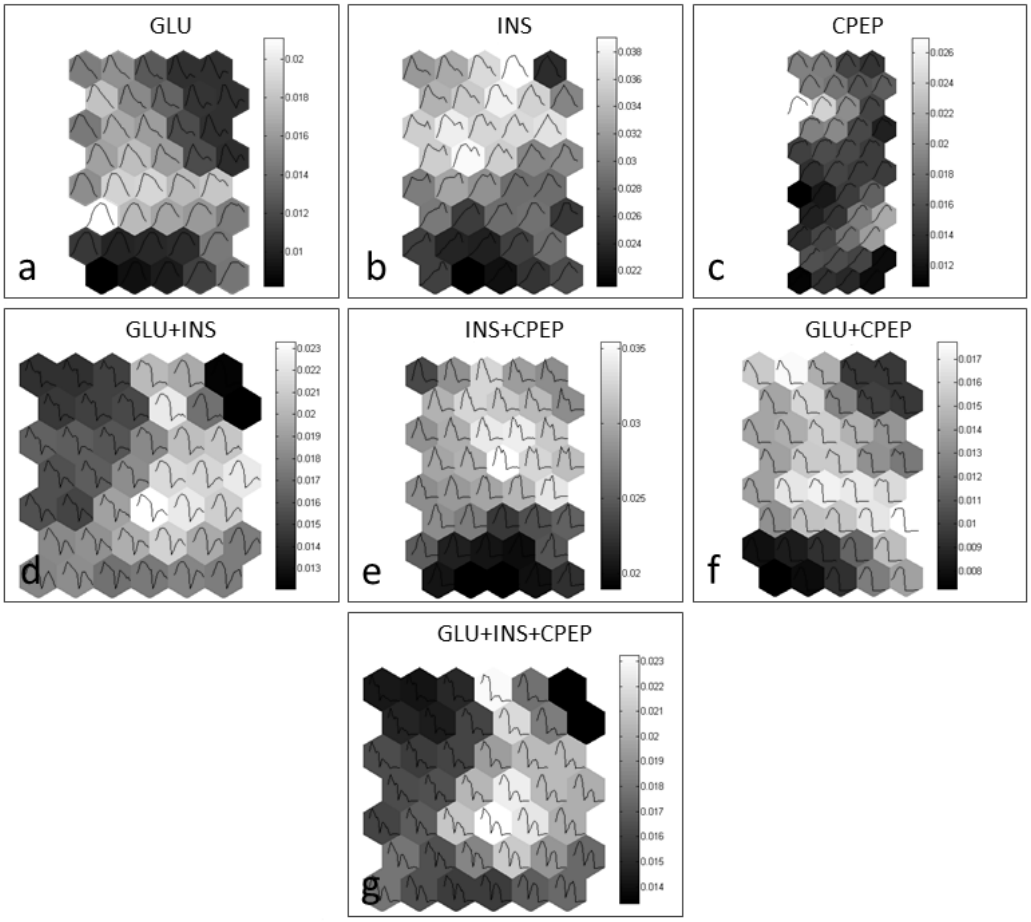

Figure A4. U-matrices of SOMs trained with CNT and T2DM groups. The controls and the diabetic groups were considered. Sets of GLU, INS, CPEP, GLU+INS, INS+CPEP, GLU+CPEP and GLU+INS+CPEP were used for training the SOMs and for generating the U-matrices. Neurons characterised by darker colours have lower distance values from neighbours, while lighter neurons have higher distances. Considering GLU (a) and

GLU+CPEP (f), compact neurons clusters with low distance values are concentrated in specific SOM regions surrounded by neurons with high distances that act as a frontier. Similar scenery is obtained using GLU+INS (d) and GLU+INS+CPEP (g). However, in this case, the frontier region is characterised by lower distance values. Using INS (b) and INS+CPEP (e), the clear identification of two clusters as in (a) is not possible. For CPEP curves (c), almost all neurons have similar distance values.

The presence of distinct clusters is evident considering GLU and GLU+CPEP curves (Figure A4 a and f) and mild but still present when GLU+INS and GLU+INS+CPEP curves are considered (Figure A4 d and g). The same analysis performed on INS and INS+CPEP curves generates more complex and dispersed U-matrices (Figure A4 b and e). For CPEP curves, instead, almost all the neurons are characterised by very close neighbours distance values, giving rise to a sort of single cluster involving the entire SOM (Figure A4 c). Also in this case, plotting the first two principal components of prototype vectors confirms the visual inspection of the U-matrices. Even if the neighbours distances in the U-matrix are still very low (lower than 0.04), the darkest neurons are divided into two different regions, surrounded by lighter ones (Figure A5), making clear the identification of the two main clusters previously noticed (Figure A4).

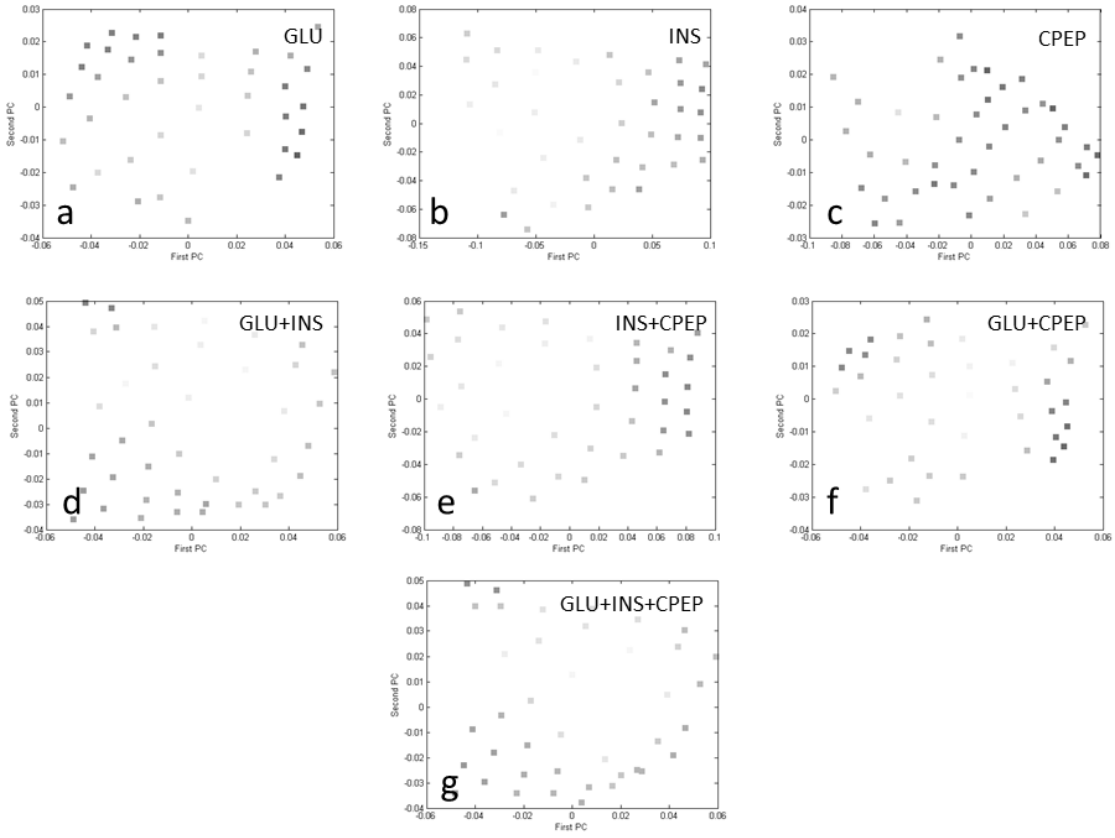

Figure A5. Prototype vectors of SOMs trained with CNT and T2DM groups plotted in their principal components space. The controls and the diabetic groups were considered. After using sets of GLU, INS, CPEP, GLU+INS, INS+CPEP, GLU+CPEP and GLU+INS+CPEP for training the SOMs, the first two principal components of each prototype vector were plotted. The colour of each point is referred to the corresponding distance reported in the U-matrices (Figure A4). Neurons with low neighbours distance values are grouped into two well separated clusters, if GLU (a) and GLU+CPEP (f) curves are considered. Two major clusters of neurons with low distance values could be still identified plotting principal components of prototype vectors of SOMs trained with GLU+INS (d) and GLU+INS+CPEP (g). Any cluster could be detected for INS (b), CPEP (c) and INS+CPEP (e).

Again, this result is particularly clear for GLU and GLU+CPEP curves (Figure A5 a and f). The plots of prototype vectors of GLU+INS and GLU+INS+CPEP curves in the plane of the first two PCs show that two clusters can be barely identified (Figure A5 d and g). In the other cases, the prototype vectors seemed to be not able to

identify different region of the space corresponding to different curve shapes (Figure A5 b, c and e).

The morphological features of OGTT curves identified by SOMs were compared as follows: neurons characterized (1) by a number of curves associated greater than two and (2) by a distance value from neighbours lower than 50% of the U-matrix highest distance (i.e. lower than 0.012 for GLU and GLU+CPEP curves and 0.015 for GLU+INS and GLU+INS+CPEP curves) were selected and grouped together in clusters (Figure A6 a, d and A7 a, d).

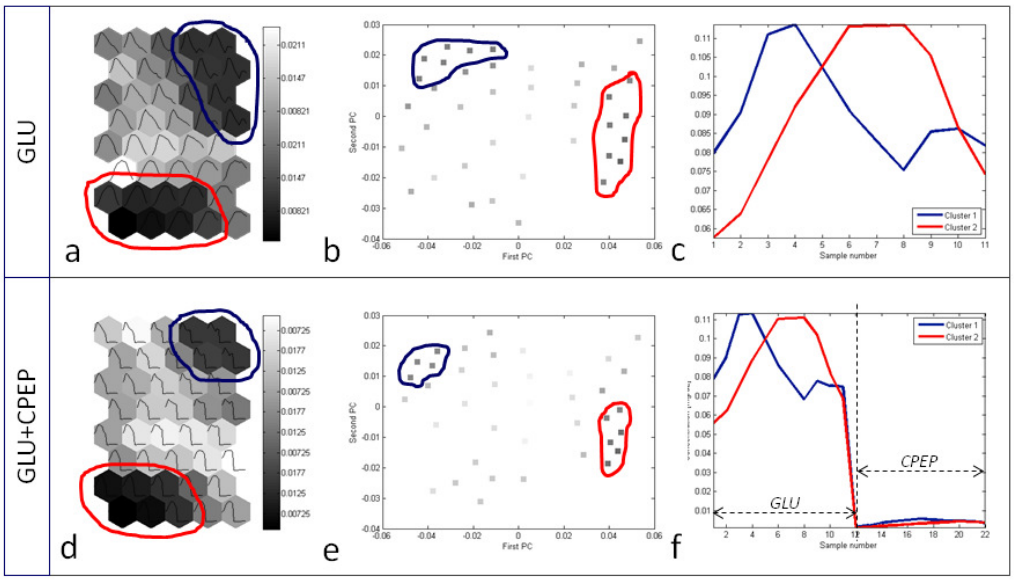

Figure A6. Clusters identified in SOMs trained with GLU and GLU+CPEP curves. Neurons with a distance value less than 50% of the highest distance and with more than 2 curves associated to, were grouped into clusters (a,d). The same neurons were identified in the principal components space (b,e). Then, the prototype vectors of those neurons were averaged obtaining the curves plotted in (c,f). In (c), the average prototype vectors collect all the main features of Glucose curves: for cluster number 1 (blue line), a more complex curve with a higher initial and final value is observed; for cluster 2 (red line), instead, a monophasic shape is noticed. In (f), the average prototype vectors reflect the principal characteristics of Glucose and C-peptide curves that were simply queued for training the

SOM. The Glucose features are the same reported in (c). Also the C-peptide averaged curves show the characteristics noticed for GLU.

The choice of the threshold as 50% is purely qualitatively (as usually done with U-matrix) derived from the fact that we would like to find just two clusters. Then, prototype vectors belonging to single clusters were averaged and the average curves were plotted. The results are displayed in figures A6 and A7. As for the GLU and GLU+CPEP curves, the average prototype vectors belonging to one of the clusters (blue curve) exhibit more complex shapes, with two complete peaks, one occurring in the first part of the test and the other the end. On the contrary, monophasic shapes characterize the average prototype vector of the other cluster (red curve), with the only peak occurring in the middle of the OGTT test (Figure A6 c and f).
Furthermore, the average prototype vectors of the two clusters differ for different glucose concentration at the beginning and at the end of the test. Notably, the contribution given by the C-peptide curves is minimal (Figure A6 f).

Similar features can be noticed in the average curves of prototype vectors belonging to single clusters, obtained from SOMs trained with GLU+INS and GLU+INS+CPEP curves (Figure A7).

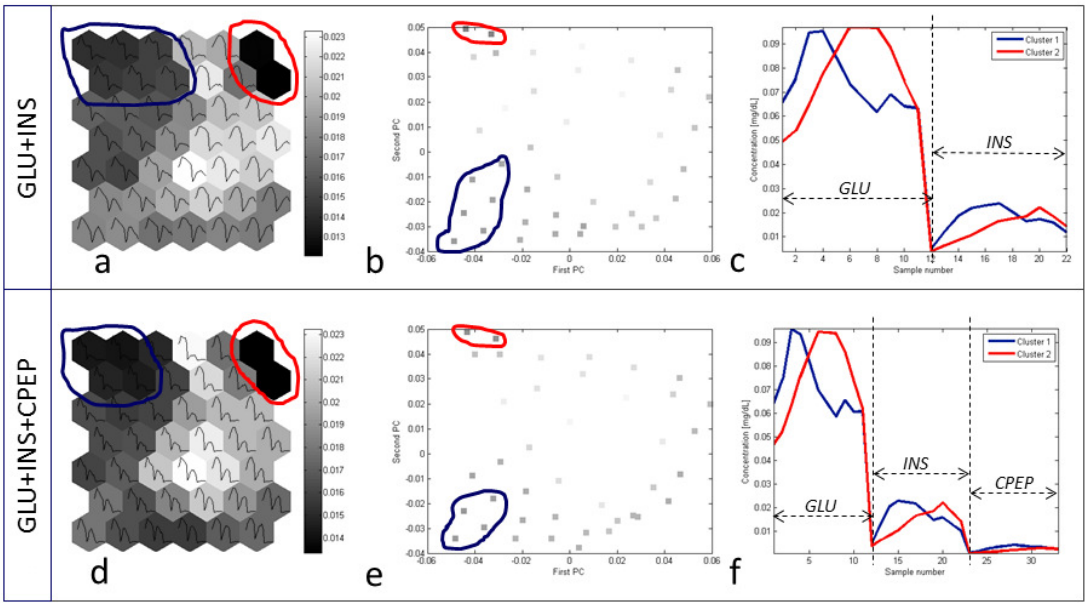

Figure A7. Clusters identified in SOMs trained with GLU+INS and GLU+INS+CPEP curves. Neurons with a distance values less than 50% of the highest distance and with more than 2 curves associated to, were grouped into clusters (a,d). The same neurons were identified in the principal components space (b,e). Then, the prototype vectors of those neurons were averaged obtaining the curves plotted in (c,f). In (c), the average prototype vectors collect all the main features of Glucose and Insulin curves that were simply queued for training the SOM. Cluster number 1 curve (blue line) shows two-peaks shape glucose part with a higher initial and final value, and an almost two-peaks shape insulin part. Cluster 2 curve (red line), instead, has a monophasic shape in both Glucose and Insulin part. In (f), the average prototype vectors reflect the principal characteristics of all kind of curves queued.

Interestingly, the insulin contribution shows the same behaviour as glucose, i.e., a two-peaks shape is present when also the glucose curve shows two complete peaks (blue curve), with the highest peak in the first part of the OGTT test and a monophasic shape when also glucose curve shape is monophasic (red curve), with the peak in the second part of the OGTT test (Figure A7 c and f).

For the next step, we considered the blue curves as representative of a 'normal' condition, while the red curves of a 'diabetic' one based on the morphological features noticed on Figure A6 and A7 and based on observations derived from previous literature[22].

Morphology and Classification

The average prototype vector curves (Figure A6 c, f and A7 c, f) were used as reference curves for the classification based on shape similarity measure. To do it, *KLd* values between normalized NGT curves and reference curves were computed, obtaining the results reported in Table A1.

Table A1. Classification of NGT curves based on Kullback-Liebler distance from the reference curves obtained with SOMs.

Curves	***Normal***	***Diabetic***
GLU	67.44%	32.56%
GLU+CPEP	95.35%	4.65%
GLU+INS	100%	0%
GLU+INS+CPEP	95.35%	4.65%

Considering just GLU reference curves, 67% of NGT curves were correctly classified. Instead, using the other reference curves (GLU+CPEP, GLU+INS and GLU+INS+CPEP), almost 100% of NGT curves were correctly classified.

Morphology and Prediction

Using the average prototype vector curves (Figure A6 c, f and A7 c, f) as reference curves, we used the *KLd* for prediction. Normalized curves at time T_0 were considered and their Kullback-Liebler distances from corresponding referent curves were computed. The validation was possible because the real evolution of those curves at time T_{fu} was known. Table A2 shows the sensitivity, specificity and *p*-value associated to each contingency table computed.

Table A2. Sensitivity, Specificity and p-value of contingency tables built as results of Kullback-Liebler classifier.

Curves	*Sensitivity*	*Specificity*	*p-value*
GLU	0.826	0.633	< 0.001
GLU+CPEP	0.844	0.649	< 0.001
GLU+INS	0.511	0.848	< 0.001
GLU+INS+CPEP	0.556	0.788	< 0.001

Very close results using prototype vectors of SOMs trained with glucose, and glucose and C-peptide curves were obtained. In both cases, in fact, a high sensitivity was reached, meaning that at least the 82% of women that have developed diabetes within two years were correctly identified. The 63-64% of women that remained or became 'normal' was, instead, assigned to the 'normal' evolution. The slight difference obtained using GLU or GLU+CPEP was simply due to the number of not classified subjects: in case of GLU+CPEP, in fact, 3 subjects could not be classified having the same distance from 'normal' and 'diabetic' referent curves.

The opposite behaviour was noticed if GLU+INS or GLU+INS+CPEP were considered. A higher specificity and a lower sensitivity were obtained (Table A2). Also in these cases, 3 subjects were not classified.

The contingency tables built were found statistically significant.

6.A.5. Discussion

In this study we tested the hypothesis that morphological features of glucose, insulin and C-peptide OGTT curves can be predictive of the metabolic condition of women with a history of GDM. To the best of our knowledge, few previous works investigated on the existence of relationships between the shapes of OGTT curves and glucose tolerance [22-24] and only very recently the shape of plasma glucose

concentration curve during OGTT was proposed as predictor of future risk of type 2 diabetes in women with previous GDM [31].

In the analysis presented in this study on frequently sampled 3-h test OGTT curves (1) the entire shape of glucose, insulin and C-peptide OGTT curves was considered, with each single measured sample giving contribution to the prediction and (2) the identification of peculiar morphological features that can discriminate between normal and diabetic subjects was addressed.
It is worth to notice that the method applied here does represent a step forward with respect to the recent cross sectional studies on OGTT curves shape [22]. Our approach, that allowed us (3) to perform an analysis of how the shape of OGTT curves can reflect the history of glucose tolerance state in women with previous GDM and (4) to predict future risks based just on the shape of glucose, insulin and C-peptide OGTT curves, represents a first attempt of longitudinal study applied to GDM.

The rationale behind this study is to reveal if OGTT curve shapes can be the mirror of still not symptomatic mechanisms occurring in glucose metabolism. These mechanisms can be normal (as for healthy subjects) or abnormal (as for T2DM subjects, for example), and influence accordingly the kinetics of both glucose and insulin. For this reason, we hypothesized that the progression from the normal to the diseased (i.e., diabetic) condition can be traceable in features and changes occurring in OGTT curves morphology.
As a first step, we identified those OGTT curves morphological features that are common to a normal condition or to a diabetic one and used them as reference curves to address the driven-by-shape prediction of future risk of type 2 diabetes. Clustering glucose, insulin and C-peptide curves of CNT and T2DM groups allowed us to identify representative-of-the-state curve shapes. Interestingly, our results are in agreement to what is reported in Tura et al. work [22]: the most common curve shapes (not only glucose, but also for insulin and C-peptide kinetics) are monophasic (i.e. with one peak) and triphasic (i.e. with two complete peaks). According to

previous observations [22-24], these curve shapes are highly related to different glucose tolerance condition: the monophasic is the most common among diabetic subjects, while the triphasic represents the normoglycaemic state. The cause of these different shapes was suggested to be in the pulsatile behaviour of insulin secretion (and in plasma insulin concentration, as a consequence) [32]. This pulsatile behaviour involves rapid oscillations (period of 5–15 min), ultradian oscillations with a period of 80–150 min [33], and circadian oscillations [34]. Moreover, it was also observed that insulin oscillations seem to be coupled to glucose oscillations of similar time scale [33, 35]. Since some studies found that these oscillations are depressed in diabetic [36] or elderly subjects [33], it was suggested that the oscillatory behaviour may be an intrinsic characteristic of the insulin-glucose regulation system in healthy individuals, being sign of a specific defect in β-cell function, i.e. a reduced dynamic responsiveness of insulin secretion to glucose changes. For this reason, we associated our monophasic reference curves to a diabetic state and the triphasic curves to a normal state.

The same oscillatory behaviour was found in NGT curves, which we classified as characterized by a triphasic shape more than monophasic. This morphological feature-based classification is markedly improved when a combination of OGTT curves, i.e., GLU+INS, or GLU+CPEP, and GLU+INS+CPEP is considered. Previous observations in which women with former gestational diabetes (but normotolerant after delivery) do not show the majority of indices of insulin sensitivity and beta-cell function significantly different from healthy control women with similar age, BMI, and glucose concentrations [37] agree with our results.

The potency of curves shape for the prediction of the metabolic condition was tested by using a similarity measure between the reference curves, i.e., the monophasic diabetic curve and the triphasic normal curve, and curves from the dataset with a two years follow-up. The hypothesis was that if a subject will evolve to a certain condition, its current OGTT curves should contain morphological features characterizing the final state.

Here, we demonstrated the soundness of our hypothesis. In fact, with the method proposed here, by using only the information on glucose curves we were able to predict that the 82.6% of women belonging to the population under investigation have developed diabetes within two years of follow up. Interestingly, we also noticed that using GLU+CPEP curves do not introduce relevant changes to sensitivity and specificity, indicating that the C-Peptide curve shape could not be meaningful for prediction. We also noticed that adding the shapes of insulin to glucose in both referent curves and dataset curves reversed the situation: a higher ability to recognize normal metabolic condition was reached compared to the ability of predicting diabetic state.

In the clinical practice, the prediction of the metabolic condition of women with a history of GDM is based on several indicators, such as maternal weight, maternal age, fasting plasma glucose concentration, and area under glucose concentration curves [6, 17, 38, 39]. In particular a very recent study [40] proposes pre-pregnancy obesity, weight gain, and fasting glucose level at the OGTT as predictors of T2DM development. However, prediction factors applied in the clinical practice are characterized by sensitivity and specificity values lower than the ones we obtained using just shape as predictor [40].

Our results confirm that the shape of OGTT curves reflect significant change that moves normal metabolic mechanisms into diabetic ones. The onset of T2DM is essentially caused by insulin resistance in muscle and liver, and impairment in β-cell function. Recently, it has become evident that β-cell function plays a more important role than previously expected: it appears that it is the progressive impairment in β-cell function that actually determines the rate of progression toward type 2 diabetes [41]. As there is increasing evidence that the OGTT should be adequate for reliable estimation of β-cell function [42]. The fact that a progressive impairment of β-cell function can be noticed in the progressive changes in the shape of OGTT curves, confirms of the work of Mari and Ferrannini [42].

This study suffers from limitations that are listed in the forthcoming. First of all, the prediction of the metabolic condition is at 2 years after the baseline OGTT.

Unfortunately, the majority of women do not visit the clinic for yearly visits, causing a significant reduction of dataset size as years increase. Another limitation is that the dataset we used for training the SOMs is imbalanced, with the 70% of the OGTT curves being "normal" and only the 30% being "diabetic". Even if SOMs is a tool that is less sensitive to imbalanced data than other tools such as linear regression, a bias derived from the size of the dataset could influence the final results.

In conclusion, we have shown that the shape of glucose OGTT curves can be a reliable indicator to predict the metabolic condition of women with a history of GDM. Our results suggest that the morphology of the OGTT curves reflect those significant changes in the underlying mechanisms that are involved in glucose metabolism. Moreover, our results suggest that it is the shape of the OGTT curves rather than the exact values of each sample that contains information of glucose metabolism evolution. Therefore, a classifier based on morphological features (1) could be helpful in prediction of T2DM development in women with a history of GDM and (2) could be easily translated to the clinical practice.

6.A.6. References

1. American Diabetes Association: **Standards of medical care in diabetes 2008**. *Diabetes Care* 2008, **31**:S12-S54.
2. Kjos SL, Buchanan TA: **Current concepts: Gestational diabetes mellitus**. *New England Journal of Medicine* 1999, **341**(23):1749-1756.
3. Lencioni C, Volpe L, Miccoli R, Cuccuru I, Chatzianagnostou K, Ghio A, Benzi L, Bonadonna RC, Del Prato S, Di Cianni G: **Early impairment of beta-cell function and insulin sensitivity characterizes normotolerant Caucasian women with previous gestational diabetes**. *Nutrition Metabolism and Cardiovascular Diseases* 2006, **16**(7):485-493.
4. American College of Obstetricians and Gynecologists Committee on Practice Bulletins--Obstetrics: **ACOG Practice Bulletin. Clinical management guidelines**

for obstetrician-gynecologists. Number 30, September 2001 (replaces Technical Bulletin Number 200, December 1994). Gestational diabetes. *Obstetrics & Gynecology* 2001, **98**(3):525-538.

5. MeyersSeifer CH, Vohr BR: **Lipid levels in former gestational diabetic mothers**. *Diabetes Care* 1996, **19**(12):1351-1356.
6. Pallardo F, Herranz L, Garcia-Ingelmo T, Grande C, Martin-Vaquero P, Janez M, Gonzalez A: **Early postpartum metabolic assessment in women with prior gestational diabetes**. *Diabetes Care* 1999, **22**(7):1053-1058.
7. Jovanovic L, Pettitt DJ: **Gestational diabetes mellitus**. *Jama-Journal of the American Medical Association* 2001, **286**(20):2516-2518.
8. Kim C, Newton KM, Knopp RH: **Gestational diabetes and the incidence of type 2 diabetes - A systematic review**. *Diabetes Care* 2002, **25**(10):1862-1868.
9. Bellamy L, Casas J-P, Hingorani AD, Williams D: **Type 2 diabetes mellitus after gestational diabetes: a systematic review and meta-analysis**. *Lancet* 2009, **373**(9677):1773-1779.
10. Zinman B, Gerich J, Buse JB, Lewin A, Schwartz S, Raskin P, Hale PM, Zdravkovic M, Blonde L: **American Diabetes Association. Standards of medical care in diabetes-2010 (vol 33, pg S11, 2010)**. *Diabetes Care* 2010, **33**(3):692-692.
11. Metzger BE, Buchanan TA, Coustan DR, De Leiva A, Dunger DB, Hadden DR, Hod M, Kitzmiller JL, Kjos SL, Oats JN *et al*: **Summary and recommendations of the Fifth International Workshop-Conference on Gestational Diabetes Mellitus**. *Diabetes Care* 2007, **30**:S251-S261.
12. Ratner RE, Christophi CA, Metzger BE, Dabelea D, Bennett PH, Pi-Sunyer X, Fowler S, Kahn SE, Diabet Prevention Program Res G: **Prevention of Diabetes in Women with a History of Gestational Diabetes: Effects of Metformin and Lifestyle Interventions**. *Journal of Clinical Endocrinology & Metabolism* 2008, **93**(12):4774-4779.
13. Retnakaran R, Qi Y, Sermer M, Connelly PW, Hanley AJG, Zinman B: **Glucose Intolerance in Pregnancy and Future Risk of Pre-Diabetes or Diabetes**. *Diabetes Care* 2008, **31**(10):2026-2031.
14. Henry OA, Beischer NA: **Long-term implications of gestational diabetes for the mother**. *Baillieres Clinical Obstetrics and Gynaecology* 1991, **5**(2):461-483.
15. Metzger BE, Cho NH, Roston SM, Radvany R: **Prepregnancy weight and antepartum insulin-secretion predict glucose-tolerance 5 years after gestational diabetes-mellitus**. *Diabetes Care* 1993, **16**(12):1598-1605.
16. Damm P, Kuhl C, Bertelsen A, Molstedpedersen L: **Predictive factors for the development of diabetes in women with previous gestational diabetes-mellitus**. *American Journal of Obstetrics and Gynecology* 1992, **167**(3):607-616.
17. Coustan DR, Carpenter MW, Osullivan PS, Carr SR: **Gestational diabetes - predictors of subsequent disordered glucose-metabolism**. *American Journal of Obstetrics and Gynecology* 1993, **168**(4):1139-1145.
18. Bian XM, Gao P, Xiong XY, Xu H, Qian ML, Liu SY: **Risk factors for development of diabetes mellitus in women with a history of gestational diabetes mellitus**. *Chinese Medical Journal* 2000, **113**(8):759-762.

19. Fuchtenbusch M, Ferber K, Standl E, Ziegler AG: **Prediction of type 1 diabetes postpartum in patients with gestational diabetes mellitus by combined islet cell autoantibody screening - A prospective multicenter study**. *Diabetes* 1997, **46**(9):1459-1467.
20. Lee AJ, Hiscock RJ, Wein P, Walker SP, Permezel M: **Gestational diabetes mellitus: Clinical predictors and long-term risk of developing type 2 diabetes - A retrospective cohort study using survival analysis**. *Diabetes Care* 2007, **30**(4):878-883.
21. Jang HC, Yim CH, Han KO, Yoon HK, Han IK, Kim MY, Yang JH, Choi NH: **Gestational diabetes mellitus in Korea: prevalence and prediction of glucose intolerance at early postpartum**. *Diabetes Research and Clinical Practice* 2003, **61**(2):117-124.
22. Tura A, Morbiducci U, Sbrignadello S, Winhofer Y, Pacini G, Kautzky-Willer A: **Shape of glucose, insulin, C-peptide curves during a 3-h oral glucose tolerance test: any relationship with the degree of glucose tolerance?** *American Journal of Physiology-Regulatory Integrative and Comparative Physiology* 2011, **300**(4):R941-R948.
23. Tschritter O, Fritsche A, Shirkavand F, Machicao F, Haring H, Stumvoll M: **Assessing the shape of the glucose curve during an oral glucose tolerance test**. *Diabetes Care* 2003, **26**(4):1026-1033.
24. Kanauchi M, Kimura K, Kanauchi K, Saito Y: **Beta-cell function and insulin sensitivity contribute to the shape of plasma glucose curve during an oral glucose tolerance test in non-diabetic individuals**. *International Journal of Clinical Practice* 2005, **59**(4):427-432.
25. mellitus Ecotdacod: **Report of the expert committee on the diagnosis, and classification of diabetes mellitus**. *Diabetes Care* 2003, **26**:S5-S20.
26. Morbiducci U, Di Benedetto G, Kautzky-Willer A, Deriu MA, Pacini G, Tura A: **Identification of a model of non-esterified fatty acids dynamics through genetic algorithms: The case of women with a history of gestational diabetes**. *Computers in Biology and Medicine* 2011, **41**(3):146-153.
27. Kohonen T: **Self-organizing maps of massive databases**. *Engineering Intelligent Systems for Electrical Engineering and Communications* 2001, **9**(4):179-185.
28. Kullback S, Leibler RA: **On information and sufficiency**. *Annals of Mathematical Statistics* 1951, **22**(1):79-86.
29. Vesanto J, Alhoniemi E: **Clustering of the self-organizing map**. *Ieee Transactions on Neural Networks* 2000, **11**(3):586-600.
30. Ringnér M: **What is principal component analysis?** *Nature Biotechnology* 2008, **26**(3):303-304.
31. Abdul-Ghani MA, Lyssenko V, Tuomi T, DeFronzo RA, Groop L: **The shape of plasma glucose concentration curve during OGTT predicts future risk of type 2 diabetes**. *Diabetes-Metabolism Research and Reviews* 2010, **26**(4):280-286.
32. Porksen N, Hollingdal M, Juhl C, Butler P, Veldhuis JD, Schmitz O: **Pulsatile insulin secretion: Detection, regulation, and role in diabetes**. *Diabetes* 2002, **51**:S245-S254.

33. Scheen AJ, Sturis J, Polonsky KS, VanCauter E: **Alterations in the ultradian oscillations of insulin secretion and plasma glucose in aging**. *Diabetologia* 1996, **39**(5):564-572.
34. Vancauter E, Shapiro ET, Tillil H, Polonsky KS: **Circadian modulation of glucose and insulin responses to meals - Relationship to cortisol rhythm**. *American Journal of Physiology* 1992, **262**(4):E467-E475.
35. Shapiro ET, Tillil H, Polonsky KS, Fang VS, Rubenstein AH, Vancauter E: **Oscillations in insulin-secretion during constant glucose-infusion in normal man - Relationship to changes in plasma-glucose**. *Journal of Clinical Endocrinology & Metabolism* 1988, **67**(2):307-314.
36. Sturis J, Polonsky KS, Shapiro ET, Blackman JD, Omeara NM, Vancauter E: **Abnormalities in the ultradian oscillations of insulin-secretion and glucose-levels in type-2 (non-insulin-dependent) diabetic-patients**. *Diabetologia* 1992, **35**(7):681-689.
37. Tura A, Mari A, Winzer C, Kautzky-Willer A, Pacini G: **Impaired beta-cell function in lean normotolerant former gestational diabetic women**. *European Journal of Clinical Investigation* 2006, **36**(1):22-28.
38. Catalano PM, Vargo KM, Bernstein IM, Amini SB: **Incidence and risk-factors associated with abnormal postpartum glucose-tolerance in women with gestational diabetes**. *American Journal of Obstetrics and Gynecology* 1991, **165**(4):914-919.
39. Schaefer-Graf UM, Buchanan TA, Xiang AH, Peters RK, Kjos SL: **Clinical predictors for a high risk for the development of diabetes mellitus in the early puerperium in women with recent gestational diabetes mellitus**. *American Journal of Obstetrics and Gynecology* 2002, **186**(4):751-756.
40. Akinci B, Celtik A, Yener S, Yesil S: **Prediction of developing metabolic syndrome after gestational diabetes mellitus**. *Fertility and Sterility* 2010, **93**(4):1248-1254.
41. DeFronzo RA: **From the Triumvirate to the Ominous Octet: A New Paradigm for the Treatment of Type 2 Diabetes Mellitus**. *Diabetes* 2009, **58**(4):773-795.
42. Mari A, Ferrannini E: **beta-cell function assessment from modelling of oral tests: an effective approach**. *Diabetes Obesity & Metabolism* 2008, **10**:77-87.

6.B. Modeling Clinical Engineering Activities to Support HealthCare Technology Management

6.B.1. Abstract

Biomedical technology is a valuable asset of healthcare facilities. It is now universally accepted that, to assure patient safety, medical devices must be correctly managed and used, and that the quality of healthcare delivery is related to the suitability of the available technology. The activities that guarantee a proper management are carried out by the people working in a Clinical Engineering (CE) department. In this section, we describe a model to estimate the number of clinical engineers and biomedical equipment technicians (BMET) that will constitute the Clinical Engineering department staff. The model is based on the activities to be simulated, the characteristics of the healthcare facility, and the experience of human resources. Our model is an important tool to be used to start a Clinical Engineering department or to evaluate the performances of an existing one. It was used by managers of Regione Piemonte to start a regional network of Clinical Engineering departments.

6.B.2. Introduction

Biomedical technology is strategically important to effectiveness of healthcare facilities. During the middle of the 60s technology started to spread inside the hospitals. The instruments were definitively simpler than today but their ability to auto-detect failures was small and the problem of their management was mostly concerned with electrical safety or fixing. In the last fifty years the performances and the potentialities of technology increased dramatically and this change significantly affected biomedical instrumentation. Medical devices became more sophisticated and safer, but the number of devices increased significantly. Testing electrical safety turned into one of the activities, and the principal problems became to correctly manage the devices maintenance, to purchase the most suitable instrument, to plan device substitutions, to ensure the correct functioning of the instruments, and to guarantee the availability of critical devices every time they are needed. It is now universally accepted that to assure patient safety, medical devices must be correctly managed and used, and that the quality of healthcare delivery is related to the suitability of the available technology. These activities, related to both technology management and to support physicians and nurses to properly use the devices, are carried on by clinical engineers (CEs) and biomedical equipment technicians (BMETs), usually employed in clinical engineering department (CED).

Following the technology progress, also the clinical engineering changed accordingly. Its role, in fact, moved from dealing with electrical safety and on-site repair of a damaged device to the more complete Healthcare Technology Management (HTM). This term is used for underlining the attention not only on one activity (i.e. electrical safety), but on all processes associated to technology management (i.e. acquisition, maintenance and so on). According to [1], costs, technology improvements, and social expectation led this transition. In this framework, the role of clinical engineering is to support and improve patients care by means of the application of engineering methods to health technology management [2]. The transition also modified the activities carried on by CED. More managerial responsibilities, in fact, have been asked to clinical engineers and also computer

skills have become mandatory, since all CED activities are supported by a computerized system that provides technology inventory management, preventive maintenance scheduling, work orders creations both automatically according to a schedule or manually, maintenance history, downtime of a device, purchase orders, and much more [2].

The organization of a clinical engineering department evolved in the same way as its role. At the beginning, each hospital hired its own clinical engineers. Nowadays, instead, CEs may be employed by a healthcare provider or by an organization that supplies services to multiple healthcare facilities and a more distributed management that takes into account different sizes and acuity levels of health organizations is the most appropriate in the current healthcare business environment [3].

All these aspects impact the CED staff composition and increase the complexity of a clinical engineering department. One way to explore this complexity in a handy way is to create a model that mimics all main features involved in a CED and to simulate that model.

Modeling has been applied in the domain of healthcare both to assist clinical decision making for diagnosis, therapy and monitoring, and to support healthcare managers in facility location and planning, resource allocation, and organizational redesign. Especially the second group of problems benefits also of simulation to understand the consequences of certain solution. There are three main reasons to choose simulation to analyze healthcare problems: healthcare systems are characterized by uncertainty and variability, healthcare organizations can be hugely complex, and the key role is played by human beings [4]. Different methodologies are used according to the model objectives. Among the possible methodologies, most of the models are based either on Discrete Event Simulation (DES) [5] or System dynamics (SD) [6, 7].

DES represents the operations of a system as a sequence of events. Each event occurs at an instant in time and marks a change of state in the system. Usually the time is

simulated by means of probability distributions. DES is widely adopted when the system consists mainly of queues.

SD is a methodology for modeling and simulating complex systems, developed by Forrester [7], based on the idea that the system behavior may be understood by means of the feedback concept, and that it is a function of the activities and interaction of its components. As a consequence, in SD models the system behavior is the result of the interaction of its feedback subsystems that represent its dynamic complexity. A key theme of SD is that policy interventions are diluted, and often fail because decision makers are not fully aware of the feedback structures [8]. SD models are deterministic and can be used at a speculative and strategic level. A few mixed models based on both DES and SD may be found in literature [4].

A new promising tool for modeling the healthcare domain is Multi Agent System (MAS). Agent technology has become a leading area of research in Artificial Intelligence (AI) and computer science [9]. The features of intelligent agents are aimed at distributing the task of solving problems by allowing different software components to cooperate, each one with its own expertise [10]. The multi agent systems paradigm is an emerging and effective approach to tackling distributed problems, especially when data sources and knowledge are geographically located in different places and coordination and collaboration are necessary for decision making [11]. Each agent is a “smart” software program that acts on behalf of human users to find and filter information, negotiate for services, automate complex tasks, and collaborate with other agents to solve complex problems. An important property of intelligent agents is their autonomy. Intelligent agents have a degree of control on their own actions, and under some circumstances, they are also able to make their own decisions, based on their knowledge and the information perceived from the outside environment [12].

When a new clinical engineering department must be established, the healthcare managers must decide the staff composition. In the past, they used to decide the personnel taking into account only the number of beds. With the growing differences among medical devices that are associated to the complexity of the clinical activities

this rule is no longer appropriate. Several more indicators must be taken into account to ensure that the clinical engineering department has the proper staff.

In this work, we describe a model to be used for estimation of the number of clinical engineers and biomedical equipment technicians that constitutes the new CED staff. For this aim, a detailed description of basic activities for a CED was provided. Then, workflow diagrams were built to analyze and describe each activity. Finally, collecting all information previously detailed, a model based on system dynamics was designed, implemented and simulated in order to mimics a CED in all of its features: people involved, activities, time scheduling, and so on. In this way, using inputs that characterized a healthcare facility, it was possible to provide the minimum staff composition for guaranteeing that all activities are completed and the customers' requests (such as maintenance requests) are satisfied. Moreover, this work provides an efficient way to handle and to simulate the complexity occurring in a system with interacting processes, structures and people like a clinical engineering department.

Background

The Italian National Health Service (NHS) follows a model similar to one developed by the British National Health Service since it provides universal health care coverage throughout the Italian State as a single payer. However, the Italian NHS is more decentralized, because it gives political, administrative, and financial responsibility regarding the provision of health care to the twenty regions [13]. Each region must organize its services in order to meet the needs of its population, define ways to allocate financial resources to all the Local Health Agencies (LHAs) within its territory, monitor LHAs' health care services and activities, and assess their performance. In addition, the regions are responsible for selecting and accrediting public and private health services providers and issuing regional guidelines to assure a set of essential healthcare services in accordance with national laws.

The LHAs form the basic elements of the Italian NHS. In addition, in 2000, there were ninety eight public hospitals qualified as "hospital trusts." Hospital trusts work as independent providers of health services and have the same level of administrative

responsibility as LHA. Based on criteria of efficiency and cost–quality, the LHAs might provide care either directly, through their own facilities (directly managed hospitals and territorial services), or by paying for the services delivered by providers accredited by regions, such as independent public structures (hospital agencies and university-managed hospitals) and private structures (hospitals, nursing homes, and laboratories under contract to the NHS).

Each LHA has three main facilities: one department for preventive health care, one or more directly managed hospitals, and one or more districts. Through the districts, the LHAs provide primary care, ambulatory care, home care, occupational health services, health education, disease prevention, pharmacies, family planning, child health and information services.

Both LHA and hospitals build most of their activities on technology, and require a Clinical engineering department to take care of healthcare technology management.

6.B.3. The CED Model

Design

The design step consists in building the conceptual model of a Clinical Engineering Department (CED). The model is essentially based on three main elements: the complexity of the healthcare facility, the activities performed by the CED, and the staff expertise and roles employed in the CED.

The first element (i.e. the complexity of the healthcare facility in which the CED works) is rendered using parameters that describe the territorial and the internal organization of the facility, including also the number and type of devices managed by the facility. In detail, the parameters are the following: (1) number of territorial units (hospitals and districts headed by the facility) (nTU); (1) number of hospitals with Emergency Units (nEU); (2) number of clinical departments (nCD); (3) number

of university departments (nUNIV); (4) number of high-risk devices (such as life supports, critical monitoring, energy emitting and other devices whose failure or misuse is reasonably likely to seriously injure patient or staff) and complex technologies (i.e. devices that require special set-up, like Positron Emission Tomography, or specialized management procedures) (nCOMP); and (6) total number of technologies owned by the facility (nT); (7) number of technologies not covered by a full-risk maintenance contract (nTDM); (8) number of technologies in hospital with emergency unit (nTEU); (9) number of technologies in hospital without emergency unit (nTnoEU); and (10) number of devices used by territorial units (nTTU).

The second element on which the CED model is based regards activities that are considered fundamental for a Clinical Engineering service. The basic or core activities are: department management, acquisition procedures, safety and preventive maintenance testing, critical technologies management, inventory management, investments planning, maintenance procedures and end-users training. A brief description of the activities modelled and who generally performs them is provided in the following paragraphs.

The CE Department management includes all the organization tasks necessary for supervising the clinical engineering department, such as the coordination of the staff, and it is performed essentially by the CE director.

The acquisition process consists of several steps starting from the definition of the specifications and ending when the device is installed in the clinical department. In answer to a public call, different companies send their offer. The offers are then evaluated, and the best one is chosen. After the arrival of the new device, the BMET installs, tests, and inserts the new device into the inventory. If required, the end-users training is also scheduled.

The aim of preventive maintenance is to keep the safety and quality features of technologies during the entire period of their exercise. In so doing, planning safety and functional tests, done periodically according to the laws and technical standards, is mandatory. Also the end-users education is important in this context to avoid the

malfunction of a device due to an incorrect use. The people responsible for this activity are both CE, for planning, and BMET, for the execution of the plan.

The Clinical engineering department must guarantee the continuous availability of devices defined as critical through the predisposition, update and application of a plan for finding a substitute of the device that is out of order as fast as possible and, in any case, to assure both patient safety and the healthcare essential activities. The clinical engineer has the responsibility of performing this activity.

The inventory management allows the staff to record all the data concerning a device from its insertion into the database to the dismissal: in particular, the technical characteristics, its location, and both preventive and corrective maintenance data. The BMET is responsible of these procedures.

The activity of investments planning, done by CE, deals essentially with a triennial, an annual and three-monthly plan to define the needs of the healthcare facility. Moreover, a monthly review is necessary to check the effective execution of plans done so far. The investments could be necessary for substituting a technology, for improving the functionalities of an existing one, buying new components, or for acquiring new devices.

Finally, the corrective maintenance procedures are all the processes that regard the restoration of damaged technologies. This activity is usually performed by BMETs.

The third main element of the CED model is the staff employed in a clinical engineering department. At this stage, we considered clinical engineers (CEs) and biomedical equipment technicians (BMETs) without any particular specialization.

The last step in building a conceptual CED was to define the outputs. The main outputs are essentially the number of people that must be involved in the staff to guarantee a certain level of service effectiveness, the workload of each kind of staff member in terms of hours, the overtime required for completing tasks, and the answering time to a specific request, i.e. the delays between the arrival of maintenance queries and their solution.

Figure B1 shows a schematic representation of the conceptual model.

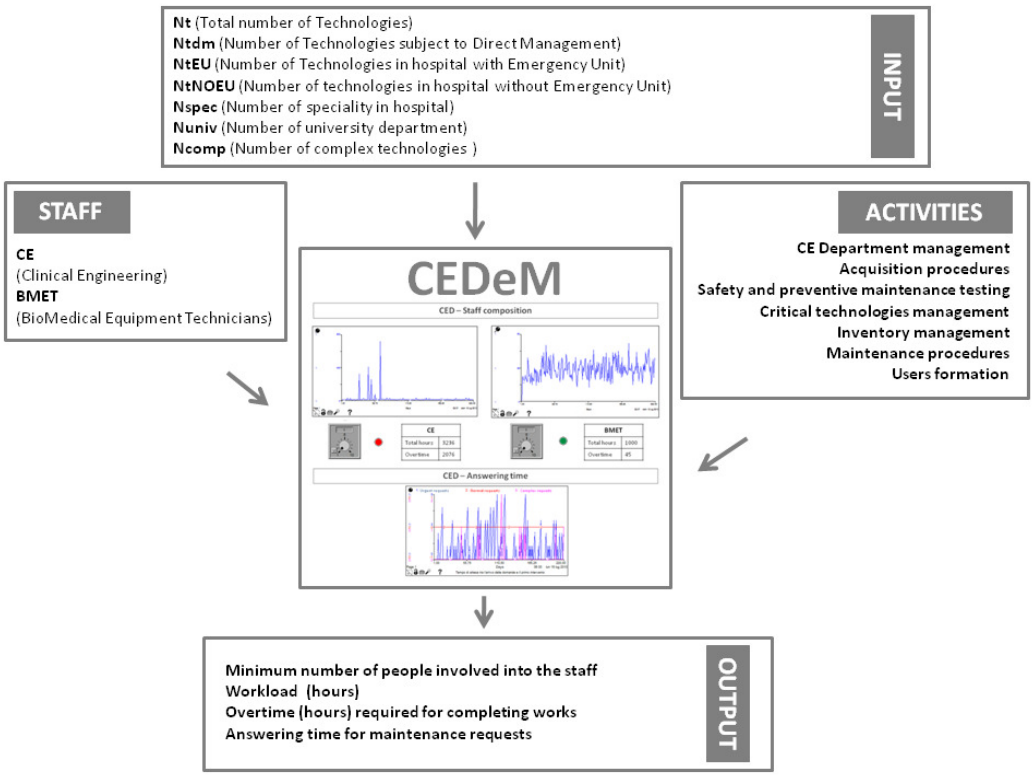

Figure B1. General description of the model.

After identifying in greater detail the features of the CED model, a more in-depth description was necessary, underlining the connection among the three basic elements previously listed (i.e. parameters, activities and people involved). Among the possible methods that can be used, we selected workflow diagrams, and in particular the diagram proposed by [14] and based on Petri nets. It allows the description of different types of jobs or processes, where each process is constituted by a set of tasks that have to be completed following defined rules. One person or a group of people is identified as responsible for each specific task that constitutes the workflow. In our case, each process is one activity that can be completed through a series of sub-activities (tasks) following some procedures (rules). The diagram consists of transitions, shown as rectangles, and places, represented using a circle. Transitions represent the tasks performed during the process, while places represent the input and output of a task. Places and transitions are linked by means of a

directed arc. Arcs from a place to a place or a transition to a transition are not possible, because they do not have any meaning.

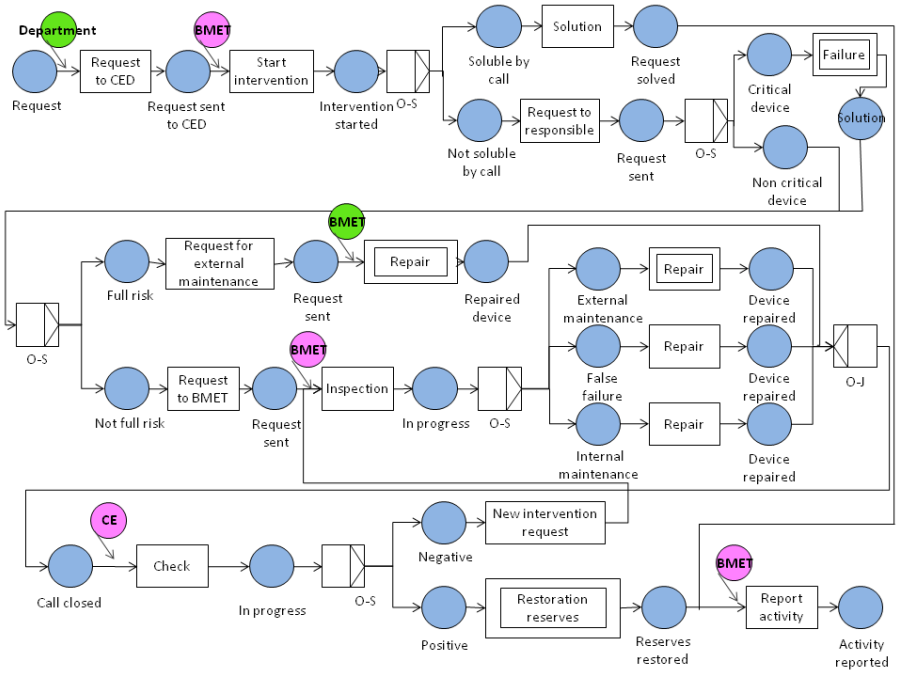

Figure B2. Workflow representing the maintenance process. Rectangles represent the tasks while circles stand for the input conditions and output state. Human resources are associated with the tasks by means of dedicated circles. A detailed description of the tasks is reported in the text.

As an example, Figure B2 shows the workflow of the corrective maintenance activity/process, in which transitions are white rectangles, places are blue circles and people involved are represented by purple circles. The process starts when the call center receives a request of intervention. The BMET that answers the call may be able to solve the problem either because it is only an incorrect use of the device easy to detect or it is a usual problem that may be solved by the user just with a few instructions. If he/she is not able to solve the problem there are two possibilities. If the technology is covered by a particular maintenance contract by the supplier (called full-risk contract) that guarantees assistance in case of malfunctioning, a call for assistance occurs. If the technology does not benefit from a full-risk contract, the

BMET that answered the call asks a BMET assigned to maintenance to go and diagnose the problem. The results of this exploratory assessment may be different. If there is no failure, i.e. the problem is not caused by device, the intervention is closed. If there is a malfunction, then the BMET decides if he/she can fix the problem or if the supplier must be called. In the second case, there are two alternatives: either the technology could be repaired in the healthcare facility (in loco) or it must be sent to the supplier (external intervention). Sometimes, when the external intervention is necessary, the administrative department has to approve that decision and the relative cost. After the repair, BMET verifies the correct functioning of the device: if everything works, the request can be closed, otherwise a new intervention is required. At the end, a report of the intervention with the associated documents is recorded in the inventory database.

Moreover, another important task of corrective maintenance is to guarantee the continuity of functioning of devices defined as critical. In this case, when the failure is diagnoses, the BMET uses the plan for a continuous availability of devices to provide a functioning technology to temporary substitute the damaged one.

Implementation

The processes previously modelled with workflows diagrams were then implemented and simulated using the *iThink* software by ISEE Systems, inc. (http://www.iseesystems.com/), a tool based on system dynamics. iThink employs the System Thinking approach proposed by Checkland [15]. It allows the design and the simulation of models through four levels that are distinct but also strictly connected: the Interface, the Map, the Model and the Equation layer. Starting with the idea of the system that has to be implemented, the first step is to lay out that idea in a map form through the Map layer. This map can be transformed into a model in the Model layer. Five building blocks are provided in these two layers to define the model: stocks, flows, converters, connectors and modules. Briefly, stocks (graphically rendered as rectangles) are measurable accumulations of resources, for example patients, customers and work backlogs. Essentially they are delays which separate and buffer their inputs from their outputs, and are built up and depleted over

time as input and output rates into them change. Flows fill and drain accumulations. The directed pipes represent activities. The results of activities flow into and out of accumulations, changing their magnitudes. Converters (represented as circles) hold value for constants, define external inputs to the model, calculate algebraic relationship, and serve as the repository for graphical functions. Connectors (arrows) connect model elements. Modules are self-contained models that you can connect to other models. Each module within a model is cohesive on its own, so it can be run separately or within the larger model. With these building blocks, a map and a model of the system can be created. During the model building, a list of equations that makes up the model is automatically generated into the Equation layer. Finally, the Interface layer provides the tools for connecting the end-users interface to the model and to make clear the input/output interactions with the model.

In this environment, the workflow of corrective maintenance process previously described was translated (Figure B3).

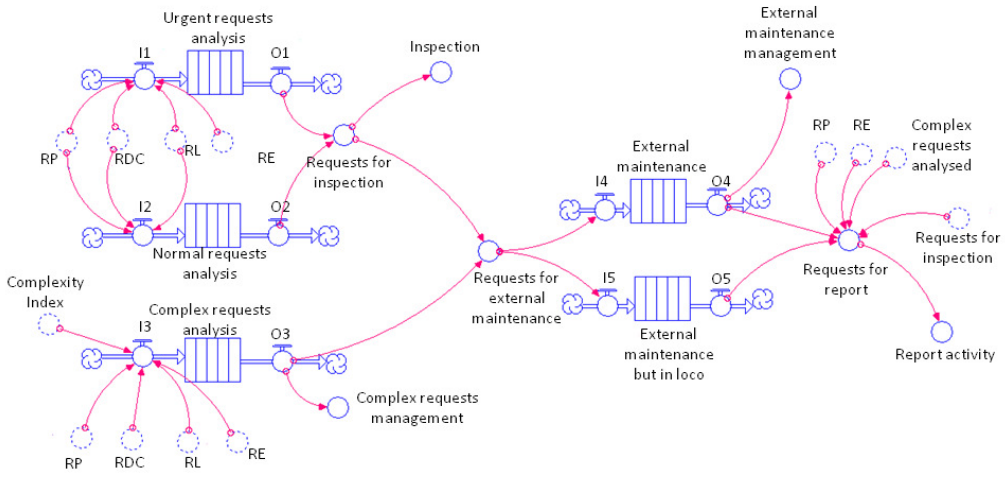

Figure B3. iThink model of the maintenance process as it is defined at the model level. Rectangles represent stocks, red lines are the connectors and the circles the converters. A detailed description of the model is reported in the text.

Depending on the total number of technologies, a stochastic number of requests of maintenance is generated each day. In this way, we simulate the arrival of various

types of demands, concerning essentially failure or malfunctioning of technologies, to the Clinical engineering department call center. Requests are classified according to their urgency, complexity, and the means used (e-mail, phone, letter, or direct call). Demands labelled as urgent must be answered as quickly as possible, while complex demands usually may require an additional time for their solution. For this reason, three accumulations are set with the aim to simulate the waiting time required for the analysis of requests. This time is proportional to the kind of requests. After the analysis, the staff may decide to directly solve some demands or to delegate the corrective intervention to the suppliers. In the former case, the BMET is responsible for the hours necessary to the problem solution. Concerning the intervention of suppliers, a waiting time is considered simulating the time necessary for the sending of the technology, the repair, and the subsequent arrival at facility, or for the 'in loco' intervention, in which a specialised technician is sent to repair the device directly at the facility. In both cases, a certain amount of time has to be referred to BMET for planning activities of these processes. After that, the technology is repaired and the request satisfies.

From this model just described, corresponding equations are derived. They are based on time variables, number of devices, and indicators that take into account the different complexity characterizing each facility. All the times involved in the process were composed by the joining of two parts: a fixed part, which indicated the minimum time required for each task, and a stochastic one for considering the differences among the requests or for any possible inconvenient related to that task that could delay the activity. In this way, the time associated to each task is included between a minimum and a maximum that depends on the activity considered. These minima and maxima derive from the experiences of three different experts that head well-established clinical engineering departments in an Italian region called Regione Piemonte. The times generated for each tasks are then referred to the people of the staff that were responsible of that task.

Simulation

After the user inserts the parameters describing the healthcare facility, the simulation starts, covering a period of one year, leaving out the number of days off provided for contract. So, the total number of days simulated are 220. At the beginning of the process, the number of events associated to each activity is derived from the parameters just inserted. Moreover, in a stochastic way, it is also planned when each event occurs and the amount of hours necessary for completing that activity. For example, the annual investments plan is done once, generally at the beginning of the year. In this case, for this activity, one event is generated and it is scheduled in a stochastic day at the beginning of the year. Suppose, instead, to have 7 acquisition processes: 7 different events are generated and distributed in a stochastic way along the year. So, each day, a certain random number of events related to the different activities occurs. The corresponding amount of hours is referred to people that are responsible for that task. In particular, those hours are assigned to the person that effectively does the work, completing his/her daily working time of 7 hours and 21 minutes (as the employment contract regulates). If at the end of the day the tasks are not finished, the remaining hours are rescheduled the day after and overtime starts to be counted.

The outputs of the simulation are showed through an appropriate interface. For each staff member, there are two numeric displays representing the amount of daily workload and the overtime, both in terms of hours. Moreover, a graph showing the daily distribution of the workload is reported. A status indicator is related to each kind of staff people (CEs, BMETs working inside a single unit, BMETs working across different units) and it is used to point immediately out critical situations. In fact, it acts like a traffic light depending on the amount of working hours: it changes from green to yellow, before, and then to red if the total amount of work, respectively, not exceed, slightly exceed or exceed in a significant way the daily working hours permitted. In detail, we assume that, for each person, a year's workload of [0 - 1584] hours is completely sustainable, [1584 - 1900] is moderately sustainable, and finally a workload that exceed the year's 1900 hours is unsustainable. These numbers are derived from the employment contract. In addition,

the interface shows also the year's distribution of delay in answering customer demands.

Validation

The aims of the validation step were (1) to verify each single assumption made in the model, (2) to demonstrate that the results of the simulation are reliable, and (3) to understand how general is the CED model, in order to apply it to every regional healthcare facility. The validation process required data, both input and output, from well working clinical engineering department. For this reason, we chose three different facilities located in Regione Piemonte, one for each group previously described (ASOu, ASO, ASL), that are characterized by a very settled CED. In order to evaluate the model ability to analyze different situation, the three facilities chosen differed from each other in their sizes (such as the number of total technologies owned, the number of university department, and so on). This can be easily seen in Table B1: the facility A (an university teaching hospital) is the biggest, the facility C (a LHA) is of middle size and the facility B (a hospital trust) is the smallest.

Table B1. Input data corresponding to the facilities used for the validation process.

	A	B	C
Type	ASOu	ASO	ASL
Nt	16995	5619	7642
Ntdm	15495	4103	6979
NtEU	15873	5619	4583
NtNOEU	1122	0	1826
Nspec	49	0	3
Nuniv	17	8	6
Ncomp	14923	4708	6786

For the first part of the validation, the staff was set as it was in the reality: for A, 6 CEs and 16 BMETs; for B, 2 CEs and 7 BMETs; and for C, 3 CEs and 9 BMETs. In

these scenarios, the experts focused on the workload of each kind of staff member, the overtime required for completing tasks, and the answering time to a specific request for evaluating if the model resembles the real situation. Moreover, for each facility, 10 simulations were launched to evaluate the influence of stochastic variables in the model. The outputs derived from those simulations did not differ each other in a significant way (their standard deviation was less than 1%), meaning that the model is robust despite the random feature of some variables. According the experts' experience, for all three facilities results were correct, demonstrating that the simulation provided accurate results and that the model was appropriate to represents different healthcare organizations.

After demonstrating that the model worked correctly, a second validation phase could be performed. The same three different kinds of facility were chosen to investigate the model ability to find the minimum number of staff members. Trying different combination of staff composition, in terms of numerousness of each professional figure, the results obtained were reported in Figure B4.

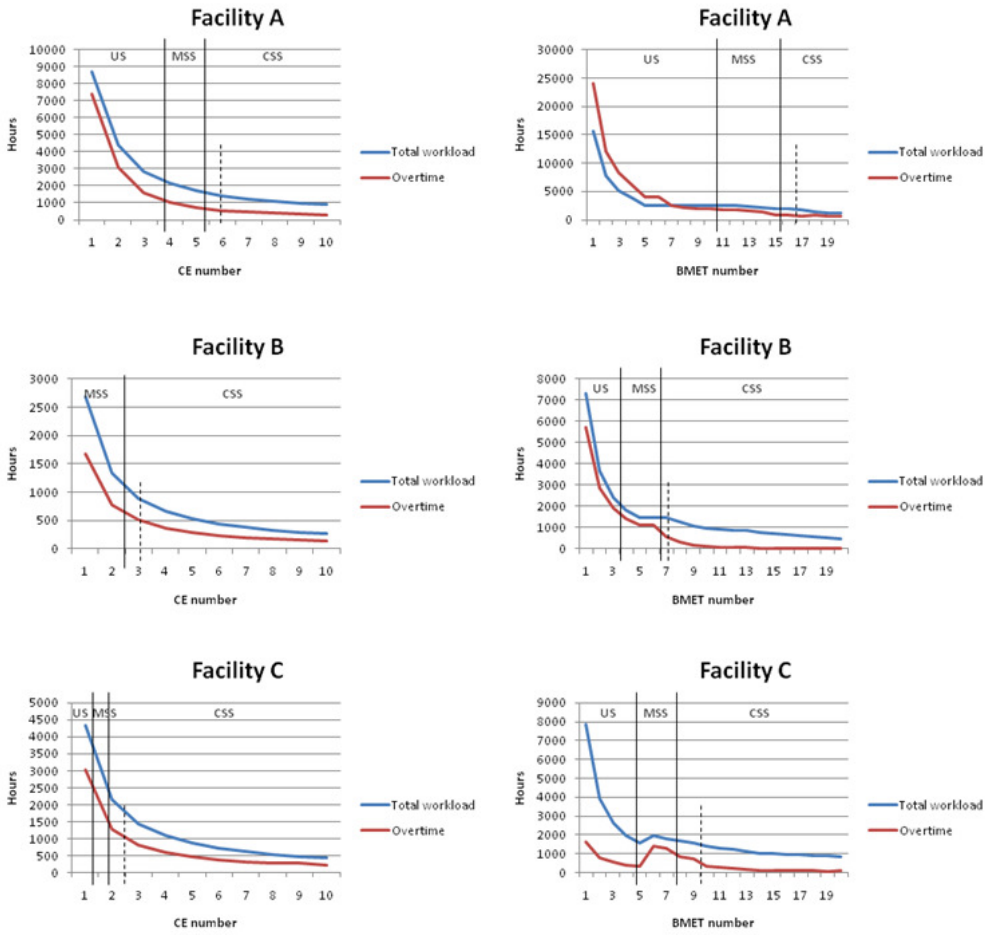

Figure B4. Evolution of total workload and overtime assigned to each person varying the number of CE and BMET of CE Department staff. Depending on the hours amount, it is possible to identify regions of situation that can be unsustainable (US), moderately sustainable (MSS) or completely sustainable (CSS). The definition of sustainability is given evaluating the workload and the answering time to maintenance requests. The dotted line represents the real number of CE and BMET employed in the facilities considered.

As expected, increasing the number of clinical engineers and biomedical equipment technicians led to a decrease of the number of hours associated to each person for completing all occurred events. Both the total number of hours and the overtime obviously followed this trend. Increasing the number of people employed, however, a little bit of overtime generally remained because of the simulation nature: some periods or even only some days, there was a higher concentration of work (such as corrective maintenance, acquisition planning, safety tests to be performed in the

same moment) leading to a higher workload that translated into overtime. Depending on the total number of hours necessary to complete all activities and on the overtime, region of sustainable or not sustainable situation could be depicted. The definition of sustainable or not sustainable situation is not completely fixed, because it depends on the employment contract and on the people's needs. According to our definition of sustainable/moderately sustainable/not sustainable, different scenarios could be analysed. For the facility C, for instance, an unsustainable situation could be reached if the staff was formed by 1 CE and 6 BMETs. Having a quick look of the behaviour of just one activity, the corrective maintenance process generated a very heavy workload, in which each BMET should be able to work for at least 20 hours per day (Figure B5 a).

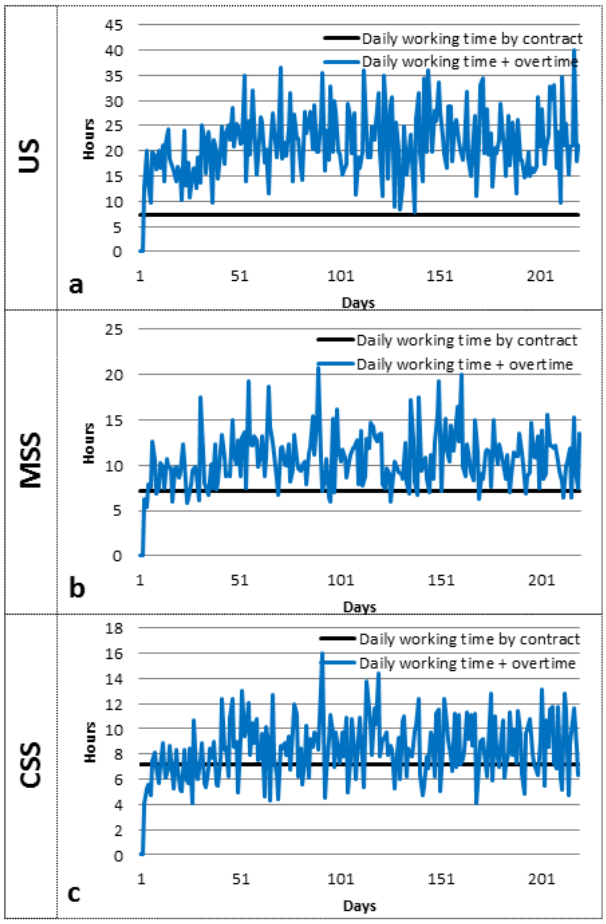

Figure B5. Daily time requested by the corrective maintenance activity in an unsustainable (a), moderately sustainable (b) and completely sustainable (c) situation.

Moreover, in this situation, the answering time for maintenance requests is extremely high (Figure B6 a, c and e), especially for urgent requests that have to wait up to 13 hours before someone could start the maintenance process (Figure B6 a).

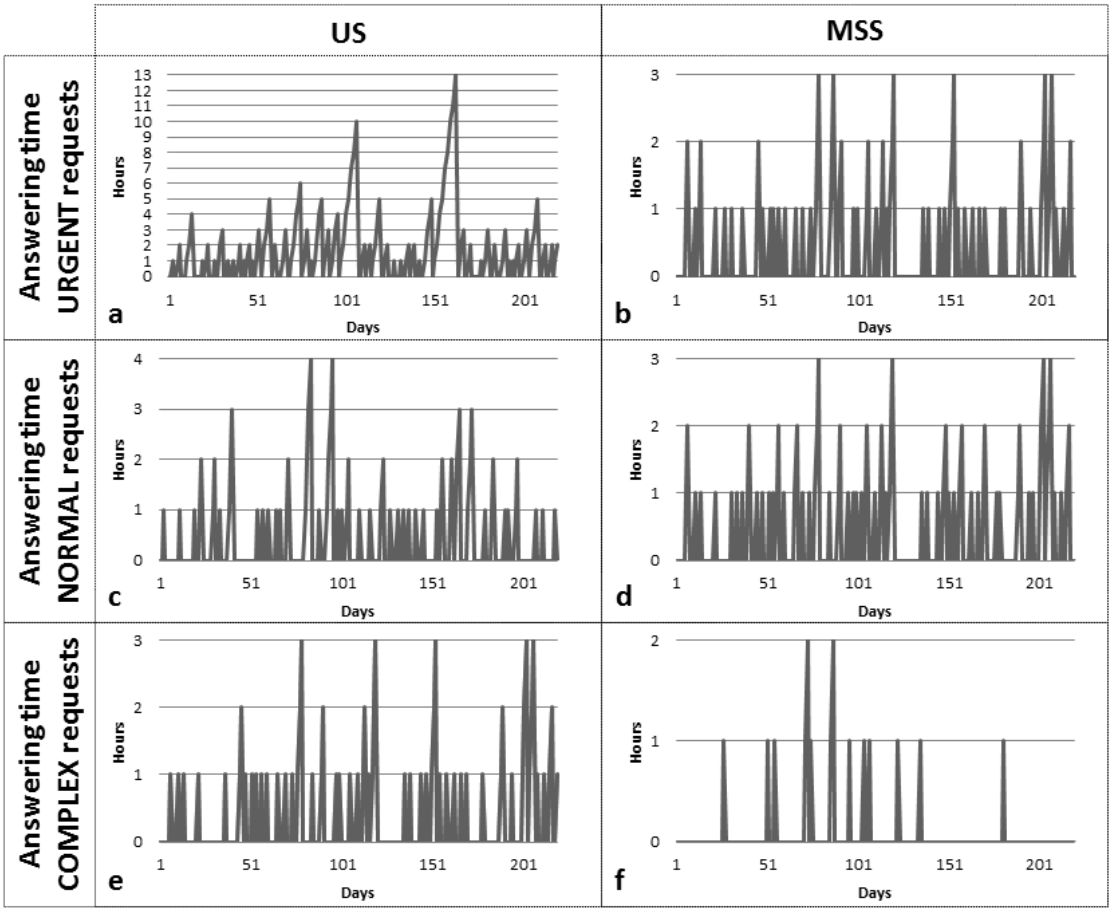

Figure B6. Answering time over the year simulated of urgent, normal and complex requests in unsustainable situations (a, c, e, respectively) and moderately sustainable situations (b, d, f, respectively).

Adding 2 more CEs and 1 more BMET, the situation started to be moderately sustainable. The workload was again high (Figure B5 b), not allowing the staff to

complete every maintenance process, but the answering time began to be reasonable (Figure B6 b, d and f). Finally, a total coverage of works occurred in facility C when the number of CEs is more than 3, and, for BMETs, more than 7. In this case, it was a completely sustainable situation because the hours assigned to each person employed filled the normal working time provided in the contract and the overtime was acceptable (Figure B5 c). Moreover, the answering time for each kind of request was very close to zero (data not shown).

To validate these results with the real situation, the real staff composition was compared with that one come out from CED model. In Figure B4, the dotted lines represented the real number of people employed in clinical engineering department for each facility considered. They were all positioned in the region referred to a sustainable situation. Since the chosen facilities have a well-established clinical engineering department, if the staff composition provided by CED model in sustainable scenario corresponded to the actual staff composition, then the model was able to describe the real situation, even for very different size of facilities. The experts found consistent the CED model results and their real experiences.

Application

Regione Piemonte is an Italian region with a population of 4,4 million people and a healthcare system principally based on public structures. The Region is divided in 21 local healthcare facilities, managing a total of 65 hospitals and more than 13000 beds, with an amount of more than 115000 medical equipment items. Until a few years ago, more than a half of these health facilities had no structured and acknowledged clinical engineering departments. Medical equipment management was usually in charge of technicians belonging to a general maintenance department of the hospital or totally given in outsourcing without any control on quality and costs. Only a few hospitals had specialized BMETs and CEs able to face with the complex processes of managing hospital technologies. Even in this case the staff number was not sufficient to deal with all the requests at a reasonably quality level. In 2005, the growing awareness by regional institutions of the impact of medical technologies in the strategic healthcare choices and high costs led the Regional

Agency for Healthcare Services (AReSS Piemonte - Agenzia Regionale per i Servizi Sanitari) to start a "Health Technology Management" (HTM) working group, in order to support central planning strategies and to coordinate clinical engineering departments activities and procedures. To ensure a good effectiveness of regional coordinating actions, the first goal was to reach an adequate level of healthcare technology management in every local healthcare facility. For this reason in 2006 the AReSS HTM group decided to build a model of a regional network of Clinical engineering departments to be implemented in Regione Piemonte [16].

The CED model previously described was then applied to all 21 healthcare facilities located in Regione Piemonte to suggest the staff composition of the clinical engineering departments that will take part in the network. Moreover, it was possible to simulate different scenarios, characterized by various staff composition, to evaluate drawbacks and benefits of each organizational situation. In so doing, with the model results, every facility could search a good compromise between its CED quality service and the staff composition, in other words between quality service and the costs for setting and maintaining it.

To define the minimum number of staff members necessary for a minimum quality level for each facility, the CED model was simulated several times to understand also the impact on the staff composition on the quality level different combinations of number of CEs and BMET. Some of the results are reported in Figure B7 where, for each facility, the number of CEs and BMETs are plotted against the number of devices to be managed.

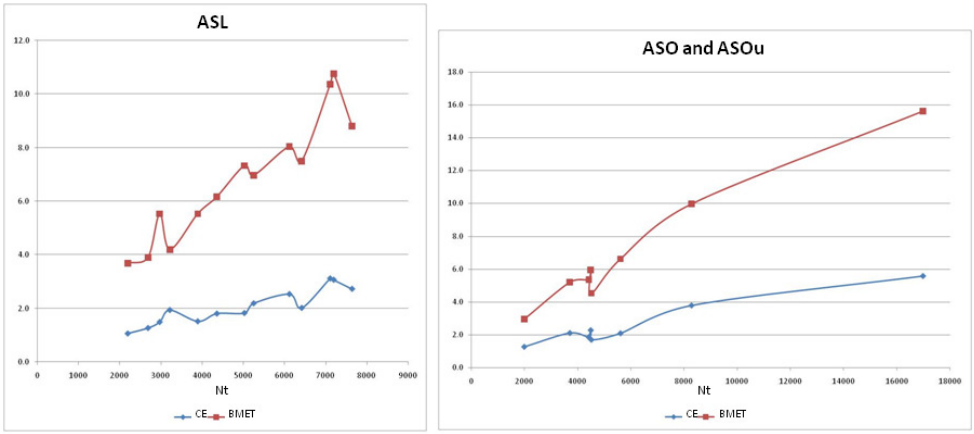

Figure B7. Number of CE and BMET required to perform the basic activities in each Clinical engineering departments of all the healthcare agencies of Piemonte Region.

The figure shows that the linear trend is interrupted in some cases. This is consistent with our design of a CED: in the model, there are some activities that are less dependent on the number of technologies (such as the clinical engineering department management) but that have to be taken into account for the staff workload. With this number of CEs and BMETs, it was possible to guarantee an acceptable workload and overtime for each person and answering time close to zero (data not shown).

In 2008, Regione Piemonte approved an important regional health system reform using these results to start establishing new clinical engineering departments or improving the existing ones. In January 2010, the results were also used by the region managers to promote a regional guideline for developing the CED network. The guideline contains the functions and responsibilities assigned to Clinical engineering departments, classes of equipments to be managed, professionals work profiles in terms of activities and educational background, and the global organization of department.

At this time, about 70% of regional healthcare facilities have a properly structured clinical engineering department.

6.B.4. References

1. David Y, Jahnke EG: **Planning hospital medical technology management**. *Ieee Engineering in Medicine and Biology Magazine* 2004, **23**(3):73-79.
2. Grimes SL: **The future of clinical engineering: The challenge of change**. *Ieee Engineering in Medicine and Biology Magazine* 2003, **22**(2):91-99.
3. Christoffel T: **Thinking outside the box.** *Biomedical Instrumentation & Technology* 2008, **3**(42):1.
4. Brailsford SC: **Tutorial: advances and challenges in healthcare simulation modeling**. *2007 Winter Simulation Conference* 2007.
5. Delaney W, Vaccari E: **Dynamic Models and Discrete Event Simulation**: Dekker INC; 1988.
6. Towill DR: **System dynamics- background, methodology and applications. 1. Background and methodology**. *Computing & Control Engineering Journal* 1993, **4**(5).
7. Forrester J: *Industrial dynamics*. Waltham (MA): Pegasus Communications; 1961.
8. Duggan J: **Using system dynamics and multiple objective optimization to support policy analysis for complex systems**. In *Complex decision making: Theory and practice*. Cambridge (MA): Springer; 2008:59-81.
9. Russel S, Norvig P: **Artificial Intelligence. A modern approach**. New Jersey: Prentice-Hall; 1995.
10. Annichiarico R, Cortés U, Urdiales C: **Agent technology and e-health.** Basel: Birkhuser Verlag; 2008.
11. Yanqing J, Hao Y, Yen J, Shizhuo Z, Barth-Jones DC, Miller RE, Massanari RM: **A distributed adverse drug reaction detection system using intelligent agents with a fuzzy recognition-primed decision model**. *International Journal of Intelligent Systems* 2007, **22**(8).
12. Padgham L, Winikoff M: **Prometheus: A methodology for developing intelligent agents**. In *Agent-Oriented Software Engineering Iii. Volume 2585*. Edited by Giunchiglia FOJWG; 2002:174-185.
13. Maio V, Manzoli L: **The Italian health care system: W.H.O. ranking versus public perception.** *Pharmacy & Therapeutics* 2002, **6**(27):7.
14. van der Aalst W: **Workflow management: Models, methods, and systems**.: MIT Press; 2004.
15. Checkland P: **System thinking, system practice**. Chichester (UK): Wiley; 1981.
16. Balestra G, Gaetano L, Puppato D, Prato G, Freda P, Morena F, Vajo F, Lombardo M: **Modeling a regional network of clinical engineering departments**. *In Proceeding ORAHS 2009* 2009.

Acknowledgments

First of all, I would like to thank my tutor, professor Montevecchi, who let me find my way in the complex world of biomedical research.

Thanks to my other tutor, the non-official one, Lella Balestra, who always finds time for discussing with me and who challenges me with new tasks and new topics. This has really made me grow up during these years.

Thanks to my tutor from UCSF, professor Roland G. Henry, who has trusted in me, even if I did not know anything about images. His behaviour and our discussions always induce me do the best I can and even more, sometimes.

Thanks to Umberto, one of the most capable person I have ever known. His devotion to work, his knowledge and also his criticism have inspired me during my PhD school.

Thanks to Giacomo, his strength, his 'craziness' and his originality have helped me to give the right meaning to things. With the hope of doing something useful at least for him, this thesis is also dedicated to him.

Thanks to all my friends, not colleagues but real friends, at Politecnico di Torino (Piergiorgio, Diana, Chiara T., Elena, Piero, Arianna, Diego, Penny, Irene, Valeria, Chiara F., Alessandro and all the others!). Each of them has taught me something and each of them has been fundamental in my journey. Moreover, with them, I spent the best time at work (and not only at work!) ever!

Thanks to Patricia and the little Pushkin. They received me like a family member and made me feel at home even if I am 10000 km far away from my place.

Thanks to Monica. I will never find the perfect words to thank her! If I am in this 'situation' now, it is just because of her. I hope that all the love that she spreads around goes back to her sooner or later.

Thanks to Maria Luisa and Eduardo. They make San Francisco a cosier place!

Thanks to Mehul and Bago for their help and patience in sharing their knowledge with me.

Thanks to Silvia and Vanessa, my 'sisters'. They are always with me, even if I am at 10000 km far away. And I cannot think my life without them.

Thanks to my mother and my father. If I am exactly like I am and if I am where I am, it is just because of them.

Thanks to my brother. At the end, I always look for his approval.

Thanks to Rossella. I would like that she considers my successes hers. Because I take her with me in what I do.

And last, but not least, thanks to Mark. In these last months, he supported me, helped me in any way he could do, and tolerated my ‘up and down’ moments with a smile. And while I am touching my belly, I can say that I can’t wait to start our new exciting adventure together.